脈衝雷射沉積之硒化鉍與碲化鉍熱電薄膜：
結構，組成和形貌對熱電性質之影響

研究生：黎有福　　　　指導教授 ： 呂志鵬　教授

國立交通大學

材料科學與工程學系

摘要

在熱電冷卻及室溫發電應用方面、硒化鉍（Bi_2Se_3）與碲化鉍（Bi_2Te_3）是廣為人知的熱電材料。熱電材料的性能取決於 $ZT = \alpha^2\sigma T/\kappa$ 值，其中 α、σ、κ 和 T 分別為 Seebeck 係數、電導率、熱導率和絕對溫度。目前，以高沉積溫度，有利於增高 σ 值，但所形成薄膜之組成為非化學計量型。因此如何提昇 Bi_2Se_3 和 Bi_2Te_3 薄膜之熱電功率因子（$PF = \alpha^2\sigma$）仍然有其困難及挑戰性。

本論文研究中，以脈衝雷射 (PLD) 沉積 *n* 型 TE Bi_2Se_3 與 Bi_2Te_3 熱電薄膜在 SiO_2/Si 基板上。進而探討壓力（*P*）與沉積溫度對於 Bi_2Se_3 及 Bi_2Te_3 熱電薄膜的結構、組成、與形貌,及其熱電性質之影響。吾人發現，在較高沉積壓力下（≥ 40 Pa），Bi_2Se_3 沉積基板溫度達 300℃，而 Bi_2Te_3 基板溫度達 340℃時，可製備出具化學計量之熱電薄膜。此不僅降低載流子濃度（*n*），而且依著 $\alpha \sim n^{-2/3}$ 之關係，顯著提高 Seebeck 係數（α）。此外，在較高的基板溫度下沈積，可

得到具高度（00l）晶向的大晶粒，層狀結構，此促使載流子遷移率 (μ) 大幅增加，進而提高電導率 ($\sigma = n\mu e$）。例如，在 300℃及 40 Pa 下沈積製備之 Bi_2Se_3 薄膜，其結構是具有高程度（00l）方向的層狀、六方晶片，此薄膜展現最高的 PF 值，5.54 $\mu Wcm^{-1}K^{-2}$ ，其中 $|\alpha| = 75.8$ μV/ K、$\sigma = 963.8$ S / cm。

同樣地，在 220 – 340°C 基板溫度和 80 Pa 氬氣壓力下，可製備出具化學計量之 Bi_2Te_3 熱電薄膜，其具有高程度之（00l）方向的層狀結構，並展現最佳熱電性能，其中載流子遷移率 $\mu = 83.9 – 122.3$ cm^2/Vs、$|\alpha| =172.8 – 189.7$ μV/K、以及非常高的 PF 值，24.3 $\mu Wcm^{-1}K^{-2}$。反之，在基板溫度(T_s) ≤ 120℃下成長的 Bi_2Te_3 薄膜，含較多的 Te 元素，並具有（015）優選方向之小晶粒、柱狀結構或者在 380℃所沉積製備之薄膜，含有 Te-空缺，另呈現 Bi_4Te_5 多面體結構，導致較差的熱電特性。其 PFs 值， ≤ 0.44 $\mu Wcm^{-1}K^{-2}$，此中 $\mu < 10.0$ cm^2/Vs、$|\alpha| < 54$ μV/ K。

本研究全面性探討 PLD 製程參數、對 Bi_2Se_3 與 Bi_2Te_3 熱電薄膜的微觀結構、組成和形貌對熱電性質之影響， 及其相互關係，進而改善熱電材料的性能和應用。簡而言之，具高度（00l）晶向的大晶粒、層狀結構和化學計量之組成乃為影響 μ 及|α|之主要因素，進而顯著提高 PF 值。

關鍵詞: 熱電材料，Bi_2Se_3，Bi_2Te_3，奈米結構薄膜，脈衝雷射沉積 (PLD) ，沉積溫度，壓力，熱電功率因子（$PF = \alpha^2\sigma$）。

Bi_2Se_3 and Bi_2Te_3 Thermoelectric Thin-Films Grown using Pulsed Laser Deposition: Effects of Structure, Composition, and Morphology on the Thermoelectric Properties

Student: Le Huu Phuoc Advisor: Prof. Jihperng (Jim) Leu

Department of Materials Science and Engineering

National Chiao Tung University

Abstract

Bismuth selenide (Bi_2Se_3) and bismuth telluride (Bi_2Te_3) are well-known compounds for thermoelectric (TE) cooling and generation applications near room-temperature. The performance of TE materials is quantified by a dimensionless figure of merit, ZT = $\alpha^2\sigma T/\kappa$, in which α, σ, κ, and T are the Seebeck coefficient, the electrical conductivity, the thermal conductivity, and absolute temperature, respectively. Currently, enhancing the TE power factor (PF = $\alpha^2\sigma$) of Bi_2Se_3 and Bi_2Te_3 thin-films remains a challenge due to the coupling amongst TE material properties and the difficulty of growing stoichiometric films under elevated substrate temperatures (T_s), at which is beneficial for enhancing the σ.

In this thesis study, n-type TE Bi_2Se_3 and Bi_2Te_3 thin films were grown on SiO_2/Si substrates using pulsed laser deposition (PLD). The effects of the structure, composition, and morphology on the TE properties of Bi_2Se_3 and Bi_2Te_3 thin films were investigated by controlling background ambient pressures (P) and T_s in PLD depositions. We found that the deposition in relatively high P ($\geq$ 40 Pa) could obtain stoichiometric films at extended T_s up to 300 °C for Bi_2Se_3 and 340 °C for Bi_2Te_3, which can reduce the carrier concentration (n) and significantly enhance the Seebeck coefficient (α), following the $\alpha{\sim}n^{-2/3}$ relation approximately. Furthermore, at high T_s-growths, the obtained structures of highly (00l)-oriented – layered of large crystallites led to the substantial increase in the carrier mobility μ and thus improve the σ (= $n\mu e$). For example, the stoichiometric Bi_2Se_3 films grown at grown at 300 °C and 40 Pa with highly (00l) oriented and layered-hexagonal platelets possessed the highest PF of 5.54 µWcm^{-1}K^{-2}, where $|\alpha|$ = 75.8 µV/K and σ = 963.8 S/cm.

Similarly, the stoichiometric Bi_2Te_3 films grown at T_s = 220–340 °C and P_{Ar} = 80 Pa with highly (00l)-oriented and layered structures showed the best properties, with a carrier mobility μ of 83.9 – 122.3 cm^2/Vs, an $|\alpha|$ of 172.8 – 189.7 µV/K, and a remarkably high PF of 18.2 – 24.3 µWcm^{-1}K^{-2}. In contrast, the Te-rich films deposited at $T_s \leq 120$ °C with (015)-preferred orientations and columnar–small grain structures or the Te-deficient film deposited at 380 °C with Bi_4Te_5 polyhedron structure possessed poor properties, with $\mu < 10.0$ cm^2/Vs, $|\alpha| < 54$ µV/K, and PFs ≤ 0.44 µWcm^{-1}K^{-2}.

This study provides a comprehensive understanding the interrelationships between PLD processing conditions, microstructures, and TE properties of Bi_2Te_3-based thin films, promising for further improving the TE performance of materials and applications. In brief, the morphology of highly (00l) oriented–layered large crystallite structures and the stoichiometry predominantly contribute to the substantial enhancement of μ and $|\alpha|$, respectively, resulting in remarkable enhancement in PF.

Key words: Thermoelectric materials, Bi_2Se_3, Bi_2Te_3, nanostructured films, pulsed laser deposition (PLD), substrate temperature, ambient pressure, the thermoelectric power factor ($PF = \alpha^2\sigma$).

Acknowledgements

First and foremost, I gladly acknowledge my debt to Prof. Jihperng (Jim) Leu and Prof. Chih Wei Luo. Without their constant friendship, generous encouragement and concise advice, this thesis would never have been completed. Additionally, I am grateful to Prof. Chien-Neng Liao for his technical comments and suggestions regarding to my researches. I would also especially like to recognize Prof. Ying-Hao Chu, Prof. Jiunn-Yuan Lin and Prof. Kaung Hsiung Wu for the support of using their equipment. Financial support from the National Science Council and the Ministry of Science and Technology of the Republic of China (Taiwan) under Contract No.: NSC101-2221-E-009-126-MY2, NSC101-2112-M-009-016-MY2, 101-2112-M-009-016-MY2, and 103-2923-M-009-001-MY3 is gratefully acknowledged.

I would also like to thank Mr. Hung-En Tu, Mr. Wen-Yen Tzeng, T. T. Yeh, and Mr. Hsueh-Ju Chen for the kindly training of using the equipment/instrument. Especially, I would like to sincerely thank Dr. Nguyen Hong Quan, Dr. Do Thi Hien for the helps of HRTEM measurements and helpful discussions; and Dr. Vu Thanh Tra for his special helps so that I can come and pursue PhD program in National Chiao Tung University, Taiwan.

Finally, special thanks go to my family and my girl friend (Thanh Truc). Your love always made it possible for me to go through tough trails. Thank you for being there, smiling at me with love, good days or bad days.

Le Huu Phuoc

Hsinchu, Taiwan

July 2014

Contents

Table Caption

Figure caption

Chapter 1 Introduction

1.1 Background

Thermoelectric (TE) materials are of interests for applications as heat pumps and power generators [1–4]. The performance of TE materials is evaluated in terms of a dimensionless figure of merit, ZT = $\alpha^2\sigma T/\kappa$, in which α, σ, κ, and T are the Seebeck coefficient, the electrical conductivity, the thermal conductivity, and absolute temperature, respectively. To achieve a high ZT value, a TE material must exhibit a high power factor (PF), $\alpha^2\sigma$, and low thermal conductivity, κ. However, increasing the ZT value is challenging because of the coupling among the TE parameters [4]: the relationship between α and the carrier concentration n (expressed by $|\sim| \sim n^{-2/3}$ [4]) limits the enhancement of the PF (= $\alpha^2\sigma$), whereas the proportional relationship between electrical conductivity and electronic thermal conductivity (the Wiedmann–Franz law) restricts the improvement of the σ/κ ratio.

In order to achieve best results at room temperature, bismuth (Bi)-based chalcogenide narrow-bandgap semiconductors sush as Bi_2Te_3, Bi_2Se_3, Sb_2Te_3, $Bi_2(Te_xSe_{1-x})_3$, and $(Bi_xSb_{1-x})_2Te_3$ are of high interest [2,3,5,6]. They have been widely exploited for Peltier-coolers and thermoelectric generators at low temperature regime (≤150°C) [7–10]. Nanocrystalline and nanostructured Bi-based chalcogenide thin films conduct heat poorly because of extensive phonon scattering at grain boundaries [11–16], but the electrical transport properties of the films are impaired because of lattice imperfections and grain-boundary defects [11], indicating that further investigation is required to determine how to improve PF or the electronic part of ZT.

Currently, enhancing the PF of Bi-based thin films is challenging. Besides the coupling among TE material properties [4], the control of film stoichiometry is a key factor for obtaining better TE properties [2,17–20]. Yet, it is a challenge to grow stoichiometric films because of the tendency for re-evaporation of volatile elements (i.e. Te, Se) at elevated T_s [19,21–23], and the low sticking coefficient Te (< 0.6 for Bi_2Te_3) at T_s beyond 300 °C [24,25] (see Figure 2.12). Numerous charge carriers arising from vacancy defects of volatile elements can constrain the enhancement of $|\alpha|$; however, low carrier concentrations can suppress electrical conductivity if carrier mobility (μ) is poor.

Substantial effort has been devoted to enhancing the PF and ZT values of Bi_2Te_3 and Bi_2Se_3 fabricated using flash evaporation [11,16], co-evaporation [19,26–28], sputtering [12,21,29–31], spark plasma sintering [32–34], metal organic-chemical vapor deposition [35,36], molecular beam epitaxy (MBE) [25,37], pulsed laser deposition (PLD) [13,17,18,38,39], the solvo-thermal method [14], chemical bath deposition [15], and chemical synthesis [40]. Among physical vapor deposition techniques, PLD offers a great versatility in the fabrication of films with multi-element stoichiometry and with a variety of structures, from amorphous or nanostructured to polycrystalline or even epitaxial [13,17,18,38,39]. We postulated that tightly controlling substrate temperatures (T_s) and ambient pressures (P) in PLD growths enables the structures – morphologies and compositions of films to be manipulated extensively, which offers a new method for enhancing the TE properties of films.

In this thesis, the interrelationships between PLD processing conditions, microstructures, and TE properties of Bi-based chalcogenide (Bi_2Se_3 and Bi_2Te_3) have been established. In addition, it has been achieved the remarkable enhancements in PFs up to 5.54 and 24.3 $\mu Wcm^{-1}K^{-2}$ for the optimal Bi_2Se_3 and Bi_2Te_3 films, respectively. The morphology of highly (00l) oriented–layered structures and the stoichiometry predominantly contribute to the substantial enhancement of μ and $|\alpha|$, respectively, resulting in the remarkable enhancement in PF.

1.2 Thesis overview

This study attempts to enhance the TE performance of PLD-grown Bi-based thin films by optimizing deposition conditions. Chapter 1 briefly introduces the background, research gap, motivations, and the general results of this dissertation. Chapter 2 describes the literature review to provide the detailed background of thermoelectric materials (bulks and thin films) and their applications (devices). In addition, the recent development of nanostructured TE materials and the nanostructuring – nanocrystalline strategies for improving the TE properties of Bi_2Te_3-based bulks and thin films are reviewed and discussed in this chapter. Chapter 3 covers the experimental details and instrumentation.

Chapter 4 reports the effects of P and T_s on the structure and morphology of Bi_2Se_3 thin films. The in-plane electrical and TE properties of the films were characterized and an optimized processing window of P and T_s conditions was determined for enhancing the PF of Bi_2Se_3 films. The coupling between α and n was illustrated. The results provide a comprehensive understanding of optimal PLD conditions and morphology of Bi_2Se_3 thin films for TE applications.

Chapter 5 reports the TE properties of Bi_2Te_3 thin films grown at T_s of 30–380 °C, featuring well-defined morphologies and grain sizes ranging from the nanoscale to the microscale. The PFs of the films were substantially enhanced because the resulting improvement in crystal structure enabled attaining high μ values and concurrently achieving stoichiometry, which lowered n and enhanced $|\alpha|$ (following $|\alpha| \sim n^{-2/3}$ approximately). A comprehensive understanding of TE Bi_2Te_3-based thin films grown using PLD is presented. Finally, key findings and contributions of this work are summarized in Chapter 6.

Chapter 2 Literature review

2.1. Introduction to thermoelectrics and applications

Thermoelectric materials are solid-state energy converters whose combination of thermal, electrical, and semiconducting properties allows them to be used to convert waste heat into electricity or electrical power directly into cooling and heating [41].

2.1.1 Thermoelectric effects

Consider a current flowing through a pair of n-type and p-type semiconductors connected in series as shown in Figure 2.1(a). The electrons in the n-type material and the holes in the p-type material all carry heat away from the top metal-semiconductor junctions, which leads to a cooling at the junctions called the Peltier effect. When current flows within the module, one side is cooled and the other heated. If the current is reversed, the hot and cold sides reverse also. For each material, the cooling effect is gauged by the Peltier coefficient Π that relates the heat carried by the charges to the electrical current through [41–43]: $Q = \Pi \times I$.

If a temperature difference is maintained between the two ends of the materials as shown in Figure 2.1(b), higher thermal energy electrons and holes will diffuse to the cold side, creating a potential difference that can be used to power an external load. This Seebeck effect is the principle for thermocouples. The power generation is measured by the Seebeck coefficient α, which relates the voltage generated to the temperature difference through $\Delta V = -\alpha \Delta T$. The Peltier and the Seebeck coefficients are related through the Kelvin relation [41,42]: $\Pi = \alpha T$.

Thermoelectric devices contain many thermoelectric couples (Figure 2.1c, bottom) consisting of n-type (containing free electrons) and p-type (containing free holes) thermoelectric elements wired electrically in series and thermally in parallel (Figure 2.1c, top). A thermoelectric generator uses heat flow across a temperature gradient to power an electric load through the external circuit.

2.1.2 The thermoelectric figure of merit (ZT)

The performance of the thermoelectric materials is often denoted as figure of merit Z whose unit is K^{-1}, or ZT the dimensionless unit [2][3].

$$ZT = \frac{\alpha^2\sigma}{\kappa}T = \frac{\alpha^2\sigma}{\kappa_E + \kappa_L}T \qquad (2.1)$$

where *σ*, *α*, *κ*, and *T* are the electrical conductivity, Seebeck coefficient, thermal conductivity, and absolute temperature, respectively. The total thermal conductivity can be split into lattice contribution (κ_L) and electronic contribution (κ_E). The quantity $\alpha^2\sigma$ is commonly used to represent the thermoelectric power factor (PF).

The efficiency of a thermoelectric device is directly related to ZT. For power generation, the maximum efficiency (η) is expressed by [4,44]:

$$\eta = \frac{T_h - T_c}{T_h} \cdot \frac{\sqrt{1+Z\overline{T}} - 1}{\sqrt{1+Z\overline{T}} + \frac{T_c}{T_h}} \qquad (2.2)$$

and for air-conditioning and refrigeration, the coefficient of performance is [44]:

$$COP = \frac{T_c}{T_h - T_c} \cdot \frac{\sqrt{1+Z\overline{T}} - \frac{T_h}{T_c}}{\sqrt{1+Z\overline{T}} + 1} \qquad (2.3)$$

where T_h and T_c are the hot-end and cold-end temperature of the thermoelectric materials, respectively, and $\overline{T}$ is the average temperature of T_h and T_c. Thus, it is important to use materials with a high ZT value for practical applications.

The best materials so far are alloys of Bi_2Te_3 with Sb_2Te_3 and Bi_2Te_3 with Bi_2Se_3. ZT is of the order of 1 at room temperature. This value gives a COP of about 1 (see Figure 2.2a), which compared to household refrigerators and air conditioners (COP from 2 to 4), makes thermoelectric cooling generally still not competitive. The same holds for power generation (see Figure 2.2b) [42,45].

2.1.3. State-of-the-art high-ZT materials

Figures 2.3(a) and (b) show the ZT values and corresponding working temperatures of state-of-the-art commercial TE n-type and p-type semiconductor bulks [4]. For mid-temperature power generation (500–900 K), materials based on group-IV tellurides are typically used, such as PbTe, GeTe or SnTe alloys [46–49]. Peak ZT values for these materials are typically in the range of 0.8 to 1.1 with p-type materials achieving the highest values (Figures 2.3a,b) [4]. The p-type alloy $(GeTe)_{0.85}(AgSbTe_2)_{0.15}$, commonly referred to as TAGS, with a maximum ZT greater than 1.2 [2]. Successful, high-temperature (> 900 K) thermoelectric generators have typically used silicon–germanium alloys for both n- and p-type legs. The ZT of these materials is fairly low, particularly for the p-type material (Figure 2.3b) because of the relatively high lattice thermal conductivity of the diamond structure [4]. For cooling below room temperature, alloys of BiSb have been used in the n-type legs, coupled with p-type legs of $(Bi,Sb)_2(Te,Se)_3$ [4,50].

2.1.4 Overview of thermoelectric applications

The solid-state devices based on TE effect have no moving fluids or moving parts and have the inherent advantages of reliability, silent and vibration-free operation, a very high power density, and the ability to maintain their efficiency in small scale applications where only a moderate amount of power is needed [51].

Commercial use has been made mostly from Peltier’s thermoelectric cooling (TEC) effect in applications, as demonstrated in Figure 2.4a [52]:

- Small refrigerator devices are used for camping and outdoor activities. For example, the cooler/warmer TE device (Engel Thermo 8) has volume 8 L and weighing just over 3 kg. Its features include cooling performance up to 22°C below ambient temperature and warming up to +65 °C.

- Automotive Climate Control Seat by Gentherm [53]. The system has TE heat pumps in the back and bottom cushions. Conditioned air passes from the TE system through channels to the occupant, providing on-demand cooling or heating. The inset in Figure 2.4a shows the heat pump consisting of a TE module (green box) and a fan (orange).

- Thermal management of tiny laser diodes is used in fiber optic telecom, datacom backhaul networks. TEC can also be used for contact cooling of semiconductor lasers, infrared detectors, CCD- matrix, and miniconditioners for photomultipliers.

- Localized cooling at hot spots of chips. For example, the Intel group is the first to demonstrate both concepts of applying the TE material only to a chip's hottest spots (Figure 2.4a) [54,55]. On the substrate, the researchers grew a 100-µm-thick layered structure, called a superlattice, containing bismuth, tellurium, antimony, and selenium. The structure can pump 1300 W/cm^2 heat from the back side of the chip to the heat spreader. The superlattice caused a roughly 6 °C temperature drop at the hot spot even before the device was powered up, because it conducts heat better than the grease that bonds the rest of the heat spreader to the chip. But once 3 amperes of current were sent through the thermoelectric cooler, the total temperature change was just shy of 15 °C. Managing heat in electronics is a common issue, and TE coolers can improve electronic systems in thermal performance, cost, noise, weight, size or efficiency.

Figure 2.4b shows an overview of the present and potential applications of thermoelectric generators (TEGs) [56]:

- Miniaturized autarkic sensor systems powered by an integrated TEG with a wireless data transmitter.
- Waste heat recovery in automobiles and other combustion-engine-powered vehicles for enhanced efficiency and electric current supply of the electronic system.
- Ventilated wood stove powered by a thermoelectric generator. Enhanced oxygen supply, improves burning process.

- Heating systems and water boilers with TEG units which generate the electricity for the control units and pumping systems.
- On the long term perspective: waste heat recovery for medium-scale industrial facilities.

Solar thermoelectric generators (STEGs)

The crisis at the crippled Fukushima Daiichi nuclear plant due to an earthquake evoked calls for safe, clean, and sustainable energy sources [57]. Solar energy will be the most possible alternative to fill the gap left by the nuclear energy. Recently, Kraemer et al. reported that the developed solar thermoelectric generators (STEGs) achieved a peak efficiency of 4.6 % under AM 1.5G (1 kWm^{-2}) conditions [58].

Wireless sensors and wireless sensor networks

Wireless sensors powered by TEGs in environments where temperature differentials exist would lead to avoiding issues with battery lifetime and reliability and lead to an increase in wireless sensor network implementations [59].

Waste heat recovery systems in vehicles

A large number of car companies, including Volkswagen, VOLVO, FORD and BMW in collaboration with NASA have been developing TE waste heat recovery systems in-house, each achieving different types of performance but all of them expecting to lead to improvements of 3-5% in fuel economy while the power generated out of these devices could potentially reach up to 1200W [59].

Consumer applications

In these applications, the type of solution that TEGs provide varies: it could be related to saving energy when cooking by utilizing thermo-powered cooking sensors, powering mobile phones, watches or other consumer electronics, even body sensing could become more widespread with sensory wristbands, clothing or athletic apparel that monitor vitals such as heart rate, body temperature, etc. [59].

Military and Aerospace

Military and aerospace applications have already become a market such as radioisotope TEGs in space probes, satellites, etc. These applications in a segment where cost considerations are not as important as the ability to efficiently and reliably provide power when needed most, in hostile, remote environments and applications. Even some terrestrial applications have seen adoption of TEG technologies. For example, TEGs worldwide in remote locations such as oil or natural gas pipelines, wells, offshore platforms, etc. have been installed in remote locations by Global Thermoelectric Company [59].

Figure 2.5 outlines the way the market for TEGs is expected to grow in the next few years. Consumer applications will also increase remarkably but the dominant market will remain that for bespoke military and aerospace applications. According to IDTechEx [59], an overall market for thermoelectric energy harvesters will reach $750 million by 2022.

Important factors for industrialization

For industrialization, low cost of TE devices is desired, which involves in some important factors:

(1) TE materials costs → choose TE material systems carefully.

(2) Performance → get the material form and scale right.

(3) Architecture, manufacturing cost → general design approach when considering end user metrics.

Further information of TE devices and applications can be found from websites of the famous TE companies such as Laird/ Nextreme, Marlow, Tellurex, Global Thermoelectric, etc.

2.2. Challenges in enhancing ZT and approaches

2.2.1 Conflicting thermoelectric material properties

The best thermoelectric materials were succinctly defined as ‘‘phonon-glass electron-crystal’’ (or PGEC in short), which means that the materials should have a low lattice thermal conductivity as in a glass, and a high electrical conductivity as in a crystal [60]. The interdependency of the TE parameters makes the enhancement efforts of ZT very challenging. The normal ways of optimizing TE materials are to increase the power factor $\alpha^2\sigma$ by optimizing the carrier concentration n, and/or to reduce the lattice thermal conductivity κ_L by introducing the scattering centers. These parameters are the function of scattering factor r, carrier effective mass m^* and carrier mobility μ and their interconnectivity limit ZT to about 1 in large bulk materials [61].

According to the kinetic definition α is the energy difference between the average energy of mobile carrier and the Fermi energy [62]. If the carrier concentration n is increased, the Fermi energy as well as the average energy increases. However, the Fermi energy increases more rapidly than the average energy when n is increased. As a result α decreases, dragging the factor of $\alpha^2 n$ down rapidly. Thus in attempting to increase ZT for most of the homogeneous materials, the carrier concentration (n) increases electrical conductivity (σ) but reduces the Seebeck coefficient (α). For this reason, in metals and degenerate semiconductors (energy-independent scattering approximation), the Seebeck coefficient can be expressed as [4,63]:

$$\sim = \frac{8\text{®}^{2} k_B^2}{3eh^2} m^* T \left(\frac{\text{®}}{3n}\right)^{2/3} \qquad (2.4)$$

The parameter m^* is density of states effective mass in the Eq. (2.4). The high m^* influence the Seebeck coefficient to raise according to the Eq. (2.4). Most materials having high m^* have generally low μ which limits the Seebeck coefficient by a weighted mobility with the relationship of power factor proportional to $(m^*)^{3/2}\mu$. Also, there is no such thing as an optimal effective mass. There are low mobility high effective mass polaron conductors (oxides, chalcogenides) as well as high mobility low effective mass semiconductors (SiGe, GaAs) [4].

It should also be noted that the defects scatter not only the phonons but also the electrons. Hence, there are some trade-offs carried out in carrier mobility when designing for reducing lattice thermal conductivity. The ratio of μ/κ_L determines the improvement of ZT [2,61]. Although the increase in the ratio is usually experimentally achieved through a more reduction in κ_L rather than that in μ, some fundamental issues in this mechanism are not understood well [61].

The electrical conductivity (σ) and electrical resistivity (ρ) are related to n through the carrier mobility μ:

$$1/\rho = \sigma = ne\mu \qquad (2.5)$$

Wiedemann–Franz Law states that [4] the electronic contribution to the thermal conductivity is proportional to the electrical conductivity (σ) of the materials and the relationship is

$$\kappa_e = L\sigma T = ne\mu LT \qquad (2.6)$$

where ‘e’ is electron charge, and L is Lorenz factor 2.48 × 10^{-8} J^2/K^2C^2 for free electrons and this can vary particularly with carrier concentration [4,64].

Figure 2.6 shows the compromise between large α and high σ in thermoelectric materials that must be struck to maximize the figure of merit ZT. Meanwhile, the low carrier concentration will result into the lower electrical conductivity decreasing ZT. The ZT and PF peaks typically occur at carrier concentrations between 10^{19} and 10^{21} carriers per cm^3 (depending on the material system), which falls in between common metals and semiconductors – that is, concentrations found in heavily doped semiconductors [4].

High mobility carriers are most important for high value of electrical conductivity. Again from the Eq. (2.4), it is shown that increasing the effective mass of the carrier increases α but reduces the carrier mobility μ and hence the electric conductivity σ according to the Eq. (2.5). The thermal excitation of carrier from valence band to conduction band creates holes and electrons in case of the narrow semiconductor. However, the concentration of the major carrier does not vary much. Bipolar effects takes place when two types of carriers are present [3] and this is notorious to achieve effective thermoelectrics. For example, the Seebeck coefficient for different carrier types is given by a weighted average of their electrical conductivity values (σ_e and σ_p) [64].

$$\sim \approx \frac{\sim_e \pm_e + \sim_p \pm_p}{(\pm_e + \pm_p)} \qquad (2.7)$$

In short, any attempt to increase σ, will increase κ_e which contributes to thermal conductivity (κ). In order to counter the increment of κ_e, κ_L can be decreased by various approaches. However, decreasing κ_L with phonon scattering by adding defects results in decrease in carrier mobility and electrical conductivity. These are the major conflicts in the bulk materials properties which were addressed in the researches for more than a half century [61].

2.2.2 Nanostructuring thermoelectric materials

The coefficients α, κ_e and σ in classical physics are interrelated, in such a way that it is not possible to increase one without affecting the others. Therefore, a compromise has to be reached to find the maximum ZT value. In this sense three different strategies have appeared in order to improve the ZT [65]:

(a) Looking for new materials with complex band structures, like heavy fermion compounds (this approach increases (↑)α while keeping the values of σ and κ_e)

(b) Controlling the disorder in materials that can be considered electron crystals and phonon glasses, like Skutterudites or Clathrates. These materials present a rattling effect which causes, (↑)σ and decreases (↓)κ_L see for instance ref. [66]

(c) Nanostructuring, that could lead to (↑)α due to quantum confinement effects, while ↓κ_L due to the scattering of phonons at the interfaces. This is the main reason for the latest improvements in the ZT of different materials.

In 1993, Hicks and Dresselhaus pioneered the concept of nanostructuring in design of thermoelectric materials (i.e. Bi_2Te_3). The addition of the dimensionality and size of the system is added as a new parameter that affects the coupling of the electrical conductivity, Seebeck coefficient, and thermal conductivity, leading to substantially enhanced ZT [67–69]. Regarding the low-dimensional materials approach for improving ZT, two ideas are dominant. Firstly, the introduction of nanoscale constituents would introduce quantum confinement effects to enhance Seebeck coefficient and the power factor $\alpha^2\sigma$. Secondly, the numerous internal interfaces (and nanoinclusions) found in nanostructures would be designed so that the thermal conductivity would be reduced more than the electrical conductivity, based on differences in their respective scattering lengths [67].

As the dimensionality is decreased from 3D crystalline solids to 2D (quantum wells) to 1D (quantum wires) and finally to 0D (quantum dots), the spatial confinement are introduced that create the possibilities to tune the TE properties α, σ, and κ independently. When the system size decreases and approaches the scale comparable to the feature length of electron behavior (e.q. mean free path and wavelength) in any direction, the electronic density of states (D.O.S.) can split and become narrow as well as increase substantially (Figure 2.7a), resulting in the enhancement of α. Meanwhile, the thermal conductivity is also reduced because of the extensive phonon scattering at the surface, interfaces, and grain boundaries, as any dimension is less than the mean free path of phonons. Figure 2.7(b) illustrates examples of different nanostructuring with different dimensionalities [65]. A schematic diagram is shown in Figure 2.7(e) capturing these various phonon scattering mechanisms, along with the electrical transport within a thermoelectric material. For example, in material embedded nano-inclusions (nanoparticles), atomic defects are effective at scattering short wavelength phonons, but larger embedded nanoparticles are required to scatter mid- and long-wavelength phonons effectively. Grain boundaries can also play an effective role in scattering these longer-wavelength phonons [70].

Figure 2.8 plots major milestones achieved for ZT over the past several decades as a function of both year and temperature [58,70]. In the 1950s, Bi_2Te_3 was first investigated as a material of great thermoelectric with ZT~0.6 near room temperature. In recent year, great enhancements in ZT owning to low dimension and nanostructure materials have been reported [1,51,70–81] and achieved the highest ZT value of approximately 2.4.

2.2.3 Formulation and analysis of transport coefficients

Carrier mobility (μ)

The carrier mobility, *μ*, in nanostructured materials differs from bulk material. It can be expressed as [62]:

$$\mu = \left(\frac{e}{m_\sigma}\right)\frac{\int_{E_0}^{+\infty} g(E)\tau(E)v^2(E)(df_0/dE)dE}{\int_{E_0}^{+\infty} g(E)v^2(E)(df_0/dE)dE} = \frac{e\langle\langle\tau\rangle\rangle}{m_\sigma} \qquad (2.8)$$

where <<τ>> denotes an average of the relaxation time involving the non-equilibrium terms of the distribution (df_0/dE). Since carrier velocity $v^2(E) = 2(E-E_0)/Dm_\sigma \sim E$, we can use integration-by- parts to simplify <<τ>> to

$$\langle\tau\rangle = \frac{\int_{E_0}^{+\infty} g(E)\tau(E)f_0(E)dE}{\int_{E_0}^{+\infty} g(E)f_0(E)dE} = \frac{\langle\langle\tau\rangle\rangle}{((2r/D+1)} = \tau_0(k_BT)^r\frac{F_{r+D/2-1}(\eta)}{F_{D/2-1}(\eta)} \qquad (2.9)$$

Where $\langle\tau\rangle$ is now the average over the equilibrium carrier distribution. τ_0 is product of many parameters [62]. Figure 2.9(a) shows the normalized mobility,

$\tilde{\mu}(\eta)=\mu(\eta)/\mu(\eta=-5)$ as a function of the reduced Fermi level, *η*. It shows that *μ* increases with *η* if scattering constant *r* > 0, and vice versa. If *r* = 0, then $\langle\langle\tau\rangle\rangle=\langle\tau\rangle=\tau_0$ and $\mu = e\tau_0/m_\sigma$ are constants. Since *μ* may change either way with increases in *η*, *σ* may also be variable. For example, *σ* in metal tends to decrease with increasing *η* because the reduction in *μ* due to acoustic phonon scattering (*r* = - 1/2) dominates the smaller increase in *n* (when *η* is large). On the contrary, *σ* in non-degenerate semiconductors tends to increase with increasing *η* due to a large increase in *n* (when *η* is small) [62].

Seebeck coefficient (α)

The Seebeck coefficient is described incompletely, and non-quantitatively as being dependent on the symmetry/asymmetry of the electronic band [82] or the energy dependence of the density of states (D.O.S.) in the range of the Fermi level [51], or that ‘‘high and steep’’ D.O.S is required for large Seebeck [83]. Assuming that *g(E)* and *τ(E)* are power law functions, the expression for *α* of a single band is simplified to

$$\alpha = \mp\frac{1}{eT}\left(\frac{\int_{E_0}^{+\infty} g(E)\tau(E)Ev^2(E)(df_0/dE)dE}{\int_{E_0}^{+\infty} g(E)\tau(E)v^2(E)(df_0/dE)dE}-E_F\right)=\mp\frac{1}{eT}\left(\frac{\langle\tau E\rangle}{\langle\tau\rangle}-E_F\right) \qquad (2.10)$$

where $\langle x\rangle=\int_{E_0}^{+\infty} g(E)x(E)f_0(E)dE\,/\int_{E_0}^{+\infty} g(E)f_0(E)dE$ is the average value of an arbitrary function *x(E)* over the equilibrium carrier distribution. The explicit expression of the diffusive Seebeck coefficient can be computed through the following equation [62]:

$$\alpha = \mp\frac{k_B}{e}\left(\frac{(r+(D/2)+1)F_{r+D/2}(\eta)}{(r+(D/2))F_{r+D/2-1}(\eta)}-\mu\right) \qquad (2.11)$$

The behavior of $|\alpha|$ versus the reduced Fermi level, η, for different energy dependence of the DOS and relaxation time (D and r, respectively) is then plotted in Figure 2.9(b). As the average energy should be weighted by the relaxation time, according to Eq. (28), the increase in the scattering constant r will similarly increase $|\alpha|$. Hence, $|\alpha|$ would be larger if, say, weakly ionized impurity scattering ($r = +3/2$) rather than phonons scattering ($r = -1/2$) dominates [62].

One way of manipulating the relaxation time was through the use of resonant scattering. According to Ravich et al. in ref. [2], resonant scattering occurs when electrons in the allowed energy band of the host material are trapped in the quasi-local states of impurity atoms before they are ejected after a finite period of time . The total relaxation time near the resonant energy range can subsequently be affected, leading to a possible increase or decrease in the energy dependence of the total relaxation time and $|\alpha|$ [62].

An interesting enhancement of α^2n was recently reported in bulk p-type PbTe doped with Tl by Heremans et al. [51]. In this case, instead of quantum confinement effects, *resonant states* [84] formed due to the interaction of the Tl with the valence band of PbTe leads to an increase in the D.O.S near the band edge, as illustrated in Figure 2.7(c). Optical measurements on 1.5% Tl–PbTe sample indicated that the resonant states were located ~0.06 eV below the band edge, and increase the D.O.S by a factor of 2.6 above the bulk value. Electrical and thermal measurements showed a higher $\alpha^2\sigma$ for the 2% Tl–PbTe sample, but with the same κ as a Na–PbTe control sample, which led to the doubling of ZT near 800 K as shown in Figure 2.7(d) [46,51,62].

2.3 Bismuth-based chalcogenide thin films

2.3.1. Advantages of thin-film thermoelectric devices

Thin film TE devices offer some distinctive advantages. First, a thin film device has the natural advantage of a small volume (thickness of ≤ 10 μm, length and width of ~100 μm) as compared to size of millimeters for a bulk TE couple. As a result, thin film TE cooling can be integrated into microelectronic systems (Figure 2.10a). In principle the bulk device can be scaled down to micro sizes, however fabrication processes to do so are difficult.

Second, thin-film devices have a much shorter response time than bulk devices, as shown in Figure 2.10(c) [1]. The thin film device achieves the steady state in 15 μs, while the bulk device requires 0.35s [1]. This is a result of the response time associated with the transport of heat through the thin film (micrometers) rather than through the millimeters associated with bulk devices.

Third, the thin film device has the ability to handle much larger density of heat pumping power than does the bulk device. Typically, bulk devices are working with pumping power density lower than 10 W/cm^2, however the pumping power density in a thin-film device is on the order of hundreds of W/cm^2 [85]. Figure 2.10(d) illustrates a comparison TE module performance chart, in which the load line represents the ΔT and power pumped conditions possible for a given TE module drive current [86]. At the maximum drive current for the module, the load line is generated from two key parameters: (1) the maximum power the device can pump, Q_{max}; and, (2) the maximum temperature difference that the device can sustain between its top and bottom substrates, ΔT_{max}. For a commercial example, under a given drive current, a eTEC^{TM} Series thin film TE module (Laird technology) possesses a larger pumping power up to ten times (Figure 2.10e) and a comparable the maximum temperature difference ΔT_{max} as compared to the conventional bulk TE modules [86].

Fourth, the granular structure–morphology of thin films increases the grain boundary scattering which is helpful for suppressing κ and enhanced ZT values. Figure 2.10(b) represents the roles of grain orientation and grain size in carrier mobility. The grains with the same colors illustrate that they have the same/similar orientations. The grain boundary scattering in Figure 2.10b(i) will be greater than that of the Figure 2.10b(ii) case because of its smaller grain size and the greater grain disorientation. The effective mobility is given by [87]:

$$\mu_g = \frac{Lq}{\sqrt{2\pi m^* kT}} \exp\left(-\frac{\phi_b}{kT}\right) \qquad (2.12)$$

where q is the carrier charge, m^* is the effective mass, k is the Boltzmann constant, T is the temperature, and ϕ_b is the grain boundary potential barrier in the depletion region [87,88]. In polycrystalline silicon, the potential barrier height is approximately twice as high at random boundaries as at low-energy coincidence boundaries [88].

2.3.2. Thermoelectric properties of Bi_2Te_3-based thin films

In the 1950s alloys of Bi_2Te_3 were discovered and then developed to have ZT~1 near room temperature [2,3]. It was quickly realized that alloying with Sb_2Te_3 and Bi_2Se_3 allowed for the fine tuning of the carrier concentration alongside a reduction in lattice thermal conductivity. These compounds have played a dominant role in the field of thermoelectrics through today. The traditional cooling materials are alloys of Bi_2Te_3 with Sb_2Te_3 (such as $Bi_{0.5}Sb_{1.5}Te_3$; p type) and of Bi_2Te_3 with Bi_2Se_3 (such as $Bi_2Te_{2.7}Se_{0.3}$; n type), with a ZT at room temperature approximately equal to one [3].

The crystal structures of Bi_2Se_3 and Bi_2Te_3 are usually described by a hexagonal cell that consists of 15 layers of atoms stacking along the c-axis with a sequence shown below [2], as shown in Figure 2.11.

$\cdots\ Se^{(1)}–Bi–Se^{(2)}–Bi–Se^{(1)}\ \cdots\ Se^{(1)}–Bi–Se^{(2)}–Bi–Se^{(1)}\ \cdots\ Se^{(1)}–Bi–Se^{(2)}–Bi–Se^{(1)}\ \cdots$,

and $\cdots Te^{(1)}–Bi–Te^{(2)}–Bi–Te^{(1)} \cdots\ Te^{(1)}–Bi–Te^{(2)}–Bi–Te^{(1)} \cdots Te^{(1)}–Bi–Te^{(2)}–Bi–Te^{(1)}\ \cdots$

The superscripts refer to two different types of bonding for Se or Te atoms. The 5-atomic-layer thick lamellae of $–(Se^{(1)}–Bi–Se^{(2)}–Bi–Se^{(1)})–$ or $–(Te^{(1)}–Bi–Te^{(2)}–Bi–Te^{(1)})–$ is called quintuple layers, QLs. The $Se^{(1)}…Se^{(1)}$ or $Te^{(1)}…Te^{(1)}$ refers Van der Waals force between Se or Te atoms, whereas the $Se^{(1)}–Bi$ and $Bi–Se^{(2)}$ or $Te^{(1)}–Bi$ and $Bi–Te^{(2)}$ are ionic-covalent bonds. This weak binding between the $Se^{(1)}$ – $Se^{(1)}$ or $Te^{(1)}…Te^{(1)}$ accounts for the ease of cleavage along the plane perpendicular to the *c*-axis and the anisotropic thermal and electrical transport properties of Bi_2Se_3 and Bi_2Te_3. For example, the thermal conductivity along the plane perpendicular to the *c*-axis (~1.5 $Wm^{-1}K^{-1}$) is nearly twice that of the value along the *c*-axis direction (~0.7 $Wm^{-1}K^{-1}$) [2,3,64].

Thin-film technology is advantageous for obtaining nanocrystalline and nanostructured materials by adjusting deposition conditions and subsequent thermal treatments. The extensive phonon scattering at grain boundaries in the nanostructures causes a large reduction in thermal conductivity, while maintaining reasonable electrical conductivity, leading to enhanced ZT. Therefore, nanocrystalline and nanostructured Bi_2Te_3-based thin films have recently attracted great interests because of their superior TE performance [11,12,16,17,28,29,31,39]. The layered–hexagonal Bi_2Te_3 films fabricated using radio-frequency magnetron sputtering possessed a PF of 8.8 $\mu Wcm^{-1}K^{-2}$ for an (015)-oriented film, and a PF of 33.7 $\mu Wcm^{-1}K^{-2}$ for a highly (00l)-oriented layered film [28,29]. Furthermore, PFs of 27 $\mu Wcm^{-1}K^{-2}$ and 39.9 $\mu Wcm^{-1}K^{-2}$ were measured for smooth-epitaxial- and hexagonal-Bi_2Te_3 films grown using MBE [37] and co-evaporation [89], respectively.

Despite fewer studies performed on thermoelectric Bi_2Se_3 as compared to Bi_2Te_3, a considerable amount of recent efforts to enhance TE performance has been devoted to the synthesis of Bi_2Se_3 nanostructures such as hexagonal flakes (PF ≈ 0.28 $\mu Wcm^{-1}K^{-2}$) [14] and nanoflakes (PF ≈ 0.97 $\mu Wcm^{-1}K^{-2}$) [15], using the solvo-thermal method and chemical bath deposition, respectively. Moreover, the Bi_2Se_3 film grown by metal organic-chemical vapor deposition has been reached a PF = 5.8 $\mu Wcm^{-1}K^{-2}$ [35]. To our best knowledge, however, a systematic investigation of PLD growth and characterization of TE Bi_2Se_3 thin films has not been reported yet. Furthermore, due to the larger difference in vapor pressure between Se and Bi ($P_{Se} > P_{Te} > P_{Bi}$, Figure 2.12a [21]), Bi_2Se_3 is considered a suitable candidate material for investigating the effects of PLD deposition conditions on the compositions, structures–morphologies, and TE properties.

In PLD, tightly controlling substrate temperatures (T_s) and ambient pressures (P) enables the morphologies and compositions of films to be manipulated extensively, which offers a new method for enhancing the TE properties of films

[17,20,38,39,90]. For example, self-assembled Bi_2Te_3 films featuring well-aligned zero- to three-dimensional nanoblocks have been fabricated (Figure 2.13-i), but the room-temperature PFs of these films remain low ($\leq$ 1.9 $\mu Wcm^{-1}K^{-2}$) [39]. By contrast, A. Li Bassi et al. [17] obtained several microstructured Bi_2Te_3 films (Figure 2.13-ii) with high PFs for morphologies: (A) layered-smooth (50.6 $\mu Wcm^{-1}K^{-2}$), and (B) compact-smooth (21.2 $\mu Wcm^{-1}K^{-2}$) at room-temperature; whereas the PFs remained low values of 8.8 $\mu Wcm^{-1}K^{-2}$ for 3D crystallite shapes and 0.08 $\mu Wcm^{-1}K^{-2}$ for 3D-voided platelets. Therefore, the interrelationships between PLD processing conditions, microstructures, and TE properties of Bi_2Te_3-based thin films must be understood comprehensively.

2.3.3 Thermal conductivity κ of Bi_2Se_3 and Bi_2Te_3 alloys

A transient 3ω technique is usually employed in measuring thermal conductivity of thermoelectric films. The detail of this technique can be found in refs. [12,85,91].

Table 2.1 summarizes thermal transport properties (at room–temperature) of nanocrystalline–nanostructured Bi_2Te_3-based thin films and bulk materials in the literature. Generally, the thermal conductivity κ value for polycrystalline films is expected to be smaller than that of bulk alloys because of the contribution of grain boundary scattering [2,11,92]. Moreover, the κ of nanocrystalline Bi_2Te_3-based films will further decrease when the grain size of decreases ($\kappa \leq 0.81$ W/mK, Figure 2.14A) [12,16]. For Bi_2Te_3/Sb_2Te_3 superlattice films, the coherent backscattering of phonon waves at the superlattice interfaces is outlined for the reduction of lattice thermal conductivity, resulting in the low κ ≤ 0.4 W/mK [93,94].

For PLD Bi_2Te_3-based films, Yamasaki et al. [93] measured thermal conductivity with an ac calorimetric method in the direction across the film, obtaining κ ~ 1.1 W/m K for a Bi_2Te_3 film deposited by PLD in vacuum (Table 2.1). In addition, Walachova et al. [95] estimated κ starting from direct ZT measurement with the Harman method and found a value of about 0.2 – 0.3 W/mK for films with a thickness comparable to our films (>100 nm). Recently, Chang et al. [13] reported the κ between 0.93 and 1.16 W/mK for $Bi_xSb_{2-x}Te_3$ films with the similar morphologies to our films (Figure 2.14B). The reported κ (at 300 K) of hexagonal flake Bi_2Se_3 was 0.75 W/mK). From these relevant reports, thermal conductivity of the present Bi_2Te_3 and Bi_2Se_3 films can be roughly estimated at 1.1 W/mK.

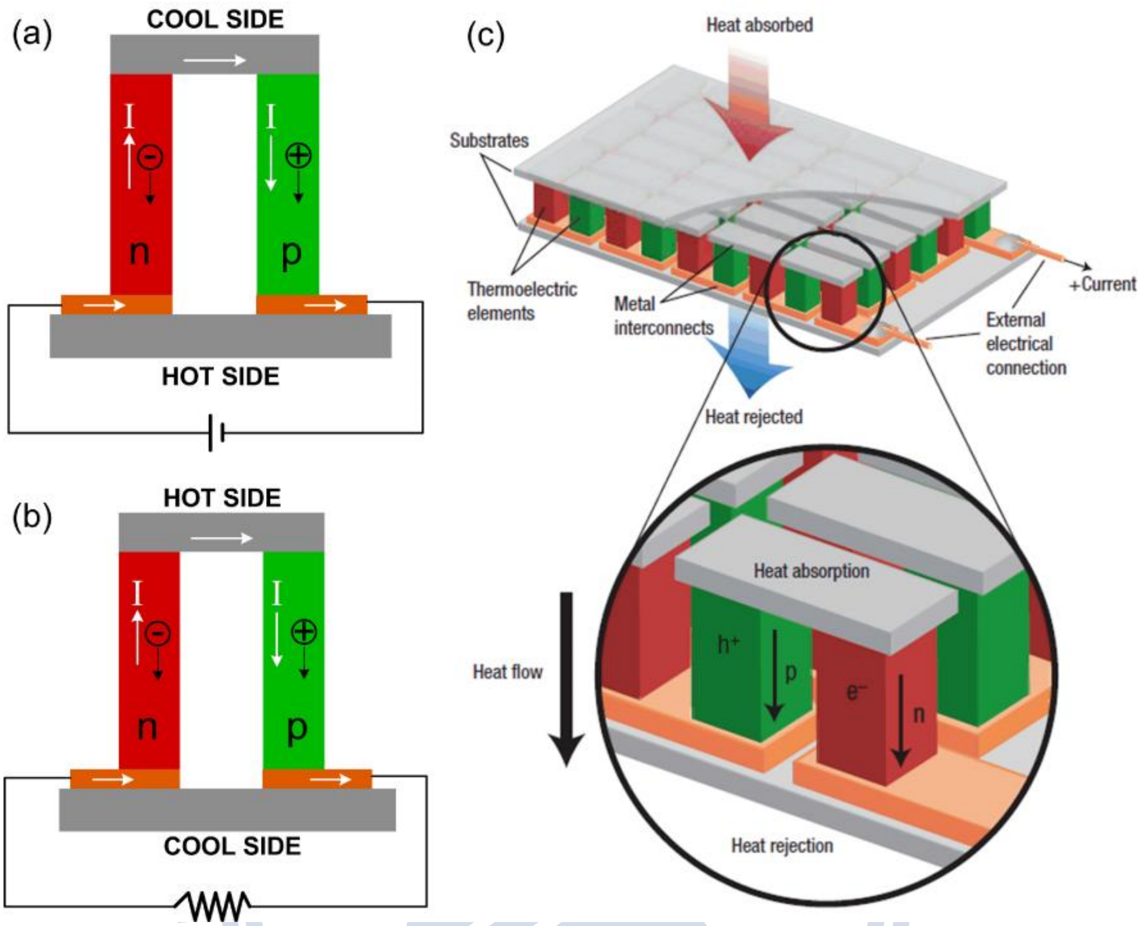

Figure 2.1 Illustration of TE devices: (a) cooler (Peltier effect), (b) power generator (Seebeck effect). Redrawn after ref. [42]. Thermoelectric module showing the direction of charge flow on both cooling and power generation [4].

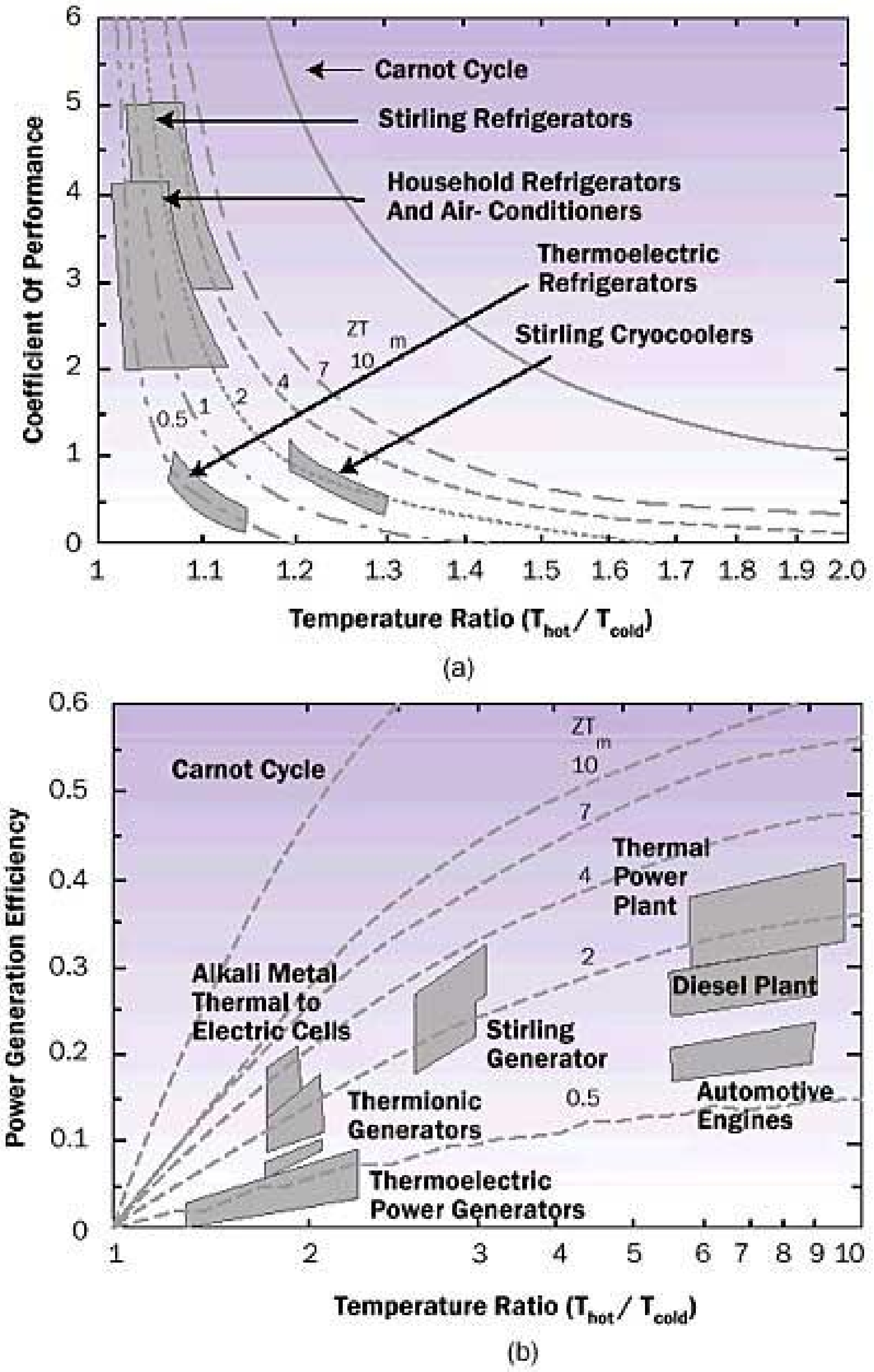

Figure 2.2 Comparison of thermoelectric technology with other energy conversion methods for (a) cooling and (b) power generation [42,45].

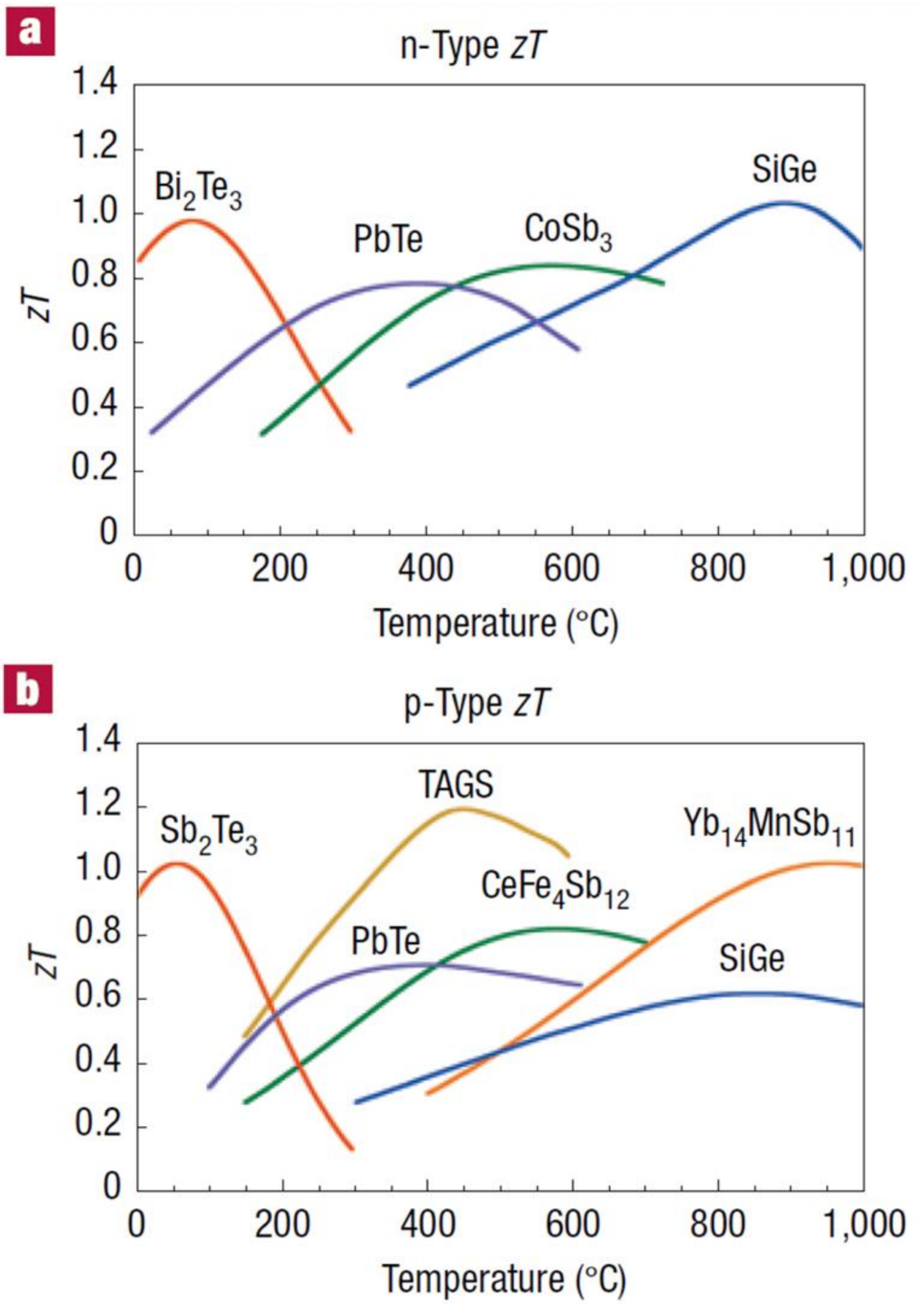

Figure 2.3 Figure-of-merit ZT of (a) n-type and (b) p-type state-of-the-art commercial materials and those used or being developed by NASA for thermoelectric power generation. Most of these materials are complex alloys with dopants; approximate compositions are shown [4].

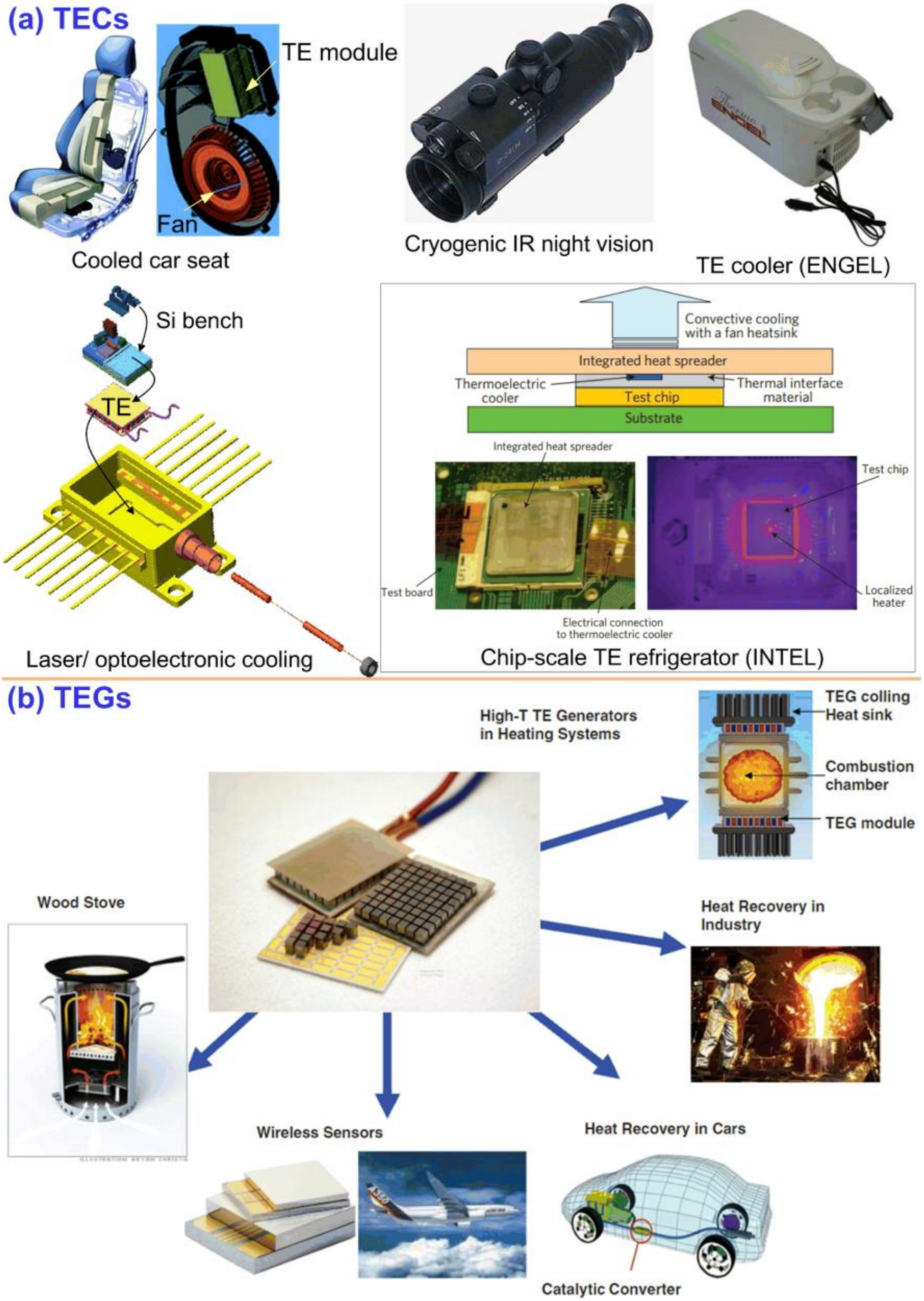

Figure 2.4 Overview of potential thermoelectric cooling (TEC) and thermoelectric generator (TEG) applications [55,56].

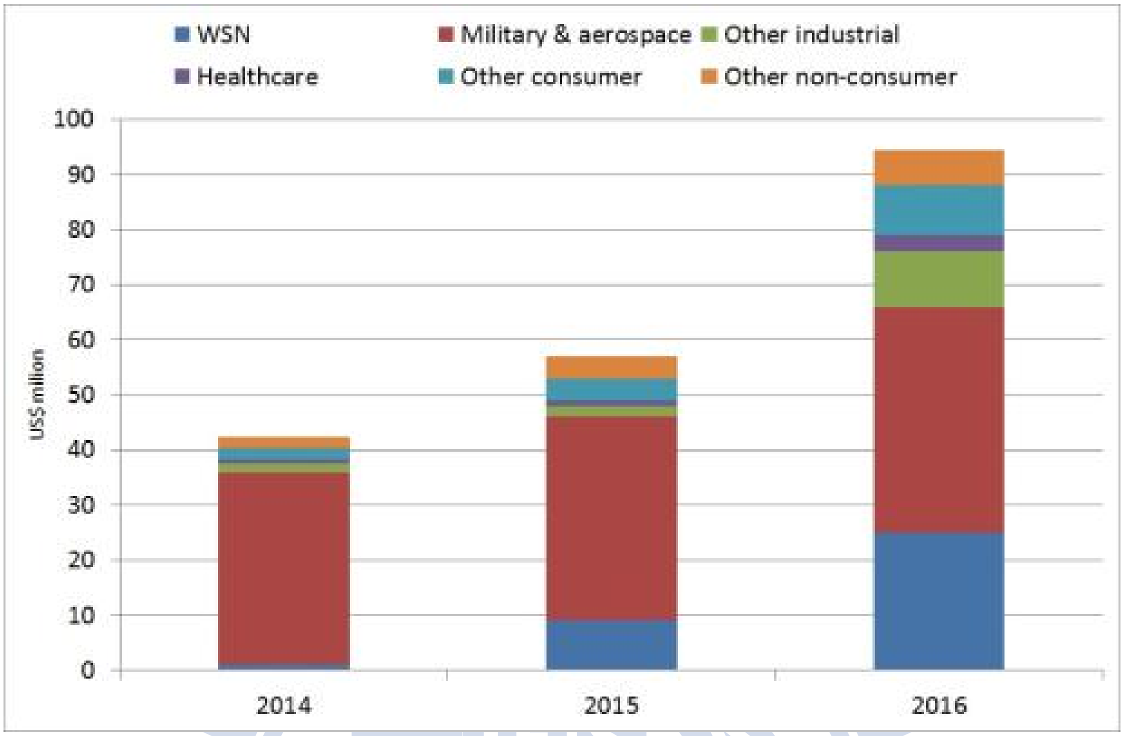

Figure 2.5 Market forecasts for thermoelectric energy harvesters (US$ million), source IDTechEx [59].

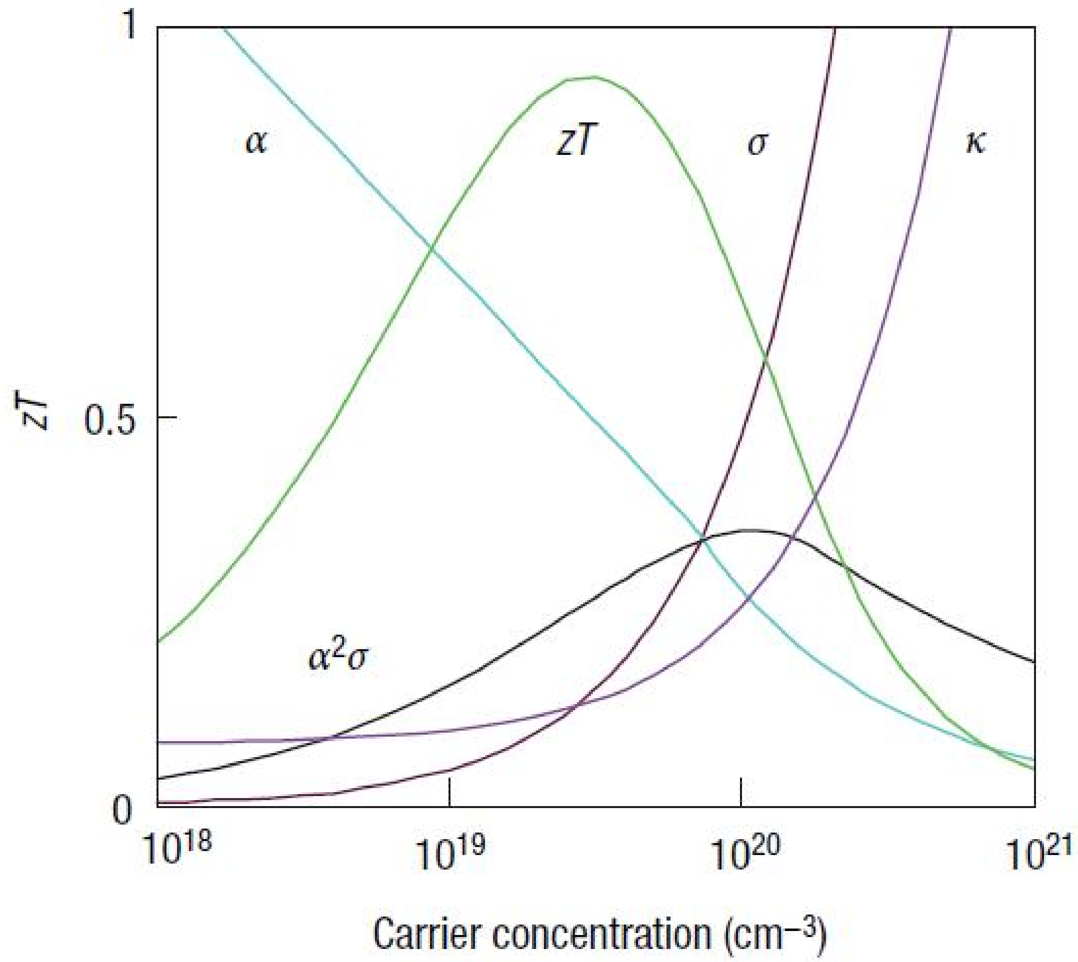

Figure 2.6 Maximizing the efficiency (ZT) of a thermoelectric involves a compromise of thermal conductivity (κ; plotted on the y-axis from 0 to a top value of 10 $Wm^{-1}K^{-1}$) and Seebeck coefficient (*S* or α; 0–500 μVK^{-1}) with electrical conductivity (σ; 0–5000 $\Omega^{-1}cm^{-1}$) [4].

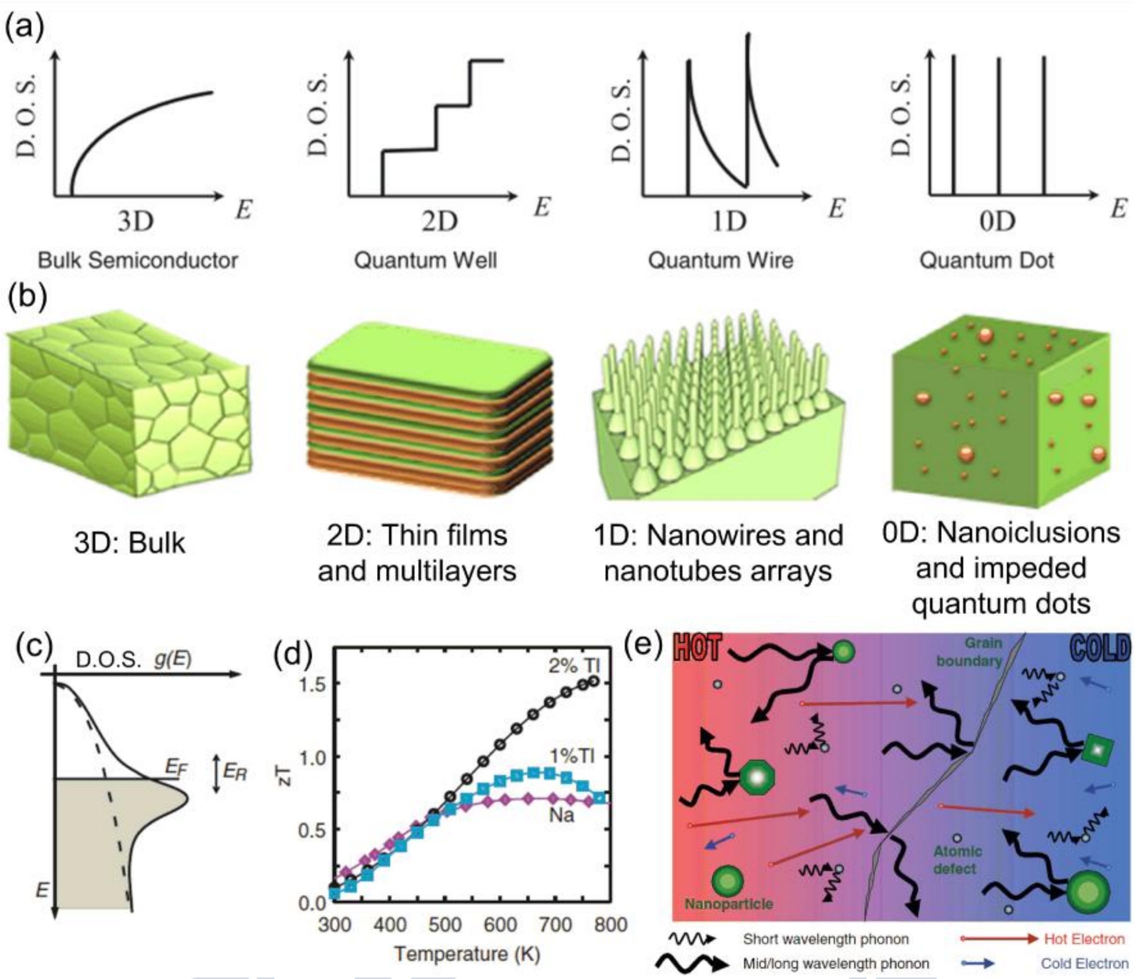

Figure 2.7 (a) Electronic density of states (D.O.S.) for a bulk 3D crystalline semiconductor, a 2D quantum well, a 1D nanowire or nanotube, and a 0D quantum dot [67]. (b) Examples of different nanostructuring with different dimensionalities [65]. (c) A spike in the density of states (solid line) above the bulk value (dashed line) occurs due to resonant states in Tl-doped PbTe [51]. (d) The measured ZT of Tl-PbTe and Na-PbTe samples for 300–800 K indicates an improvement due to the addition of Tl [51]. (e) Schematic diagram illustrating various phonon scattering mechanisms within a thermoelectric material, along with electronic transport of hot and cold electrons [70].

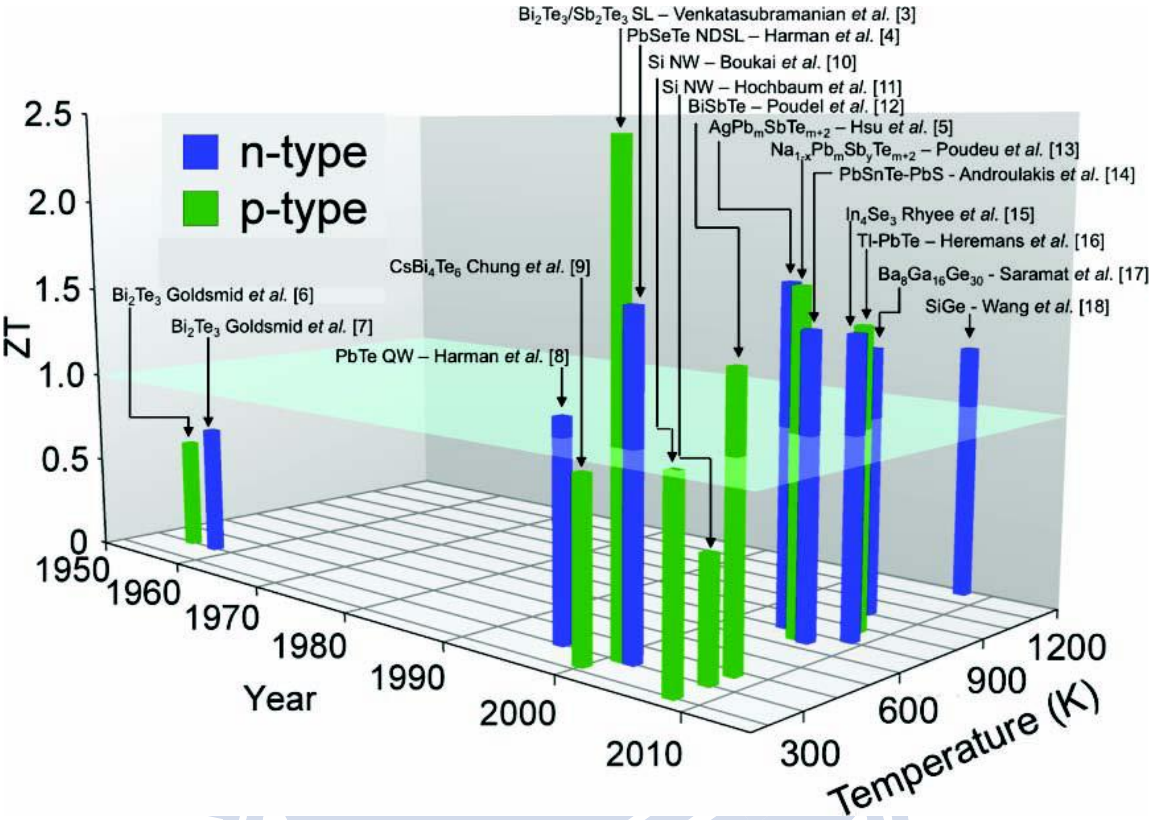

Figure 2.8 Thermoelectric figure-of-merit ZT as a function of temperature and year illustrating important milestones [70]. Although there have been several demonstrations of ZT > 1 in the past decade (2001 – 2010), no material has yet achieved the target goal of ZT ≥ 3. The material systems that have achieved ZT > 1 have all been based on some form of nanostructuring.

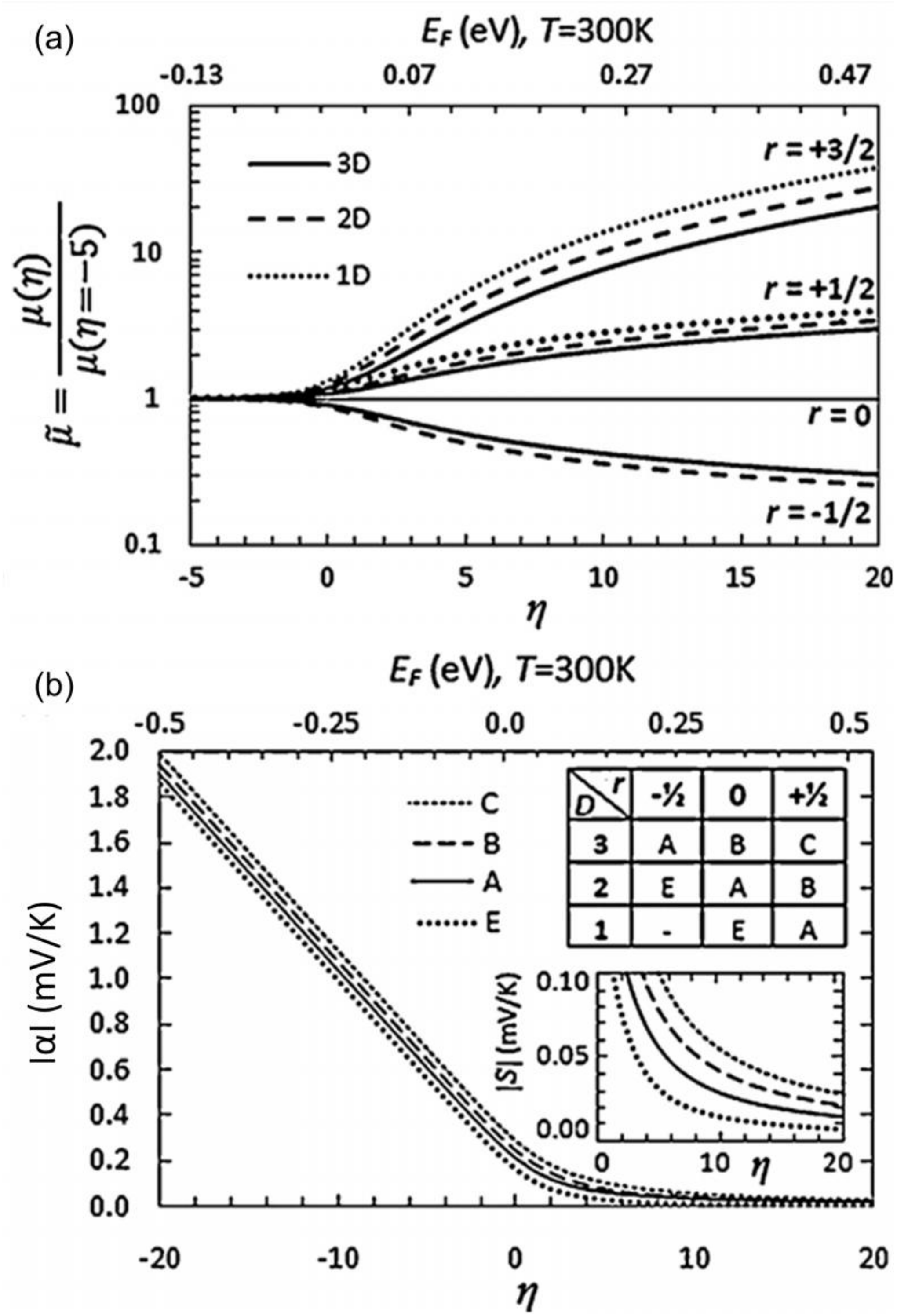

Figure 2.9 (a) Normalized mobility and (b) |α| as a function of the reduced Fermi level, η [62]. Equivalent value of E_F at 300 K is labeled on the top horizontal axis.

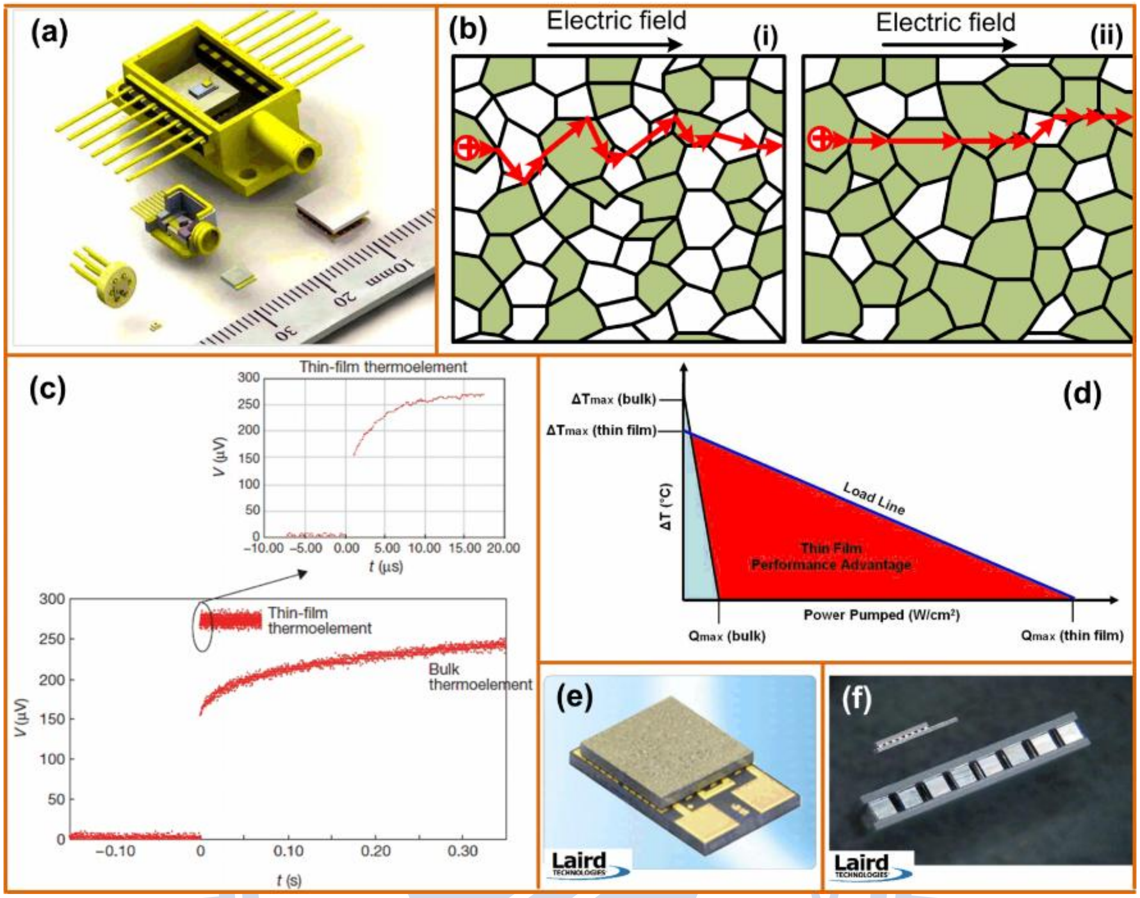

Figure 2.10 (a) An example for optoelectronics of the continuing reduction in package size. (b) A schematic of grain boundary scattering for thin–film materials with (i) disoriented–small grains, and (ii) highly oriented–large grains. (c) The comparison of thermal/cooling time response of thin-film (~5 μm) superlattice device and a bulk device [1]. (d) Thermoelectric modules performance chart which presents the temperature drop ΔT vs. pumping power [86]. (e) A commercial thin film TE module. (f) Size comparison between a thin film TE device and bulk TE device [86].

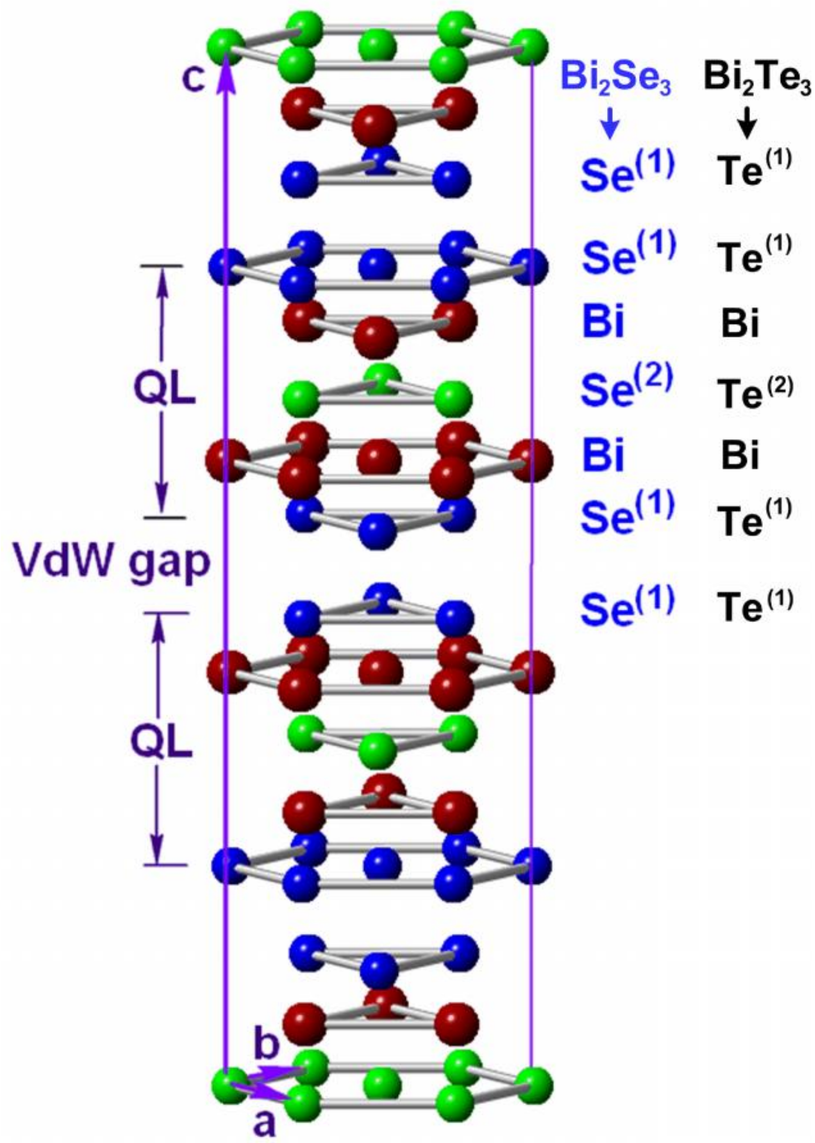

Figure 2.11 The hexagonal structures of one unit cell of Bi_2Se_3 and Bi_2Te_3.

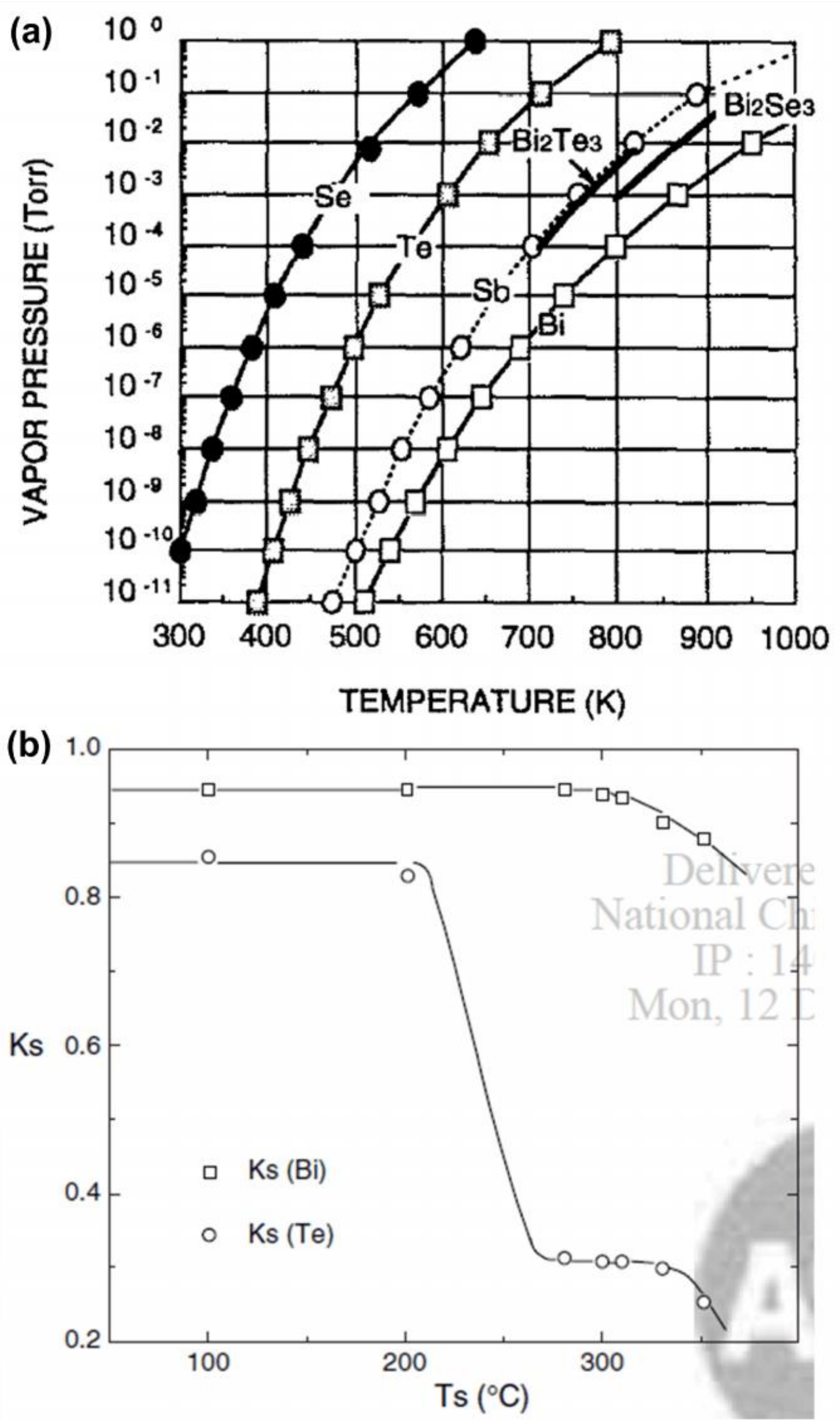

Figure 2.12 (a) Vapor pressures of Bi, Sb, Te, Se, Bi_2Se_3, and Bi_2Te_3 as a function of temperature [21]. (b) The variation of sticking coefficient K_s (Bi, Te) as a function of substrate temperature T_s at fixed flux ratio F_R = 4.5 [24].

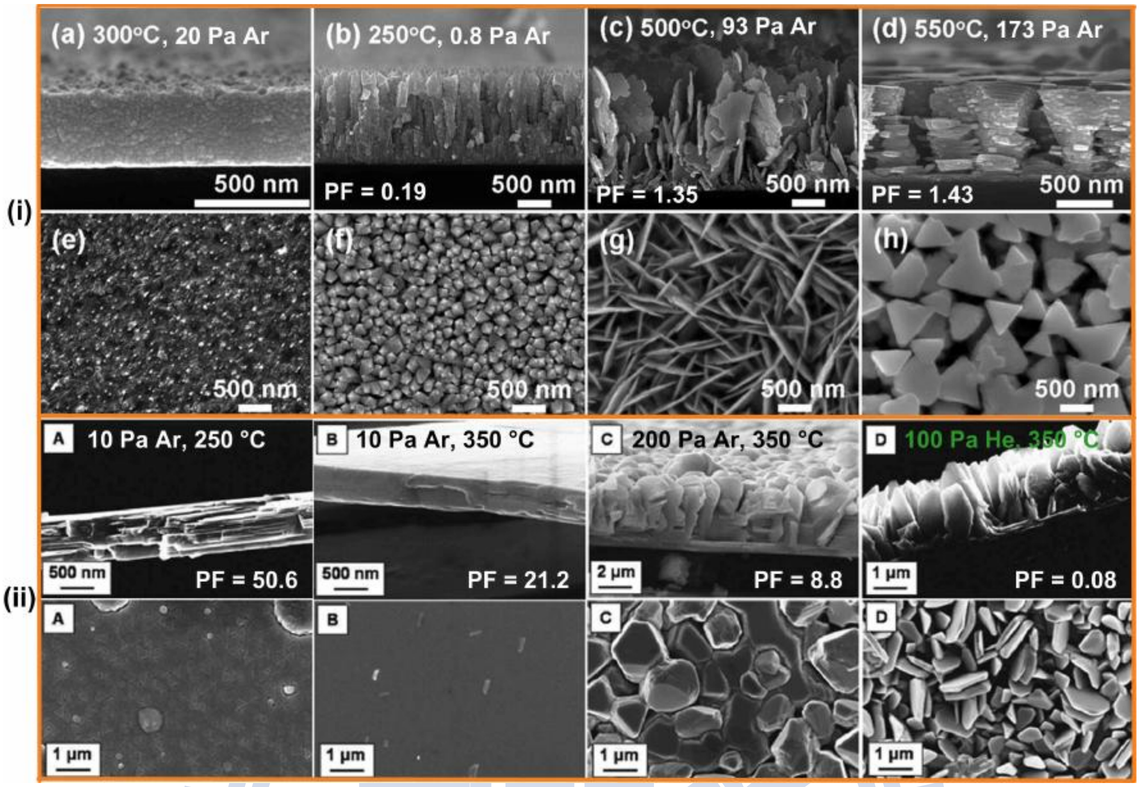

Figure 2.13 The morphology and power factor (unit $\mu Wcm^{-1}K^{-2}$) of nano/micro-structured Bi_2Te_3 thin-films grown by PLD at various substrate temperatures and ambient pressures, reported by (i) Chang and Chen [39] and (ii) Li Bassi et al. [17].

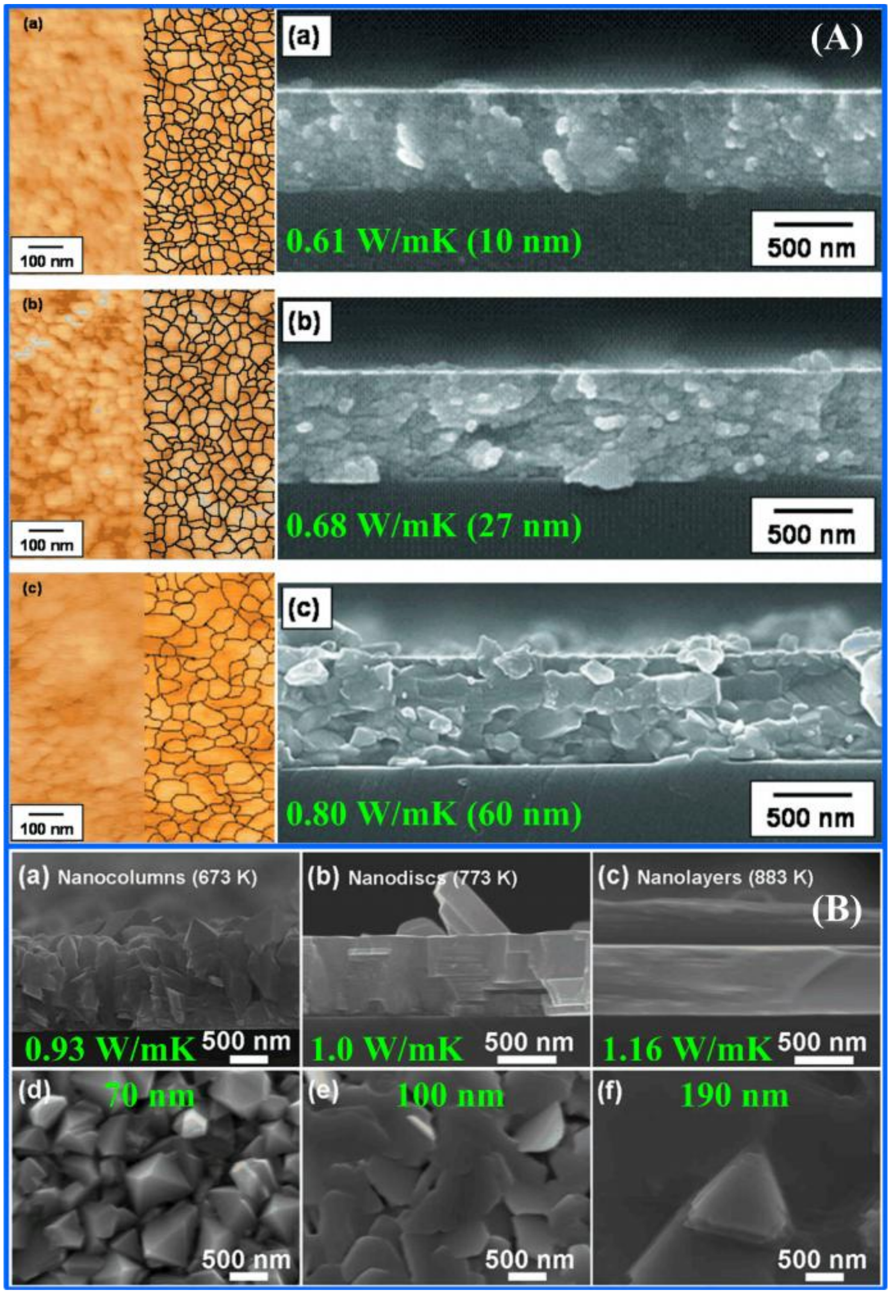

Figure 2.14 The morphology and thermal conductivity of Bi_2Te_3-based films with different grain sizes: (A) nanocrystalline $Bi_2Te_{3-x}Se_x$ films [16], (B) the $Bi_xSb_{2-x}Te_3$ films [13].

Table 2.1 Room–temperature thermal transport properties of nanocrystalline–nanostructured Bi_2Te_3-based thin films and bulk materials in the literature, included: sample and fabrication method, average grain size, thermal conductivity κ, electrical conductivity *σ*, Seebeck coefficient *α*, power factor PF (= $\alpha^2\sigma$), and ZT (at 300 K).

Sample, fabrication method	**Avg. grain size**	**κ (W/m K)**	**σ (S/cm)**	**α (μV/K)**	**PF = $\sigma\alpha^2$ ($\mu W/cmK^2$)**	**ZT (300 K)**	**Ref.**
$Bi_2Te_{2.7}Se_{0.3}$ nanocrystalline thin film, flash evaporation	60 nm	0.8 (cross-plane)	540	−186.1 (in-plane)	18.7 (in-plane)	0.7	[11]
Sintered bulk $Bi_2Te_{3-x}Se_x$ material, hot-pressing	30 μm	1.6	930	−177.5	29.3	0.6	
Nanocrystalline bismuth-telluride-based ($Bi_2Te_{3-x}Se_x$) thin film	10 nm	0.61	550	−84.0	3.9	0.19	[16]
	27 nm	0.68	540	−138.1	10.3	0.46	
	60 nm	0.80	540	−186.1	18.7	0.70	
Nanocrystalline Bi-Sb-Te thin film, sputtering	26 nm	0.46	3.3	–	–	–	[12]
	45 nm	0.65	6.7	–	–	–	
	84 nm	0.81	33.3	–	–	–	
Nanocrystalline BiSbTe (8:30:62) thin film, flash evaporation	150 nm	0.6	–	–	–	–	[92]
Single crystal BiSbTe bulk alloys	–	0.75	–	–	–	–	[2]
Bi_2Te_3/Sb_2Te_3 superlattices (period~5 nm)	–	0.4	–	–	–	–	[94]
$Bi_2Te_{3+0.63}$ bulk	–	2.2	1000	−240	58	0.87	[2]
$Bi_2(Te_{0.95}Se_{0.05})_3$ bulk	–	1.59	901	−223	45	0.85	[2]
$Bi_2Te_3/Bi_2(Te_{0.88}Se_{0.12})_3$ superlattice film, MBE	80 nm	1.25	639	−204	27	0.60	[37]
Bi_2Te_3 film, PLD	–	1.1	–	–	–	–	[93]
Bi_2Te_3/Sb_2Te_3 superlattices film (layered thickness ~ 6 nm), PLD.	–	0.11	–	–	–	–	
Bi_2Te_3 films, laser ablation	–	0.2– 0.3	–	–	–	–	[95]
$Bi_xSb_{2-x}Te_3$ nanolayer film, PLD	190 nm	1.16	2700	95	25	0.65	[13]
$Bi_xSb_{2-x}Te_3$ nanodisc film, PLD	100 nm	1.00	1100	132	20	0.60	
$Bi_xSb_{2-x}Te_3$ nanocolumn film, PLD	70 nm	0.93	280	207	12	0.39	

Chapter 3 Experimental Details

In order to investigate and optimize the thermoelectric properties of Bi-based (i.e. Bi_2Se_3 and Bi_2Te_3) thin films grown by PLD, the designed experiments of this thesis were performed, as briefly illustrated in the flowchart (Figure 3.1).

3.1 The PLD growths of thermoelectric Bi_2Se_3 and Bi_2Te_3 thin films

3.1.1 Introduction to the PLD system

PLD is one of the most convenient thin film growth techniques that uses a high intensity pulsed laser beam as an external energy source to ablate a target, form a plume, and deposit thin films onto a substrate. Figure 3.2 shows the PLD system for preparing thermoelectric Bi_2Se_3 and Bi_2Te_3 thin films in this dissertation. The substrate was heated and maintained at desired T_s using a thermocouple and a proportional-integral-derivative temperature controller. The thermocouple was buried inside a stainless-steel substrate holder which was heated by a tungsten lamp just behind the holder. The pressure of ambient gas (He/Ar) could be fine-tuned by the needle valve. Also, a KrF excimer laser beam ($\lambda = 248$ nm, pulsed duration 15–20 ns, repetition rate of 5 Hz, and fluence of 3.8 J/cm^2) was guided by several UV mirrors and focused on a stoichiometric polycrystalline target (Bi_2Se_3 or Bi_2Te_3) inside the vacuum chamber by the UV lens. The target-to-substrate distance was 40 mm. During the deposition of Bi_2Se_3 films, pure (6N) He/Ar gas was introduced into the vacuum chamber, which was evacuated to a base pressure of 4×10^{-4} Pa (or 3×10^{-6} Torr) and maintained at a certain constant pressure (P), using a differential evacuation system.

3.1.2 Substrate surface cleaning and preparation

The surface of the substrate should be atomically clean and free from impurities because the contaminants can interact with the thin films being deposited and substantially degrade its quality and adhesion to the substrate. The presence of unwanted surface contaminants can also influence the growth and orientation of the films in an undesired manner. In our experiments, an approximately 300-nm-thick SiO_2 layer was thermally grown on the Si wafers (thickness 525 μm) for electrical isolation purpose. The wafers were cut into 1.5 cm × 1.5 cm substrates. The substrates were cleaned with acetone to dissolve any contaminants adhering to the surface such as grease, oils, etc. This was followed by rinsing with methanol to remove any residues left behind after cleaning with acetone. Afterward, the substrates were rinsed in distilled water and dried with nitrogen flow. The substrates were then used for the deposition of thermoelectric thin films.

3.1.3 Deposition process

For Bi_2Se_3 thin films, the depositions were at T_s of 200–350 °C and helium ambient pressure (P) of 0.7–173 Pa. The number of laser pulses was 9,000 and deposition took 30 min. The average growth rate was approximately 0.46 Å/pulse. For the growths of Bi_2Te_3 thin films, T_s was varied from room-temperature (30 °C) to 380°C and Ar ambient pressure (P_{Ar}) was at 80 Pa. The number of laser pulses was 12,000 and deposition took 40 min. The average growth rate was approximately 0.52 Å/pulse.

3.2 Characterization of key properties

3.2.1 Structural characterizations

X-ray diffraction: The orientation and crystallinity of Bi_2Se_3 and Bi_2Te_3 films were determined using X-ray diffraction (XRD, Bruker D8) with $CuK_{\sim}$ radiation (λ = 1.5406 Å) in $2^{-} - \mu$ and rocking-curve (ω-scan) configurations.

Transmission electron microscopy (TEM): To collect detailed the structural quality on the films and grain boundaries, digital images from a high-resolution transmission electron microscope (HR-TEM) (Philips Tecnai F20), operated at 200 kV, were recorded using a Gatan 2k ×2k charged couple device camera. The specimens were prepared using a standard procedure of mechanical thinning and Ar-ion milling. The TEM analysis was done by Gatan Digital Micrograph software.

3.2.2 Morphology and film thickness

Field-emission scanning electron microscopy (SEM): Surface morphology and film thickness were examined using SEM (JEOL JSM-6500) through plane-view and cross-sectional images, respectively.

3.2.3 Composition and surface analysis

Energy-dispersive X-ray spectroscopy (EDS): Film compositions were also analyzed using an Oxford EDS equipped with the SEM instrument at an accelerating voltage of 15 kV, a dead time of 22% – 30%, and a collecting time of 60 s. The atomic percentage of each film was determined by averaging the values measured in 5 or more distinct 13 × 18 μm^2 areas on the surface of films.

3.2.4 Electrical properties

The in-plane electrical conductivity, carrier concentration and mobility were measured at room temperature using a Hall system (Bio-Rad HL5500PC) with van der Pauw geometry. Indium balls were used to improve ohmic contact on the films' surface.

In Hall Effect measurement (Figure 3.3), the resistivity is given by:

$$\circ = \frac{\text{®} \times t}{2.\ln 2}\left(\frac{V_{43}}{I_{12}} + \frac{V_{23}}{I_{14}}\right).F.Q \quad [\Omega cm]$$

where t is the thickness of the film, F and Q are the symmetry and correction factors, and I, V are current source applied to contacts and the voltage is measured across contacts (named by numbers, Figure 3.3), respectively.

The sheet resistance is defined as: $R_s = \circ / t \quad [\Omega / square]$

The sheet Hall coefficient: $R_{Hs} = \frac{V_h}{IB} \quad [m^2 / C]$

where V_h is the average value for all possible permutations of the contacts applied current and directions of magnetic field.

The sheet carrier concentration: $n = -\frac{1}{R_{Hs} e} \quad [cm^{-2}]$. This is negative for free electrons, for e is positive by definition.

One the thickness t is known, the carrier concentration can be calculated by

$$n = n_s / t \quad [cm^{-3}].$$

Hall mobility is given by: $\mu = R_{Hs} / R_s \quad [cm^2 / Vs]$

Conductivity *vs.* temperature $\sigma(T)$ values were measured using a Physical Property Measurement System (PPMS, Quantum Design) between 2 K and 300 K, applying the standard 4-probe technique and using silver paste for the contacts.

3.2.5 Seebeck measurement

Measurement of Seebeck coefficient at room-temperature was performed by a longitudinal DC steady-state method on specially designed setups for film, with $\alpha = \Delta V/\Delta T$, where ΔT is the temperature gradient across the sample, and ΔV is the thermo-emf generated by ΔT (Figure 3.4). At a given temperature, a programmable power supply was controlled by the LABVIEW graphical program to develop a small temperature gradient across the sample. Typically, ΔT is set in the range of 0.8 – 1.5 K monitored by a pair of T-type thermocouples. The resulting thermo-emf ΔV was continuously recorded by a digital voltmeter. By varying ΔT, a statistically averaged α value was derived from the slope of a ΔV vs ΔT plot [96].

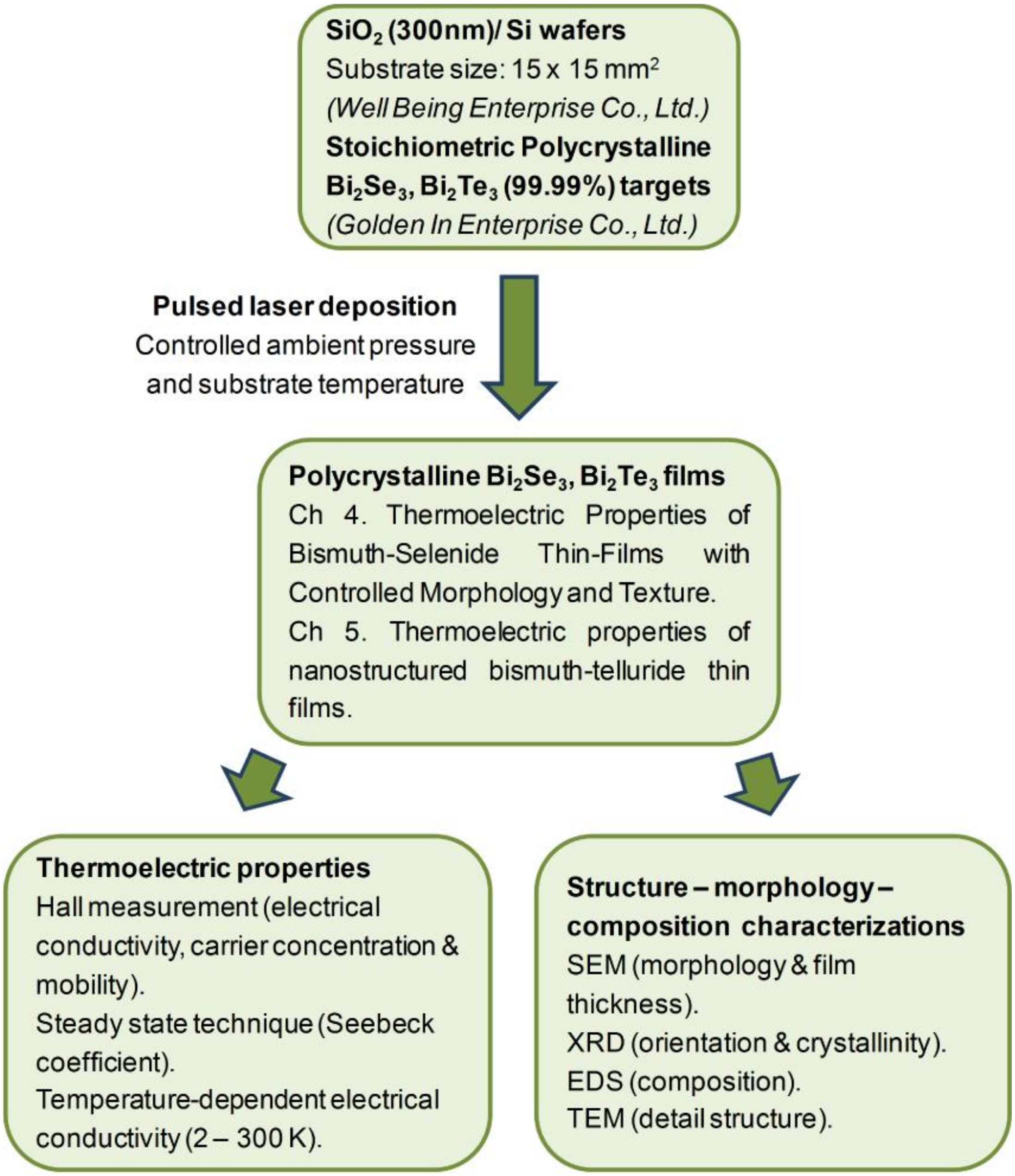

Figure 3.1 An experimental flowchart illustrating the experiment methods in this thesis.

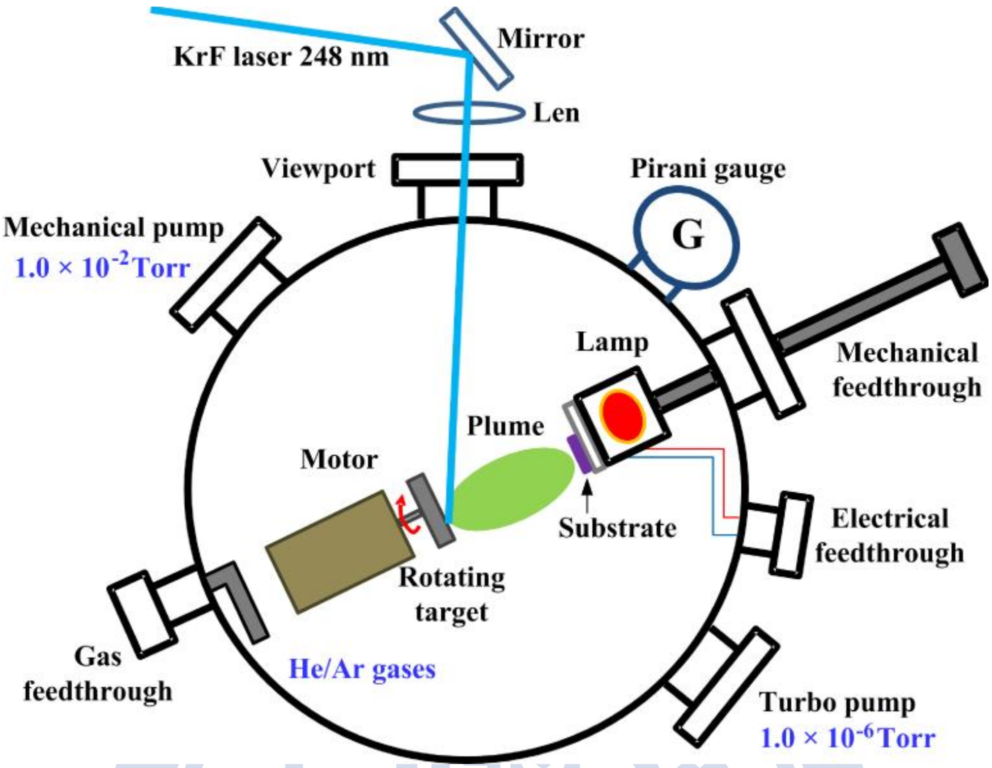

Figure 3.2 Schematic illustration of the PLD system

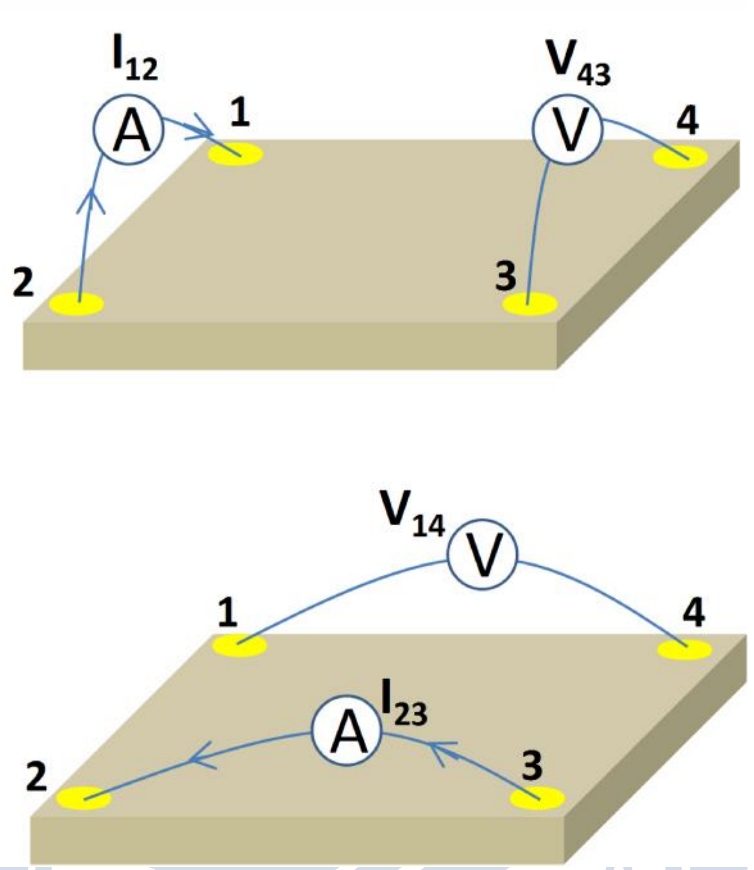

Figure 3.3 Schematic of a rectangular Van der Pauw configuration.

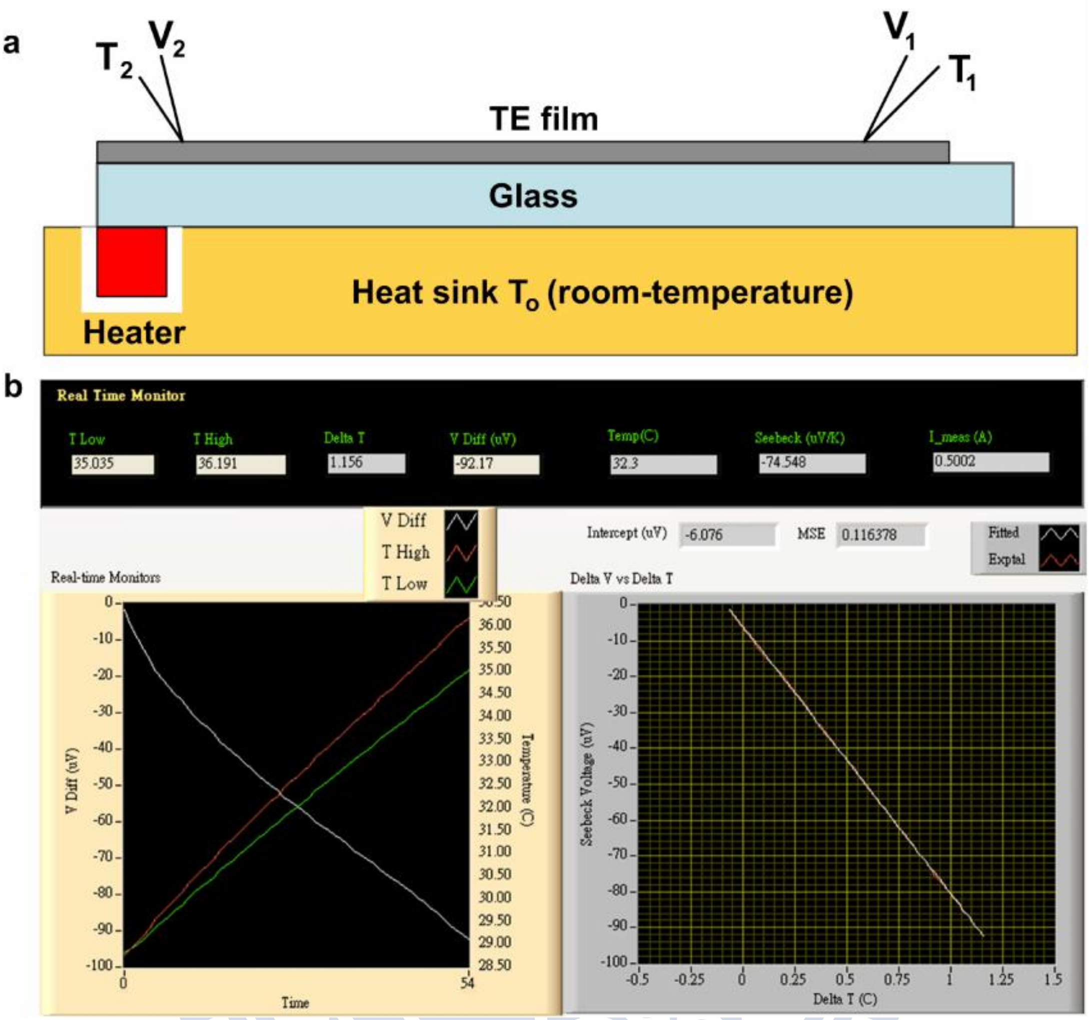

Real Time Monitor

T Low	T High	Delta T	V Diff (uV)	Temp(C)	Seebeck (uV/K)	I_meas (A)
35.035	36.191	1.156	-92.17	32.3	-74.548	0.5002

Intercept (uV) -6.076

MSE 0.116378

Figure 3.4 (a) Schematic setup for the Seebeck coefficient measurements on films. (b) A demonstrated Seebeck measurement result of a Bi_2Se_3 film.

Chapter 4 Thermoelectric Properties of Bismuth-Selenide Thin-Films with Controlled Morphology and Texture

4.1 Deposition temperature- and pressure-dependent crystal structure of Bi_2Se_3 films

Figure 4.1 shows the XRD patterns of selected Bi_2Se_3 films deposited at distinct T_s (at 6.7 or 40 Pa for the optimal crystallinity of films in group I, 0.7 Pa for group II). The presence of dominant (00ℓ) family planes (labeled from PDF#33-0214) clearly indicates that the films are highly c-axis oriented along the growth direction. The weak $Se^{(1)} - Se^{(1)}$ bond leads to a c-axis-favored crystal orientation that has the lowest surface energy [97] and enables the preferential formation of sheet-like structures [36]. Notably, the layered crystal structure offers poor thermal conductivity along the c-axis [2,3].

The (012) and (024) peaks of pure bismuth (identified by PDF#85-1331) were observed at 27.3° and 56.3°, respectively, for the films deposited at 0.7 Pa, but these peaks were absent when $P \geq 6.7$ Pa, indicating Bi segregation (observed as high Bi enrichment in the 0.7-Pa films; Figure 4.2). In addition to the dominant (00ℓ) orientation, the films deposited at 350°C showed the minor (10ℓ) orientation of the BiSe phase (PDF #29-0246). The existence of the major Bi_2Se_3 and the minor BiSe phases in films deposited at 350°C implies near-unity Se/Bi ratios in the films (more specifically, ratios ranging from 1.05 to 1.25; Figure 4.2); the structure of these films may possess double, covalently connected layers of bismuth –(Bi–Bi)– intercalating in VdW gaps between QLs, and alternating with 2 QLs [17,98,99].

The mosaic structure and crystallinity of the films were determined from the full width at half maximum (FWHM) of the (006) X-ray rocking curve (Figure 4.3). FWHM decreased with increasing T_s, indicating improved crystallinity and better orientation between the crystallites (grains). At any given T_s, the FWHM also depended on P. The optimal deposition pressure (the pressure at which the smallest FWHM was associated with the optimal crystallinity) changed from 6.7 Pa to 40 Pa as T_s was increased from 200–250°C to 300–350°C. The effect of strain on FWHM was neglected because the films were up to at least three hundred nanometers thick. Thus, the present FWHM characteristics can be explained by considering the orientation and sizes of the grains. Large grain sizes reduce the probability of misorientation of the grains and therefore diminish FWHM [100]. Here, the average grain size increased from approximately 100 to 500 nm when T_s was increased from 200°C to 350°C (Figure 4.4), leading to a drop in FWHM from approximately 10° to 2.7°. However, the narrowing of FWHM depended strongly on the orientation between crystallites (grains). Since the films deposited at 0.7 and 173 Pa were comparatively disoriented than those at 40 Pa, the FWHMs at 0.7 and 173 Pa were larger than at 40 Pa.

The detailed structure and orientation of the Bi_2Se_3 film deposited at 300°C and 40 Pa were characterized using an HR-TEM (Figure 4.5). A typical crystallite with size of approximately 150 nm was clearly presented in Figure 4.5a. The P1, P2, and P3 regions (Figure 4.5b), separated by the eye-guiding white lines (boundaries), revealed the granular-polycrystalline structure of the films. Moreover, P1 and P2 partly overlapped and the corresponding fast Fourier transform (FFT) of this overlapping region indexed by $\{003\}$ patterns of [0 1 0] zone axis was performed from the dashed-square area (Figure 4.5b, inset). The projected periods along the c-axes of both P1 and P2 were 9.60 Å, corresponding to (003) planes, which was close to the reported value of 9.55 Å in ref. [101]. The c-axis angle between P1 and P2 was approximately 20°, which is the misorientation between grains (platelets) that accounts for the large value of FWHM in Figure 4.3.

4.2 Deposition temperature- and pressure-dependent microstructure of Bi_2Se_3 films

Figure 4.4 shows the surface and cross-sectional morphology evolution of Bi_2Se_3 films prepared at various T_s in the 200–350 °C range and P in the 0.7–173 Pa range. At low pressure (0.7 Pa), films deposited at 200°C were smooth and compact (SC), with small crystals or droplets on the surface. These structures could further develop into 3-D step-and-terrace triangular-polygonal (TP) and super-layered flake (S-LFs) structures at T_s = 250°C and $T_s \geq$ 300°C, respectively.

At intermediate pressures (6.7 – 93 Pa), the films exhibited rice-like grain (RG) morphology (average grain, approximately 100 nm) at T_s = 200 °C and hexagonal platelets (HPs) at $T_s \geq$ 250 °C. The average size of HPs increased from 160 nm to 300 nm and 500 nm (approximate values) when T_s was raised from 250 °C to 300 °C and then 350 °C, respectively. At a high pressure (173 Pa), the films showed clear columnar structures, and became less dense because of the presence of nano- and submicro-voids between grains. The columnar structures were formed by the stacking of (1) RGs at $T_s = 200$ and 250°C; (2) the approximately 25-nm-thick L-HPs grown from bottom to top at T_s = 300°C; and (3) the approximately 38-nm-thick and misoriented L-HPs at T_s = 350 °C. We noted that under the same deposition temperatures, films tended to become thicker when P was increased.

The deposition parameters (P, T_s) affect the nucleation and growth of the films. After Bi and Se atoms were deposited on the substrate surface, nucleation (the formation of a single stable nucleus) occurred at supersaturation during the condensation of the adatoms on the substrate. Supersaturation is defined by the ratio between the pressure of the arriving atoms and the equilibrium vapor pressure of the film atoms at T_s [102]. At low T_s (200 °C ≤ T_s ≤ 250°C), supersaturation was fast, which reduced not only the critical size of the nucleus but also the magnitude of the nucleation energy barrier, and resulted in the growth of numerous, small RGs. However, at high T_s (300 °C ≤ T_s ≤ 350°C), a reduction in supersaturation rates increased the critical size of the nucleus and the nucleation barrier. Consequently, large nuclei can create isolate islands on the substrates, which then grow and coalesce because of surface diffusion, grain-boundary migration, and possible re-crystallization, driven by the minimum of the interface and surface energy [102–104]. Thus, HPs with c-axis-preferred orientation or large flakes were formed at high T_s (≥300 °C). The formation of HP could be associated with the anisotropic bonding configuration of Bi_2Se_3, leading to that the crystal growth rate along the basal planes is much greater than that along c-axis. Besides, the crystalline facets tend to develop on the low-index planes to minimize the surface energy during growing [105,106]. Thus, the diffusion of atoms at high T_s and the natural layered structure of Bi_2Se_3

results in the assembly of the layered structures for the films deposited at $T_s \geq 300^oC$, which are also observed in the Bi_2Te_3 films deposited at T_s = 350 °C and P = 1.0 Pa, using radio-frequency magnetron sputtering [29].

At high *P*, the ablated plume is confined tightly in the forward direction, which makes deposition faster, but the mobility of adatoms is limited by the adsorbed helium [107,108] to suppress the lateral growth of crystals. In short, increasing *P* accelerates deposition but slows crystal growth of nuclei. Consequently, columnar structures formed at the highest *P* (173 Pa) because of faster deposition rather than increased crystal growth. In contrast, the disoriented and large flakes formed at the lowest *P* of 0.7 Pa because of the high crystal growth rate and the plume expansion effect in which Bi and Se can spread over a large area of the substrate. Notably, the typical open-boundary features of high *P* can be explained by the shadowing effect, because peaks on the growing surface receive a greater coating flux than valleys do, particularly when the flux has a substantial oblique component, and the adsorbed He atoms likely accumulate in crevices and protect the deposited films from the impact of coating atoms [107,108].

4.3 Deposition temperature- and pressure-dependent compositions of Bi_2Se_3 films

Figure 4.2 shows the *P*- and T_s-dependent compositions of Bi_2Se_3 films. The Se/Bi ratio and the corresponding Se atomic percentage (Se at.%) increased monotonically with increasing *P* from 0.7 to 93 Pa and then decreased slightly at 173 Pa. In addition, both Se/Bi ratio and Se at.% decreased considerably when T_s was elevated. Because the vapor pressure of Se is higher than that of Bi (P_{Se}/P_{Bi} approximately 10^7 at 300 °C, Figure 2.12a [21]), Se re-evaporates from heated substrates considerably faster than Bi. With the loss of volatile Se atoms from films, Bi atoms segregate on the surface and at grain boundaries [99], as confirmed by the pure Bi peaks in the XRD patterns (Figure 4.1a(II)) for all highly Bi-enriched (or Se-deficient) films deposited at 0.7 Pa. These results agree with the Bi segregation and XRD patterns reported in ref. [109]. Noticeably, the remarkable reduction of Se at.% at 350°C is still unclear, probably due to the presence of minor BiSe phase and/or a decrease in Se-sticking coefficient occurred at $T_S > 300$°C, as such phenomenon has been observed in Bi_2Te_3 film (Figure 2.12b) [24].

We next addressed the dependence of film composition on the ambient pressure, P. Bi and Se atoms and ions ejected from the target travel initially at their inherent velocities, and the atoms rebound from the substrate with a certain sputtering yield. At high pressure (≥ 40 Pa), the velocities of Bi and Se atoms equilibrate because of increased collisions with ambient gas atoms, resulting in a spatial confinement of the ablated species [38]. Granular structures are often observed during high-P deposition, suggesting that the vapor species nucleate and grow into particulates before arriving at the substrate under high-pressure [110,111]. The coalescence and growth in later stages assemble these initial particulates and normal nuclei into grains or platelets. Moreover, the high P will reduce the evaporation rates of Bi and Se and shorten the diffusion distance of Bi and Se to keep the rebound atoms close to the substrate. The lateral diffusion of the atoms may also be enhanced by the increase in lateral momentum of the rebounded adatoms after several collisions with the ambient gas. Thus, Bi and Se atoms can easily locate their counterparts to form stoichiometric or slightly Se-rich films.

In contrast, at low pressure (≤ 6.7 Pa), the energetic adatoms generated a larger sputtering yield, which resulted in slower deposition or a thinner film than those under high-pressure growth conditions (Figure 4.4). Moreover, the Bi and Se atoms were spread over a large area because the vertical motion of rebounded particles was higher in regions of lower pressure. Therefore, a lower probability of Bi-Se combination and the higher re-evaporation rate of Se than of Bi together yielded Se-deficient films.

4.4. Deposition temperature- and pressure-dependent electrical and TE properties of Bi_2Se_3 films

Figure 4.6 shows that the carrier concentration (*n*) of *n*-type Bi_2Se_3 films is lowered effectively when *P* is increased (as also shown by increase of Se concentration in Figure 4.5). Carrier concentration, *n* dropped significantly when *P* was increased from ≤ 6.7 Pa to ≥ 40 Pa. Interestingly, Bi antisite (Bi_{Se1}) in Bi_2Se_3 is an amphoteric dopant, acting as a donor when electron chemical potential $\mu_e < 0.119$ eV and as an acceptor when $\mu_e > 0.251$ eV [112]. The *n*-dependent *P* can be attributed to the formation of donor antisite defects, Se_{Bi} (Se occupies Bi site) and the Bi_{Se1} under $\mu_e < 0.119$ eV [112], which are readily formed in low *P* than in high *P*. The minimum value of *n* is between $1.4 – 3.2 \times 10^{19}$ cm^{-3} for films deposited at $T_s \leq 250°C$ and at pressures ≥ 93 Pa. Because the higher vapor pressure of Se renders it more volatile, Bi_2Se_3 is often heavily *n*-type doped at sites of Se vacancy

[22,23]. Se vacancies increased with T_s, and, consequently, led to an increased n, a result that agrees with a previous report on Bi_2Se_3 films grown with $T_s \geq 200$ °C [113].

In contrast to the tendency of n, the absolute value of Seebeck coefficients ($|\alpha|$) monotonically increased with increasing P from 0.7 to 93 Pa, and decreased slightly at 173 Pa. The highest values of $|\alpha|$ were 127.3 ± 4.1, 106.4 ± 3.2, 94.9 ± 2.6, and 70.7 ± 1.4 μV/K for T_s = 200, 250, 300, and 350°C, respectively. The value of $|\alpha|$ was slightly lower at higher T_s, which can be attributed to a higher n (likely caused by an increase in the Fermi energy) and an increased grain (crystallite) size at higher T_s. Potential-barrier scattering may further enhance $|\alpha|$ when the grain size becomes smaller, as observed in the PbTe material [87,114].

The Seebeck coefficient depends on the effective number of charge carriers reaching a cold zone. Most thermal carriers are scattered when the doping concentration (n) increased, which leads to a smaller Seebeck coefficient [115]. The relationship between α and n for metals or degenerate semiconductors (i.e., the parabolic band, energy-independent scattering approximation) can be described by Eq. (1) [4,63]:

$$\alpha = \frac{8\pi^2 k_B^2}{3eh^2} m^* T \left(\frac{\pi}{3n}\right)^{2/3} = \frac{A}{n^{2/3}} \qquad (4.1)$$

Figure 4.7 shows that $|\alpha|$ can be fitted closely with the $A \cdot n^{-2/3}$ relation, using Eq. (4.1). The fitting coefficient (A) was 70 % higher than the expected value in Eq. (6) for T = 300 K, and $m^* \approx 0.14 m_o$, applied for $n = 7.2 \times 10^{18}$ cm^{-3} [116]. The discrepancy arises from the unknown value of m^* and the exclusion of the scattering parameter $R\left(= d \ln \ell_s / d \ln E\right)_{E=E_F}$ in the fitting, which determines the energy dependence of the carriers' mean free path (ℓ_s) [63]. To achieve an improved α approximation, as demonstrated for the Bi-Sb-Te nanocrystalline thin film [30], the fitting of our polycrystalline films should include the scattering parameter associated with processes such as acoustic phonon scattering, neutral-ionized impurity scattering, and grain boundary scattering.

The inset in Figure 4.7 shows the carrier mobility μ of the Bi_2Se_3 films grown at various pressures and T_s. The mobility ranged from 7.2 ± 0.2 to $98.4 \pm 0.5 cm^2/Vs$ and depended on both pressure and T_s. For a specific T_s, maximum μ was reached at different deposition pressures that correlated strongly with low values of the FWHM in Figure 4.3 or a low doping concentration (small *n)* (Figure 4.6). A larger *n* (higher doping concentration) coincides in most cases with a higher density of defective scattering centers (ionized impurities), which impedes carrier mobility. The value of μ increased with increasing T_s because defects and grain-boundary scattering from larger grains were diminished. Noticeably, all Bi_2Se_3 films deposited at high pressure (173 Pa) showed lower mobility, which can be attributed to the columnar and voided structures that limit the in-plane transport of carriers in these films.

Figure 4.8 shows the electrical conductivity ($\sigma = n\mu e$) of Bi_2Se_3 films deposited at various T_s and P. The value of σ decreased with increasing P because of the substantial lowering of *n*, whereas σ increased with increasing T_s because the values of both *n* and μ became higher. The temperature-dependent, in-plane electrical conductivities ($\sigma(T)$ in 2–300 K) for the Bi_2Se_3 films deposited at 300°C and at pressures of 0.7, 40, 93, and 173 Pa are shown in the inset of Figure 4.8. Weakly metallic conductivities were observed down to 20 K, which is common in semiconductors with a high carrier concentration and a narrow bandgap (approximately 10^{19} cm^{-3}, $E_g \approx 0.3$ eV in this study). Below 20 K, the electrical conductivities became nearly temperature-independent, as expected in the impurity-scattering region. Both PPMS and Hall measurements showed consistent results for conductivities at room temperature, which varied from 385 Scm^{-1} (or 2.60 mΩcm) to 1400 Scm^{-1} (or 0.71 mΩcm). Furthermore, the electrical conductivities increased to 564 Scm^{-1} (1.77 mΩcm) and 2078 Scm^{-1} (0.48 mΩcm) at 10 K, which are comparable to the 0.3–1.5 mΩcm at 10 K reported for Bi_2Se_3 single crystals [23].

Figure 4.9 illustrates the contour plot of the PF (= $\alpha^2\sigma$) as a function of P and T_s. The PF of Bi_2Se_3 films increased with increasing T_s from 200 to 300 °C because σ became considerably larger but the Seebeck coefficient diminished only slightly. However, for films deposited at 350°C, PF was lowered primarily because of the reduction in α and not the increase of σ. Furthermore, the PF of Bi_2Se_3 films grown at intermediate pressure was typically higher than the PF of films grown at a low or high pressure, because the growth of films at intermediate pressure yields an optimal value of $\alpha^2\sigma$ (= 5.54 ± 0.34 $\mu Wcm^{-1}K^{-2}$ at T_s = 300 °C and P = 40 Pa) associated with layered-HPs films.

The optimal PF value, 5.54 $\mu Wcm^{-1}K^{-2}$, obtained in this study is much higher than those reported previously for $Bi_2Se_3$with the hexagonal-flake structure (PF ≈ 0.28 $\mu Wcm^{-1}K^{-2}$) [14] or for the nanoflake structure (PF ≈ 0.97$\mu Wcm^{-1}K^{-2}$) [15]. Nevertheless, our result is comparable to the PF ≈ 5.8 $\mu Wcm^{-1}K^{-2}$ of Bi_2Se_3 films grown by metal organic-chemical vapor deposition [35], but remains approximately 3 times lower than the room-temperature PF of Bi_2Se_3 single crystals [23].

Table 4.1 summarizes the transport properties (at room temperature) and compositions of selected Bi_2Se_3 films of distinct morphologies grown in this study, and compares these properties and compositions with Bi_2Te_3 films of similar morphologies developed by Chang and Chen [39], using PLD and Deng et al. [29], using radio-frequency magnetron sputtering. For a given microstructure, our deposition conditions are typically lower in T_s and higher in P, which helps suppress n. The Bi_2Se_3 films grown in this study and the Bi_2Te_3 films in ref. [39] share stoichiometric or slightly Se-rich compositions, lower n ($\sim 10^{19}$), and comparable values of $|\alpha|$ (approximately 75–98 $\mu Wcm^{-1}K^{-2}$). The Bi_2Te_3 films in Ref. [29] were deposited at a low P (1 Pa) and a high T_s (300 or 350 °C) and exhibited Te-deficiency, an extremely high n (approximately 10^{21}), and excellent conductivities, but a slightly lower $|\alpha|$, which may have generated the high PF values measured for their films.

4.5 Summary

Effects of helium ambient pressures (0.7 – 173 Pa) and substrate temperatures (200 – 350 °C) on the structures – morphologies, compositions, and TE properties of polycrystalline Bi_2Se_3 films were studied. The films grown at T_s = 300 °C and at P = 40 Pa, and containing highly c-axis-oriented and layered hexagonal platelets, possessed the highest PF: $5.54 \pm 0.34\ \mu Wcm^{-1}K^{-2}$, where $|\alpha| = 75.8 \pm 2.3\ \mu V/K$ and $\sigma = 963.8 \pm 0.4$ S/cm. Furthermore, the mechanism of grown different morphologies of the Bi_2Se_3 films was well described. Moreover, a phase diagram of power factor as a function of deposition parameters was revealed.

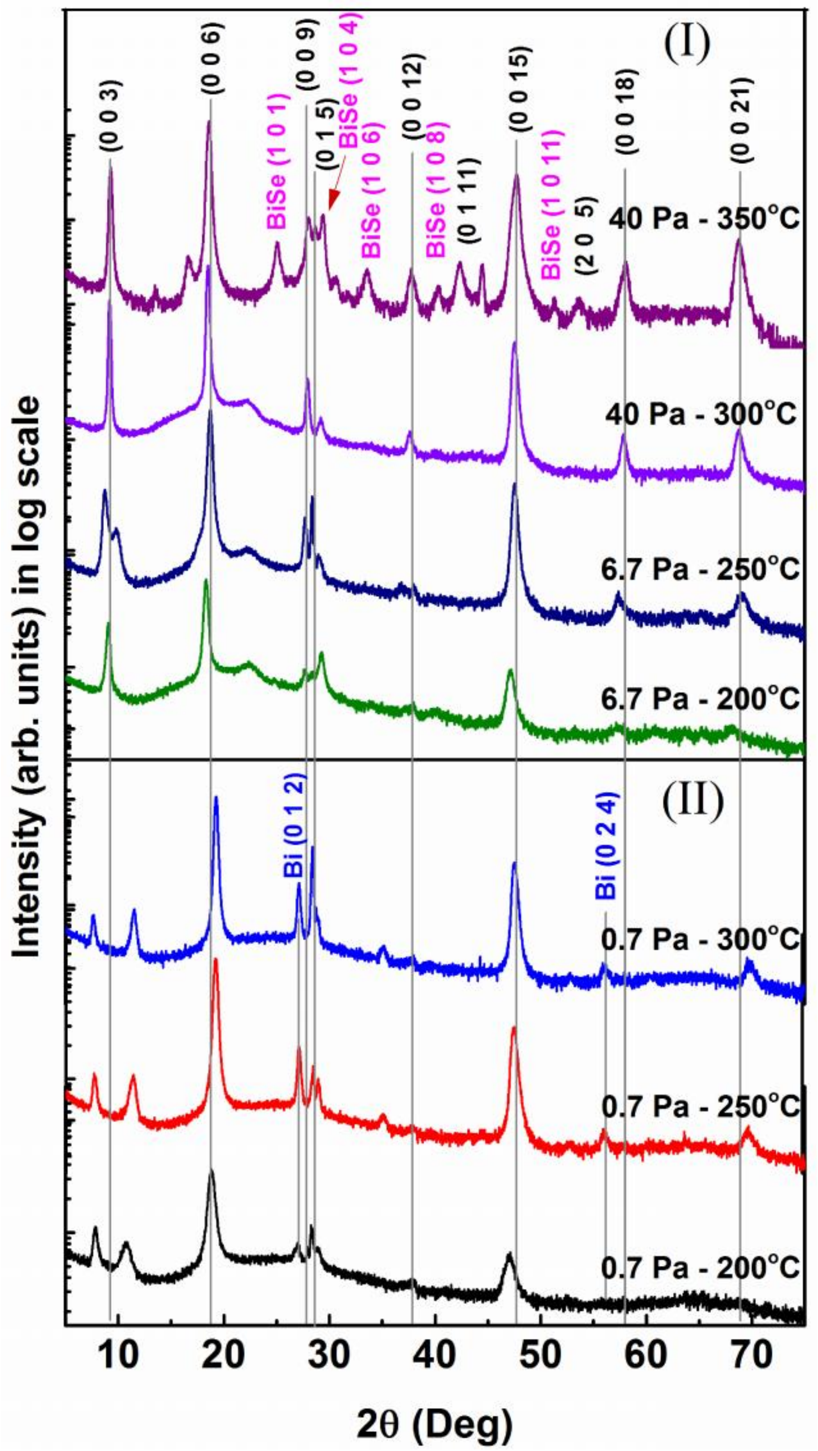

Figure 4.1 (a) X-ray diffraction patterns of Bi_2Se_3 films deposited under: (I) 6.7 or 40 Pa, and T_s of 200 – 350 °C for the best crystallinity films, and (II) 0.7 Pa (the lowest pressure in this study) and T_s of 200, 250, 300 °C.

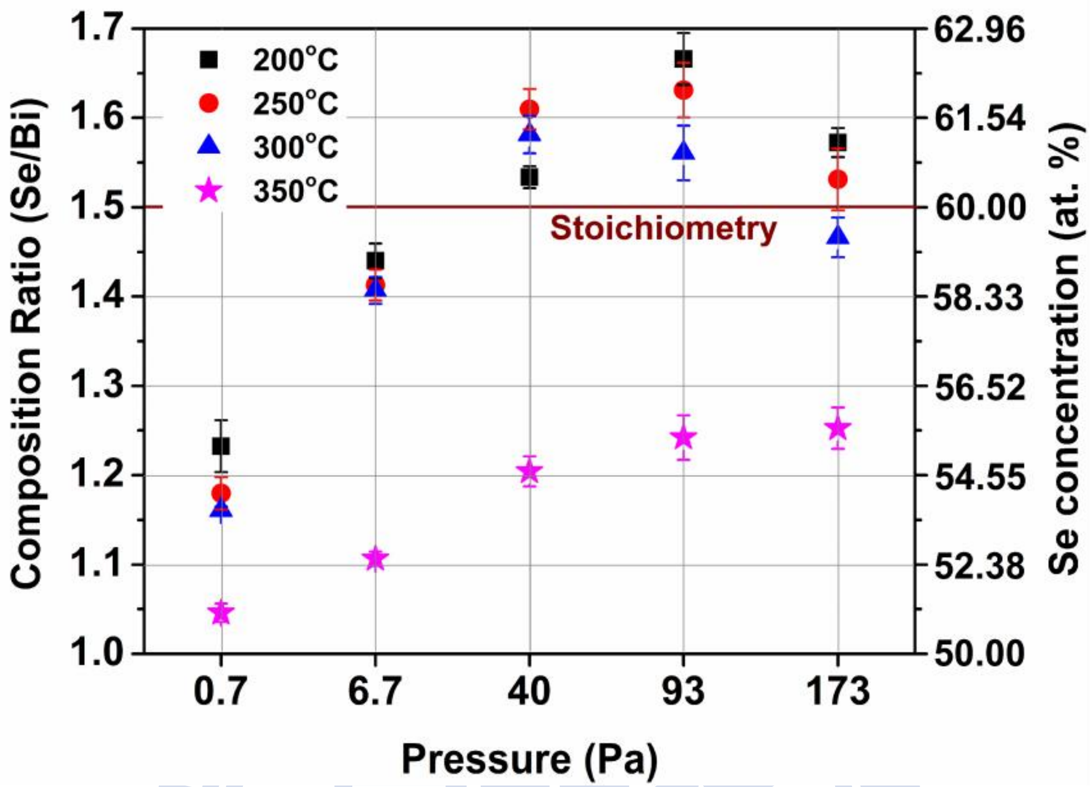

Figure 4.2 Background-pressure-dependent compositions, Se/Bi ratio and Se (at. %), of the Bi_2Se_3 films deposited at various T_s ranging from 200 to 350 °C .

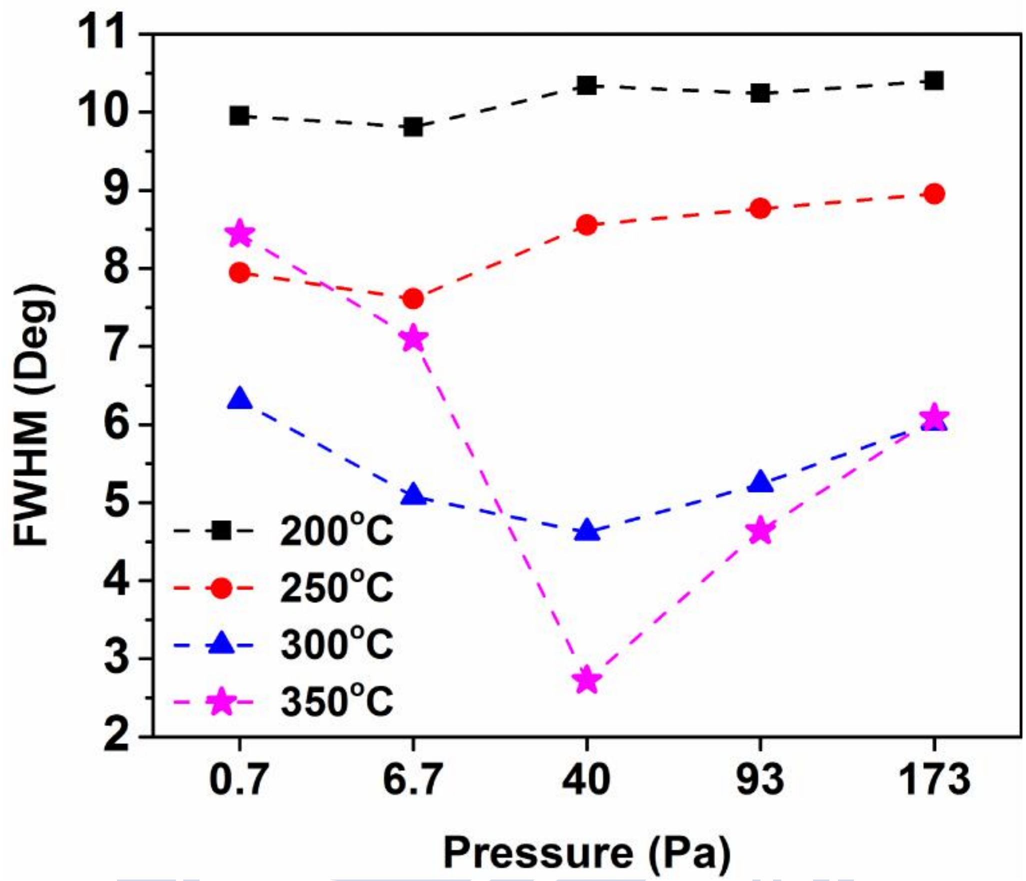

Figure 4.3 FWHM vs. pressure of the rocking curve (006) peaks for Bi_2Se_3 films grown at 200, 250, 300, and 350 °C.

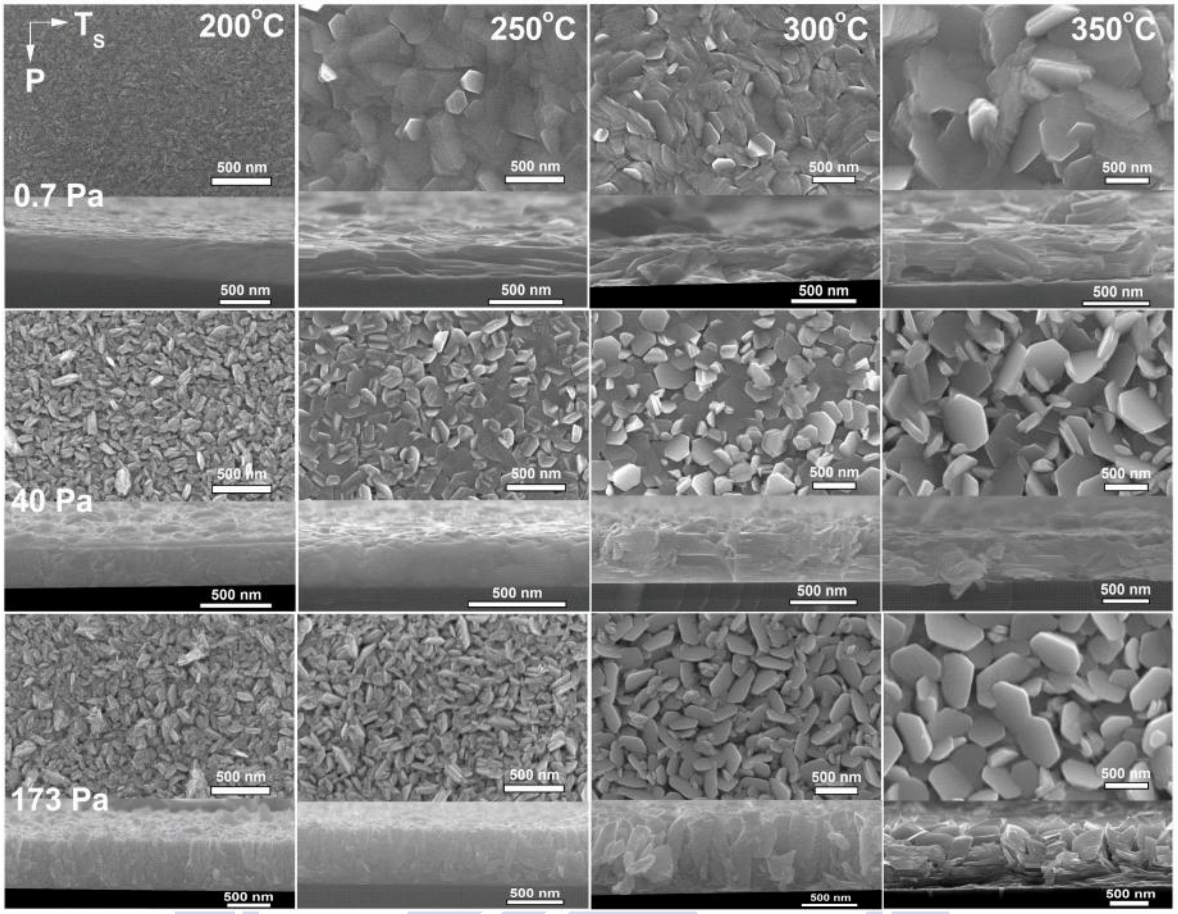

Figure 4.4 Cross-section and top view SEM images of the Bi_2Se_3 films deposited at 0.7, 40, and 173 Pa (top-to-bottom), and at 200, 250, 300, 350 °C (left-to-right).

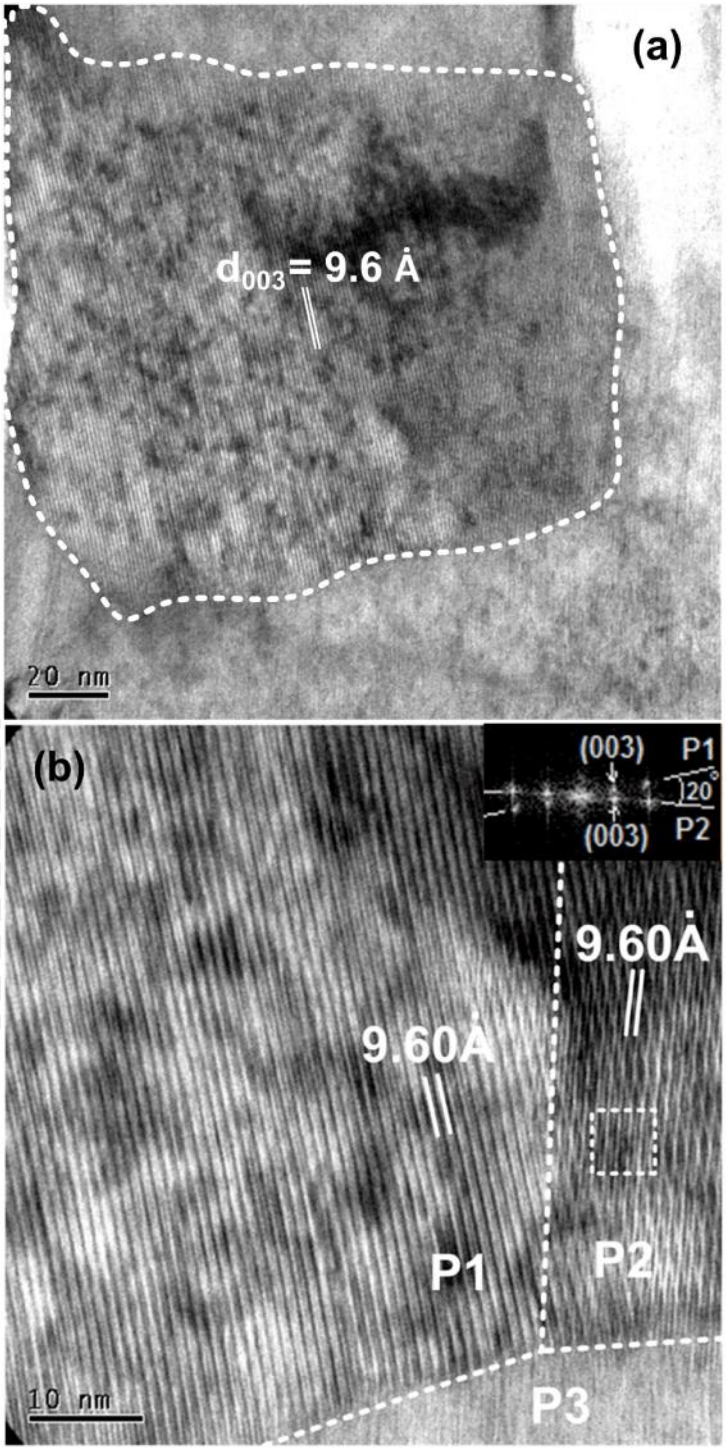

Figure 4.5 A low magnification TEM image (a) and an HR-TEM cross-sectional image (b) of an optimized Bi_2Se_3 film deposited at 40 Pa and 300 °C. The inset shows the FFT patterns of the dash square area in the TEM image.

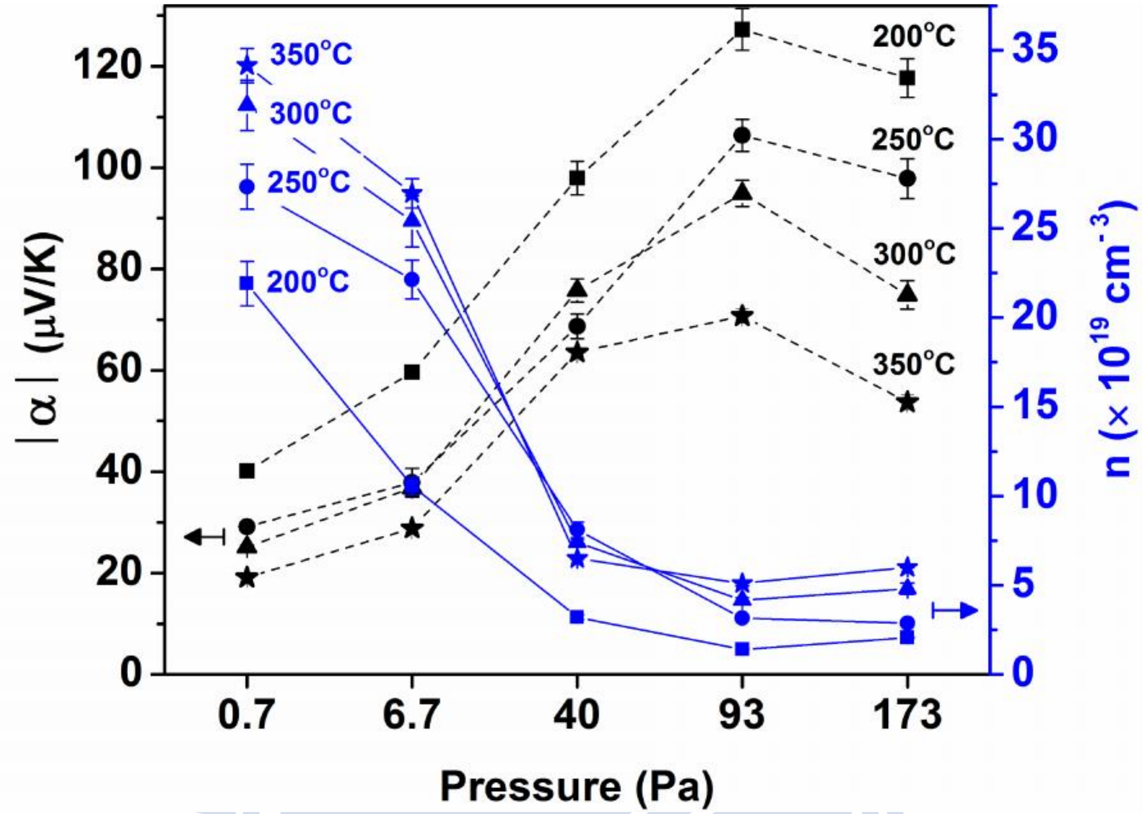

Figure 4.6 Pressure-dependent carrier concentrations (n) and absolute Seebeck coefficients ($|\alpha|$) of the Bi_2Se_3 films.

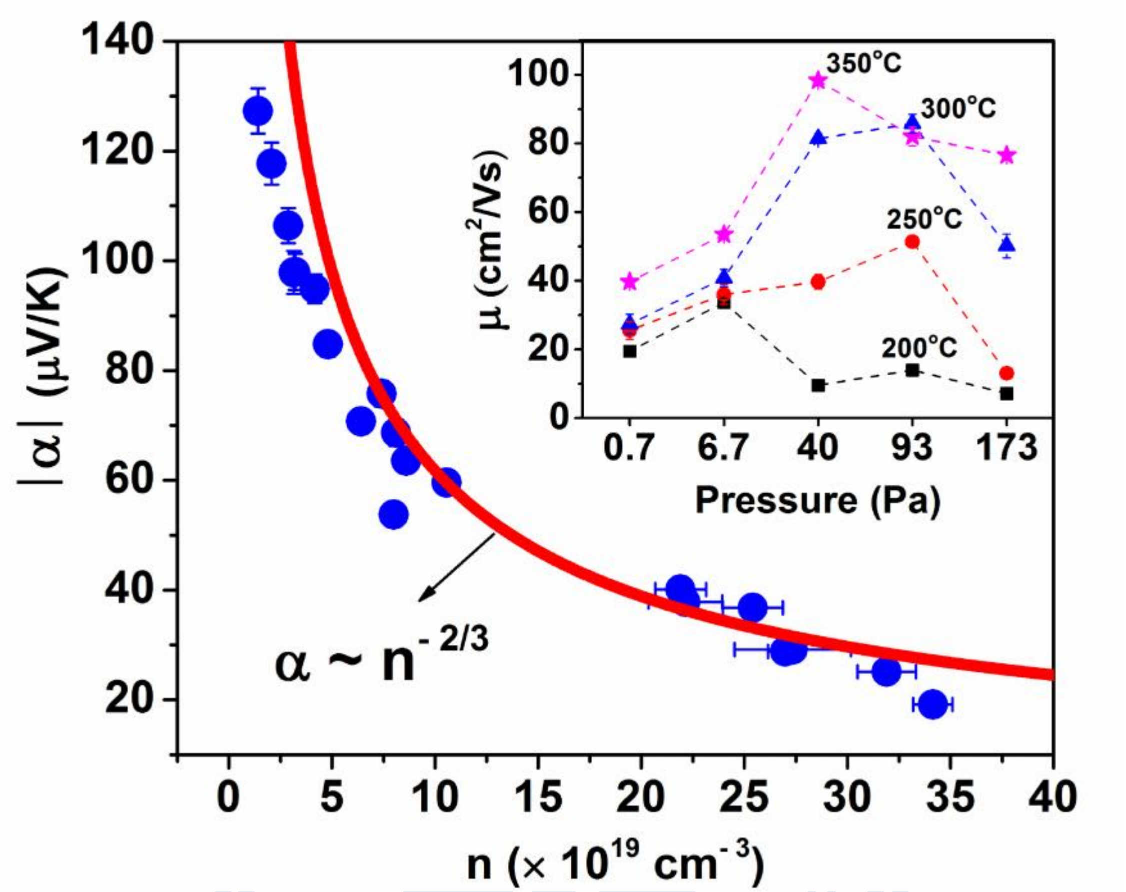

Figure 4.7 The fitting of $|\alpha|$ and n based on $|\alpha| \sim n^{-2/3}$ and the pressure-dependent carrier mobility (μ, inset).

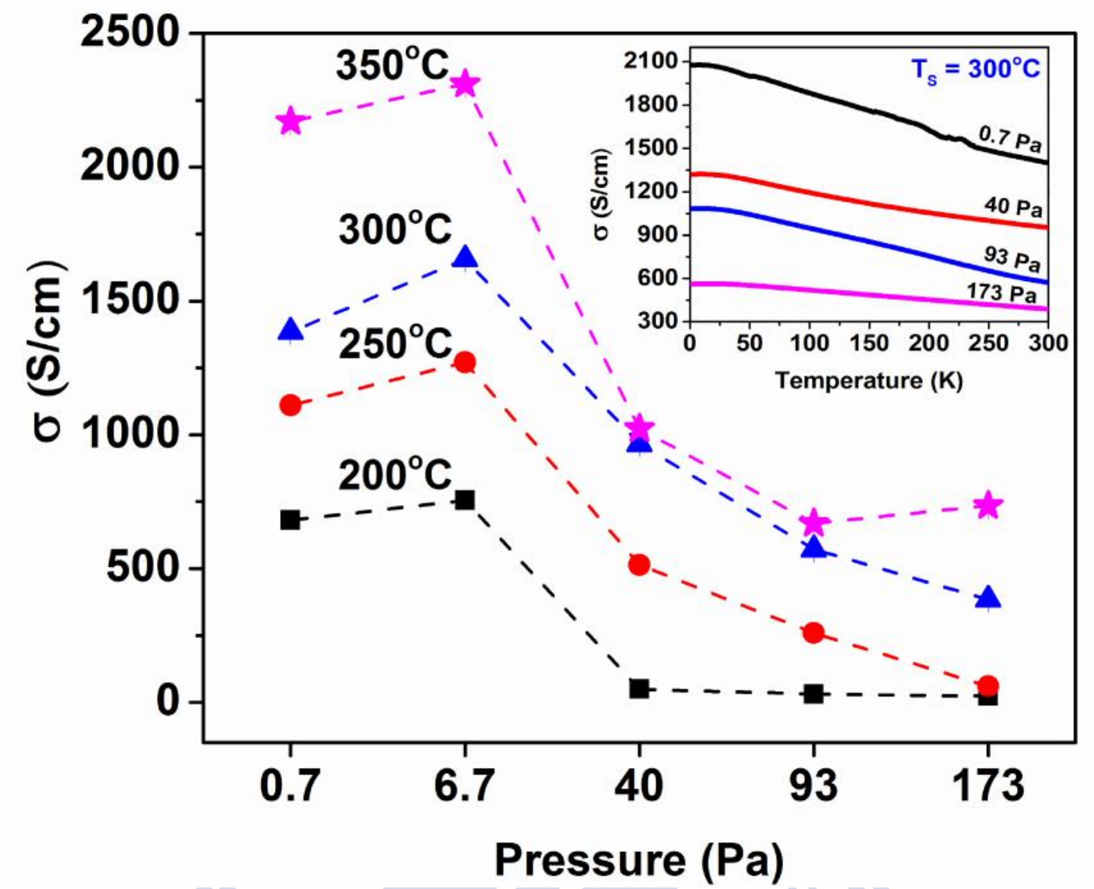

Figure 4.8 Pressure-dependent electrical conductivities (*σ*) of the Bi_2Se_3 films deposited at various T_s from 200 to 350 °C and temperature-dependent conductivities (σ(T) in 2 – 300 K, inset) for the films grown at 300 ^{o}C and at various pressures of 0.7, 40, 93, 173 Pa.

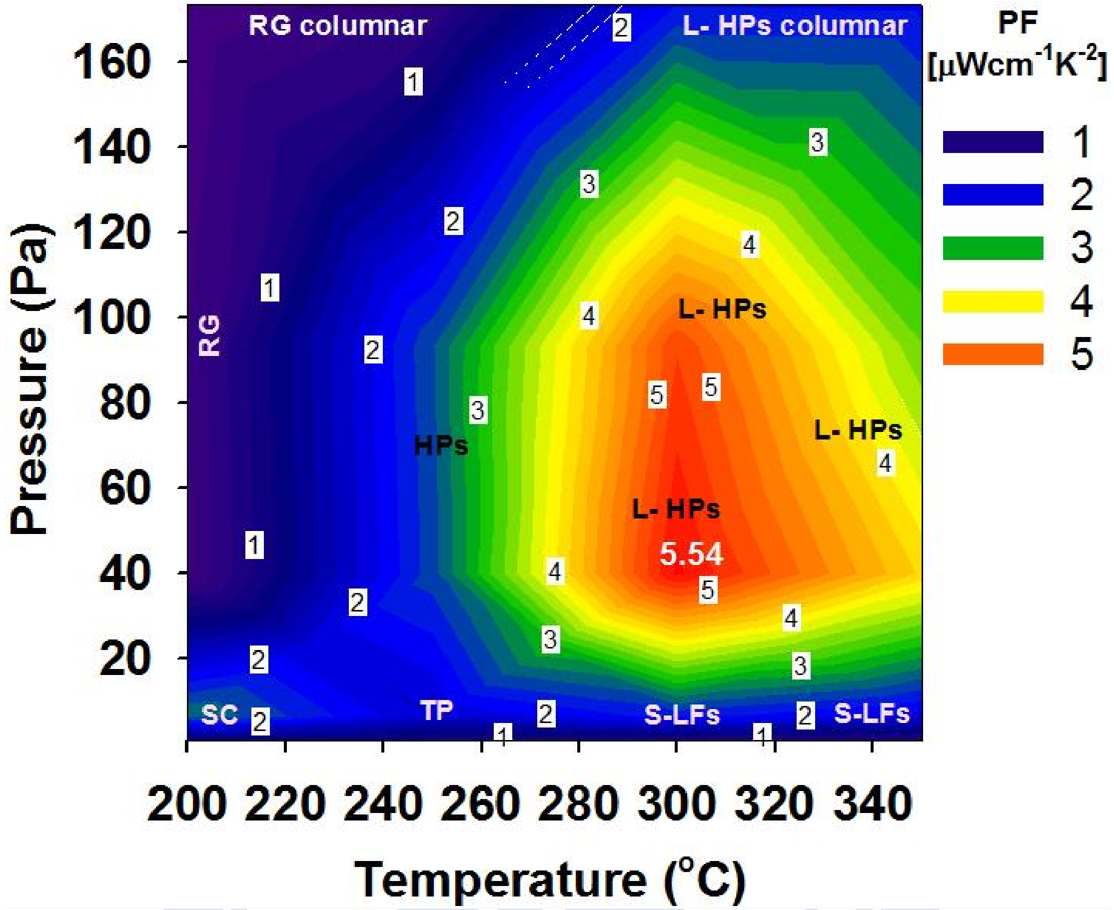

Figure 4.9 Contour plot of the film's power factor (PF = $\alpha^2\sigma$) as a function of background pressure and T_s. The morphology abbreviations: SC, smooth and compact; RG, rice grain; TP, triangular-polygonal; S-LFs, super-layered flakes; L-HPs, layered-hexagonal platelets.

Table 4.1 The transport properties (at room temperature) and compositions of some selected Bi_2Se_3 films with different morphologies in this study and the similar Bi_2Te_3 films deposited by PLD [39] and RF sputtering [29].

Morphology	**Deposition conditions**		***n*** **($10^{19}cm^{-3}$)**	**μ** **(cm^2/Vs)**	**σ** **(S/cm)**	**α** **(μV/K)**	**PF** **($\mu W/cmK^2$)**	**Se/Bi** **At. ratio**	**Ref.**
Rice grains (RG)	200°C	40 Pa	3.2 ±0.2	9.6 ± 0.4	49.2 ± 0.2	-98 ± 3.4	0.46 ± 0.03	60.5/39.5	This work
Nanoparticles	300°C	20 Pa	9.7	14.8	230	-91	1.90	60/40	Chang and Chen [39]
Nanoparticles	300°C	1.0 Pa	105	8.3	1390	-60	5.0	56.9/43.1	Deng et al. [29]
Layered HPs	300°C	40 Pa	7.4 ± 0.3	81.4 ± 1.4	963.8± 0.4	-75.8 ± 2.3	5.54 ± 0.34	61.3/38.7	This work
Layered Structure	350°C	1.0 Pa	95	12.1	1840	-70	8.8	56.6/43.4	Deng et al. [29]
Layered-HPs columnar	300°C	173 Pa	4.8 ± 0.3	50.2 ± 3.4	385.5± 0.3	-74.9 ± 2.8	2.16 ± 0.16	59.5/39.5	This work
Nanorods	250°C	0.9 Pa	9.1	2.0	29	-81	0.19	62/38	Chang and Chen [39]
Columnar Structure	350°C	1.0 Pa	246	7.5	2990	-46	6.4	57.2/42.8	Deng et al. [29]

Chapter 5 Thermoelectric properties of nanostructured bismuth-telluride thin films

5.1 The morphology of nanostructured Bi_2Te_3 films

Figure 5.1 presents the cross-section and top-view SEM images of Bi_2Te_3 thin films grown at T_s ranging from 30 to 380 °C at P_{Ar} = 80 Pa. Under these conditions, films of six well-defined morphologies featuring distinct grain sizes, shapes, and stacking characteristics were successfully prepared. Figure 5.2 presents the grain-size distribution and the most probable size (MS) of these films, which were determined using SEM statistical analysis. First, at room temperature (30 °C), 0D columnar nanoparticles (CNPs) were grown, which exhibited the smallest MS (57 nm) and a columnar structure that was approximately 50 nm wide and 400 nm high. Second, at 120 °C, columnar nanoflowers (CNFs) were formed as a result of the stacking of 2D platelets (MS = 73 nm), which generated flower-like structures featuring columns that were approximately 75 nm wide and 500 nm high. Third, at 220 °C, nanodiscs (NDs) were formed that comprised numerous disc-like crystals, whose MS was 287 nm in diameter and 24.5 nm in thickness; the disc thickness was determined by performing 2D fast Fourier transform (FFT, the inset in Figure 5.1c) of the dashed-square area indicating a set of discs (Figure 5.1c). Fourth, at 300°C, a layered compact polycrystalline (LCP) film was prepared that exhibited an MS of 477 nm. Intriguingly, this film was formed by compactly stacking of the 3D layered nanoblocks, but it exhibited a relatively rough surface. Fifth, at 340°C, a layered-triangular-platelet (LTP) structure was prepared that exhibited the largest MS (846 nm, with a layer thickness of 53 nm) and the broadest grain-size distribution (reaching the micron size) (Figures 5.1e and 5.2). Finally, the films deposited at 380 °C displayed a polyhedral (PH) structure that was composed of 3D triangular and polygonal crystals (MS of 785 nm) and exhibited a diminished density because of the presence of microvoids between crystals. The MS and the width of the distribution curves increased monotonically with increasing T_s from RT to 340 °C and then decreased slightly at 380 °C, as shown in Figure 5.2 and the inset of Figure 5.2.

5.2 Growth mechanisms of Bi_2Te_3 nanostructures

The T_s used can affect the nucleation and growth of films. At low a T_s, the rate of supersaturation is high, which reduces not only the critical size of the nuclei but also the magnitude of the nucleation energy barrier, and thus numerous, small nanoparticles grew at 30 °C and nanoflowers grew at 120 °C [20]. Moreover, the growth mechanism of the columnar structures (Figures 5.1a and 5.1b) can be attributed to the combined effects of a high deposition rate and a low crystal growth rate: the high P_{Ar} of 80 Pa tightly confines the ablated plume along the direction of the substrate to increase the deposition rate [38], whereas the potentially adsorbed argon limits the mobility of adatoms to suppress the lateral growth of the crystals at low T_s (≤ 120 °C) [107,108]. By contrast, the deposition is faster on the top of islands than in the valleys between the islands with an oblique incident flux (the so-called shadowing effect) [107,117], which generates the separated or voided inter-grain boundaries of columnar structures. The columnar structures present in the Bi_2Te_3 films grown here were similar to those in Bi_2Se_3 films grown at comparatively high temperatures and pressures (200 – 250 °C, 173 Pa helium) [20].

At a high T_s (≥ 220 °C), however, a reduction in the supersaturation rate increases the critical size of the nuclei and the nucleation barrier. Consequently, the large nuclei can further create isolated islands and 3D crystal structures on the substrates to minimize the surface energy and interface energy [102,103] by means of surface diffusion, grain-boundary migration, and possible recrystallization. Conversely, the LTP structure might be formed because of the anisotropic bonding configuration of Bi_2Te_3 and the inevitable deviations from a uniform growth environment [105,118,119]. Moreover, both the diffusion of atoms at high T_s (≥ 220 °C) and the naturally layered crystal structure of Bi_2Te_3 result in the formation of layered ND, LCP, and LTP structures [105].

5.3 Structural analysis of nanostructured Bi_2Te_3 films

Figure 5.3a shows the normalized XRD patterns of the Bi_2Te_3 target and films. The polycrystalline rhombohedral Bi_2Te_3 phase (space group $D_{3d}^{5}-R\overline{3}m$) with (015)-dominant orientation of the target can be confirmed (JCPDS 82-0358). The films grown at $T_s \leq 340$ °C exhibited the Bi_2Te_3 phase but no other detectable phases. However, when T_s was increased to 380 °C, the PH film possessed Bi_4Te_5 phase (JCPDS 22-0115), which was associated with a composition of approximately 51.5 at.% Te (Figure 5.4). Moreover, like the target, the dominant orientation of the CNP (30 °C) and CNF (120 °C) structures was (015). Typically, Bi_2Te_3 (015) is the preferred orientation of 1D structures [29,39,120] because this orientation supports not only stoichiometric growth but also regular structures that feature a bonding sequence of $\cdots Te^{(1)}–Bi–Te^{(2)}–Bi–Te^{(1)}\cdots$[97]. Because the adatom mobility increased at T_s =

220–340 °C, the films featuring ND, LCP, and LTP structures exhibited the highly preferred crystal orientation of {00l}, which possesses the lowest surface energy as a result of the weak $Te^{(1)}\cdots Te^{(1)}$ bond [97].

The crystallinity and grain orientation of the films were determined by measuring X-ray rocking curves. As shown in Figure 5.3a, the full width at half maximum (FWHM) of the (006) peak in the Bi_2Te_3 phase and the (0011) peak in the Bi_4Te_5 phase dropped substantially, from 5.87° in the case of CNFs (at 120 °C) to 0.74° in NDs (at 220 °C), indicating that NDs feature superior crystallinity and grain orientation compared with CNFs. Because of the presence of disoriented grains and a rough surface, the FWHMs of the LCP (at 300 °C) and PH (at 380 °C) structures increased slightly, to 1.82° and 1.49° respectively. By contrast, the LTP film exhibited a small FWHM, 1.05°, which can be attributed to the large (micrometer-scale) grain size, flat surface, and layered structure of the film, reducing the disorientation of crystallites.

HRTEM images performed on the low μ CNP film and the highest μ ND film are shown in Figures 5.3b and 5.3c, respectively. Clearly, Figure 5.3b presents some nanoparticles (nanocrystals) with sizes > 10 nm. Moreover, the lattice spacing of nanoparticles is approximately 0.323 nm, which corresponds to the value of (015) interplanar distance of the Bi_2Te_3 crystal. The white lines in Figure 5.3b indicate the orientations of (015) planes. Intriguingly, although the overall (015)-orientation is randomly, it possesses some local preferred orientations as shown by the parallel white lines amongst some close nanocrystals. For the ND (220 °C) film, the lower inset in Figure 5.3c shows the film with uniform thickness of approximately 295 nm, and the SiO_2 layer with thickness of 300 nm. Furthermore, an HRTEM image (Figure 5.3c) obtained from the solid square area in the inset exhibits the projected periods of 0.508 nm along the c-axis correspond to the lattice spacing of the (006) planes. Thus, the c-axis lattice constant of the film is 30.48 Å of Bi_2Te_3, which agrees closely with the value (30.44 Å) presented in JCPDS 82-0358. The other examined areas also present similar results. Consequently, this TEM results further demonstrated the highly (00l)-orientated and crystallized structures of the ND, LCP, LTP films that should facilitate the transport of charge carriers.

5.4 Composition and transport analysis of nanostructured Bi_2Te_3 films

The P_{Ar} of 80 Pa was determined to be a suitable background pressure because it allows stoichiometric films to be grown even when the T_s is high (up to 340 °C). We note that low pressures typically increased Te deficiency and elevated n, whereas high pressures commonly generated macroscopic droplets on film surfaces. These effects of pressure agree with previous studies on Bi_2Se_3 films [20] and with the results described elsewhere [121]. In Figure 5.4, the black squares indicate the T_s-dependent Te at.% of the six films featuring distinct nanostructures that were deposited at 80-Pa argon. The films clearly exhibited Te enrichment, stoichiometry, and substantial Te deficiency at $T_s \leq 120$ °C, 220 °C $\leq T_s \leq 340$ °C, and $T_s = 380$ °C, respectively. Because the vapor pressure of Te is higher than that of Bi ($P_v^{Te} / P_v^{Bi} \approx 10^5$ at 300 °C, see Figure 2.12a [21]), Te reevaporates from heated substrates much faster than Bi does [19,21]. This also occurred in the case of Bi_2Se_3 films [122], in which the film composition varied from being Se-rich to stoichiometric to Se-deficient with increasing T_s. The Te at.% dropped sharply to approximately 51.5% at 380 °C (Figure 5.4), which might be explained by a substantial increase in the Te reevaporation rate and a lowering of the Te sticking coefficient (see Figure 2.12b) [24].

The variation in the n-type carrier concentration (n) and mobility (μ) as a function of T_s and the nanostructures is shown in Figure 5.4. The n values of Te-rich films were 6.9×10^{19} cm^{-3} (CNPs, at 30 °C) and 9.3×10^{19} cm^{-3} (CNFs, at 120 °C), but decreased considerably to range from 2.9×10^{19} to 4.9×10^{19} cm^{-3} in the case of stoichiometric ND, LCP, and LTP films deposited at 220, 300, and 340 °C, respectively. However, in the highly Te-deficient PH–Bi_4Te_5 films deposited at 380 °C, n increased dramatically, reaching approximately 1.06×10^{21} cm^{-3}. This agreed well with the result in ref. [17] that the n increased dramatically from 4.9×10^{19} to 5.0×10^{20} cm^{-3} with increasing Bi content from 40 at.% (stoichiometry) to 45 at.% (Bi_4Te_5 phase). Therefore, the stoichiometry plays a vital role in reducing the n of the films.

The μ value was inversely proportional to the FWHM and the carrier concentration n (Figures 5.3a and 5.4). The CNP and CNF films grown at a low T_s ($\leq$ 120 °C) had a low μ, < 10 cm^2/Vs, because of the strong grain-boundary scattering resulting from the columnar structures with small grains (MS of 57 or 73 nm) and the defective scattering centers (ionized impurities). However, in the ND, LCP, and LTP films grown at 220–340 °C, μ increased substantially and ranged from 83.9 to 122.3 cm^2/Vs because of the suppression of those scattering mechanisms, as suggested by the low FWHMs and n results. In addition, the highly (00l)-oriented layered structures with in-plane large crystallites provides a preferential way for electron transport along the ab-plane and thus promotes the carrier mobility. Recently, Y. Deng et al. [28]

observed that the μ of the highly (00l)-oriented layered Bi_2Te_3 film was approximately 5 times higher than that of the ordinary (015)-oriented film. Despite featuring a large grain size (MS = 785 nm), the μ in the Bi_4Te_5 films displaying the PH structure was small (2.5 cm^2/Vs) because of an extremely high carrier concentration ($n = 1.06 \times 10^{21}$ cm^{-3}), the difference in phase, and the ordinary 3D–voided structure.

A. Li Bassi et al. [17] reported that the μ of Bi-Te films obtained a high value of approximately 100 cm^2/Vs only for the stoichiometric Bi_2Te_3 film, meanwhile it remained low values of 10–30 cm^2/Vs for the other non-stoichiometric Bi-Te films and phases. This result suggests that the stoichiometry plays a certain contribution to the substantially enhanced μ of the films grown at 220–340 °C. Since the high-μ preferred structures and the stoichiometry are obtained concurrently in these films, it is hard to fully extract the individual contribution of each factor for the enhanced μ. Nevertheless, under a similar deviation within 2.0 at.% from stoichiometry, the μ of the 220–340°C films exhibit a small difference (below 31.5%, Figure 5.4) compared to 81.2% for the compact films in ref. [17]. This weakly μ-dependence on the stoichiometry suggests that microstructure is the predominant factor contributed to the substantial μ enhancements of the present films.

To explain the evolution of n, the antisite and vacancy defects must be considered. From the XRD (0 0 6) and (0 0 15) peaks, the averaged c-lattice constants of the films were determined using the hexagonal unit cell relation:

$$\frac{1}{d_{hkl}^2}=\frac{4}{3}\left(\frac{h^2+hk+k^2}{a^2}\right)+\frac{\ell^2}{c^2}$$

As shown in the inset in Figure 5.5, the *c*-lattice constant of the CNP and CNF films that were Te-rich is considerably smaller than the standard value of 30.44 Å (JPCDS 82-0358), suggesting the presence of a high density of antisite Te_{Bi} (Te occupying a Bi site, a donor-point defect) because of the smaller atomic radius of Te (1.4 Å) compared with Bi (1.6 Å) [123]. This is to be expected because the strain effect can be neglected for such thick films (thicknesses > 530 nm, Figures 5.1a and 5.1b), and also because Te_{Bi} exhibits the smallest formation energy (approximately 0.5 eV) among point defects such as Bi_{Te} (Bi occupying a Te site) and V_{Te} (Te vacancy) under a Te-rich condition [124,125]. This result suggests that Te_{Bi} is the dominant donor defect that generates the moderate *n* values of the Te-rich films.

The decrease of *n* in the stoichiometric ND, LCP, and LTP films was associated with a reduction in the donor defects Te_{Bi} and V_{Te}, because the *c*-lattice constant was close to the database value (inset in Figure 5.5). Moreover, the T_s of 220–340 °C should be sufficient for atoms to move and drop to the lowest potential-energy sites and thus reduce the numbers of defects. The structure of the Bi_4Te_5 phase can be derived by stacking hexagonal Bi_2 and Bi_2Te_3 blocks, $(Bi_2)_m(Bi_2Te_3)_n$, and (m:n = 1:5), where the –(Bi–Bi)– blocks intercalate in van der Waals gaps between the –($Te^{(1)}$–Bi–$Te^{(2)}$–Bi–$Te^{(1)}$)– blocks [126]. Furthermore, the PH–Bi_4Te_5 film remained substantially Te-deficient (approximately 4.1 at.%) when compared with the Te at.% of the EDS results (51.5) and the ideal value of the Bi_4Te_5 phase (55.6). Therefore, the dramatic increase of *n* in the PH–Bi_4Te_5 film can be attributed to the dominance of V_{Te} under such Te-deficient (or Bi-rich) conditions, which can also leave Bi interstitials in the lattice and thus generate a *c*-lattice constant that is slightly larger than the database value (JCPDS 22-0115).

Figure 5.5 shows the *n*-dependent $|\alpha|$ of the films deposited at various T_s. The stoichiometric ND, LCP, and LTP films featuring a low *n* (2.9–4.9 × 10^{19} cm^{-3}) possessed superior $|\alpha|$ values, ranging from 172.8 to 189.7 μV/K. By contrast, both Te-rich (CNPs and CNFs) and Te-deficient (PHs) films featuring a high *n* possessed substantially lower $|\alpha|$ values, which ranged from 32.6 to 53.6 μV/K (Figure 5-5). This can be described effectively by the relationship $|\alpha| \sim m^* n^{-2/3}$ (Eq. 4.1) in degenerate semiconductors (i.e., the parabolic band, energy-independent scattering approximation [4]), as also shown in Figure 5.5, in which the solid lines are the plots of the formula in Figure 5.5 [4], featuring various effective mass m^* values, ranging from $0.4m_0$ to $1.0m_0$ (where m_0 is the free electron mass). Very recently, H.S. Shin et al. [127] used $m^* = 0.58m_o$ whose value was inferred from ref. [3] to describe well their transport results of the Bi_2Te_3 nanowires with the similar *n* of 4.9 × 10^{19}–1.8 × 10^{20} cm^{-3}. The present m^* values in the range of $0.4m_0 – 1.0m_0$ was comparable or slightly larger than the expected value ($0.58m_0$) because various scattering sources, such as the grain boundary, lattice, and ionized impurity scatterings, are excluded in the approximation.

Figure 5.6 shows the T_s-dependent α, σ, and PF (= $\alpha^2\sigma$) of the films. The σ value gradually increased from 34.5 ± 0.1 to 814.3 ± 1.5 Scm^{-1} when T_s was increased from 30 to 300 °C, and then sharply decreased to 647.3 ± 0.4 Scm^{-1} at 340 °C and 414.0 ± 1.2 Scm^{-1} at 380 °C. The enhanced σ (= 647.3 – 814.3 Scm^{-1}) of the films grown at 220–340 °C originated from the substantially enhanced μ because the *n* exhibited a slight decrease (Figure 5.4). Although the coupled relationship between σ (= $ne\mu$) and $|\alpha|$ (~ $n^{-2/3}$) generally constrains the concurrent enhancement of σ and $|\alpha|$, a reduction of n and a substantial increase of μ in the same optimal range of T_s, 220–340 °C, could lead to high values of both σ and $|\alpha|$. Consequently, the PF of the stoichiometric ND, LCP, and LTP films reached remarkably high values, ranging between 18.2 ± 0.25 and 24.3 ± 0.44 μW/cmK^2, whereas the PF was low (≤ 0.44 μW/cmK^2) in the case of nonstoichiometric films deposited at $T_s \leq 120$ or 380 °C (Figure 5.6).

The composition, transport and TE properties at room temperature of the optimal Bi_2Te_3 films in this study and those in the earlier relevant studies [17,27–29,37,39,89] are summarized in Table 5.1. The optimal PF value (24.3 μWcm^{-1}K^{-2}) of a layered-compact polycrystalline film obtained in this study was considerably higher than those of the Bi_2Te_3 films featuring a nanoparticle structure (PF = 1.9 μWcm^{-1}K^{-2}) [39], a layered structure (PF = 8.8 μWcm^{-1}K^{-2}) [29], a hexagonal structure (PF = 18.4 μWcm^{-1}K^{-2}) [27], and a compact-smooth structure (PF ≈ 21.2 μWcm^{-1}K^{-2}) [17]. However, it was slightly lower than the PF = 27 μWcm^{-1}K^{-2} of a smooth epitaxial Bi_2Te_3 film grown using MBE [37]. Furthermore, the optimal PF of 24.3 μWcm^{-1}K^{-2} was approximately 1.39-, 1.64-, and 2.08-times lower than the PFs ≈ 33.7, 39.9, and 50.6 μWcm^{-1}K^{-2} of a highly (00l)-oriented layered [28], a hexagonal polycrystalline [89], and a layered smooth films [17], respectively. Generally, as illustrated in Table 5.1, a stoichiometric composition is necessary to obtain a reasonably low n (≤ 1.0 × 10^{20} cm^{-3}) which in turn allows obtaining a high $|\alpha|$ value. Moreover, a layered structure is mostly found to be the best morphology for excellent TE properties (Table

5.1). In this study, the structure combining both layered and compact features exhibited the highest PF value amongst our films owning to its high σ up to 814.3 ± 1.5 Scm^{-1}.

The aforementioned results revealed that in this study, Bi_2Te_3 thin films prepared using PLD exhibited high PF values at elevated temperatures, at which the PFs of Bi_2Te_3 and Bi_2Se_3 thin films could be suppressed because of nonstoichiometry and donor-point defects (i.e., vacancies V_{Te} and V_{Se} or antisites Te_{Bi} and Se_{Bi}) [19,20]. In this study, a simple deposition strategy was adopted in which the ambient pressure used (80 Pa) was higher than that typically used in PLD depositions (see Table 5.1), with the goal being to reduce the extent of doping and the T_s (220 °C ≤ T_s ≤ 340 °C) for high-μ preferred structural growth. This approach not only alleviated the doping problem without the requirement of any extra engineering of the targets or engineering during the film growth, but also improved the structural quality of the films and thereby enhanced the charge-carrier mobility and substantially increased PFs. This PLD strategy could potentially be extended to fabricating high-PF thin films on excellent compounds such as $Bi_{2-x}Sb_xTe_3$ and $Bi_2Te_{3-x}Se_x$, promising for applications in TE devices.

5.5 Summary

Several bismuth-telluride films featuring distinct nanostructures were fabricated using PLD at T_s of 30–380 °C and a P_{Ar} of 80 Pa. Nonstoichiometric films grown at either low T_s (≤ 120 °C) or high T_s (= 380 °C) exhibited a low PF, ≤ 0.44 $\mu W/cmK^2$, whereas stoichiometric films grown in the range of 220 °C ≤ T_s ≤ 340 °C exhibited substantial enhancements in PF (between 18.2 ± 0.25 and 24.3 ± 0.44 μWcm^{-1}K^{-2}) that were associated with the highly (00l)-oriented and the compact- and/or layered- large grains morphologies. The PFs ($= \alpha^2\sigma$) were enhanced because of an improvement in carrier mobility (μ = 83.9–122.3 cm^2/Vs) and a lowering of carrier concentration ($n < 5 \times 10^{19}$ cm^{-3}), which respectively enhanced electrical conductivity σ and $|\alpha|$ (obeying the relationship $|\alpha| \sim n^{-2/3}$).

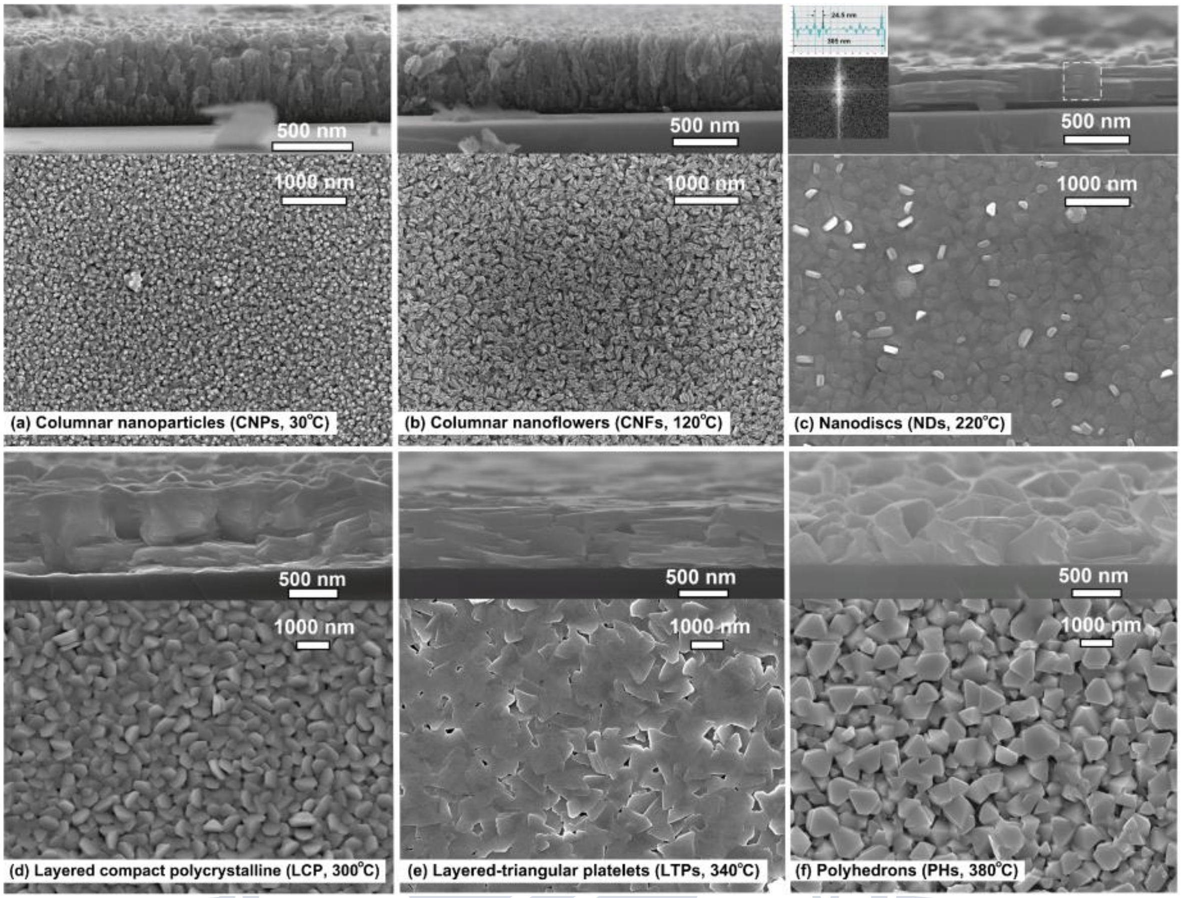

Figure 5.1 Cross-section and top view SEM images of n-type Bi_2Te_3 thin-films with different nanostructures deposited at various substrate temperatures (T_s) from 30 to 380 °C under an argon background pressure (P_{Ar}) of 80 Pa. The inset in panel (c) shows the FFT patterns and distance profile of the dash square area in the SEM cross-section image.

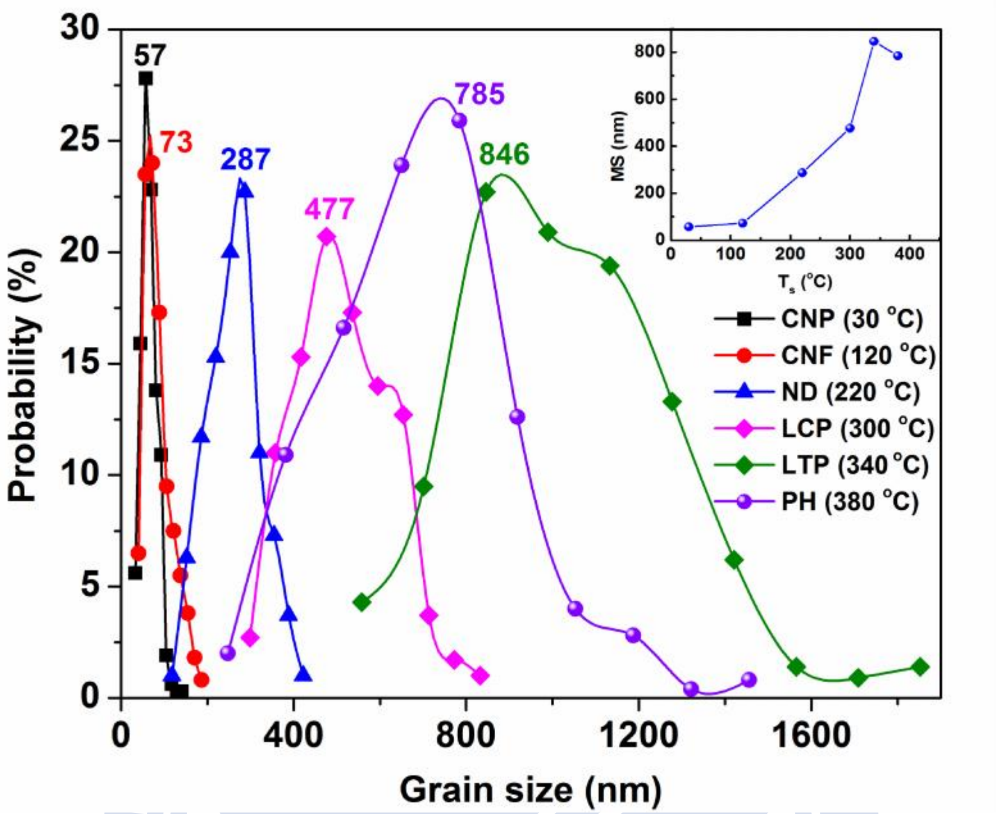

Figure 5.2 Grain size distributions and the most probable size (MS) of the films in Figure 5.1 (a-f), which was statistically analyzed from at least 200 grains of top-view SEM images. The inset shows the T_s-dependent MS of the films.

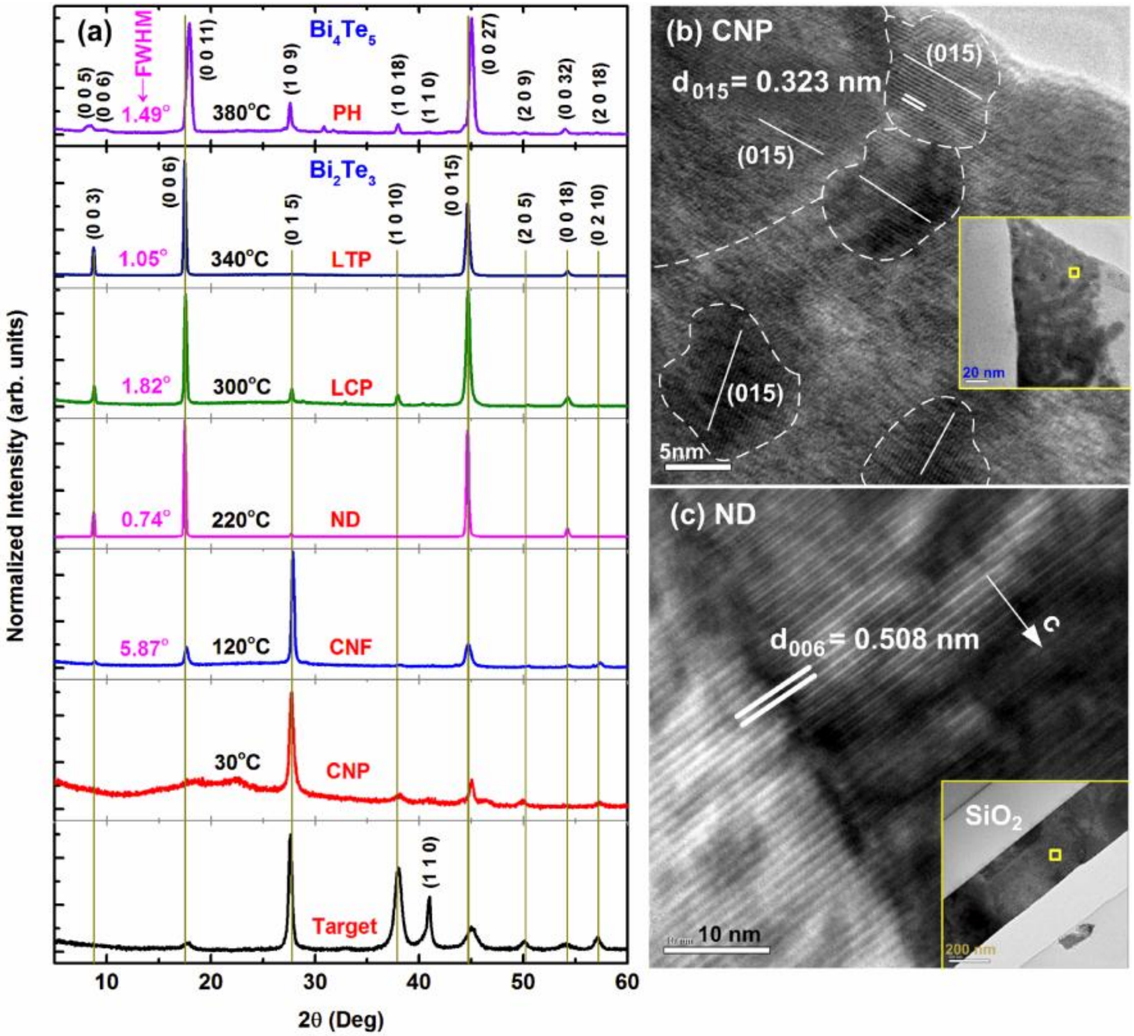

Figure 5.3 (a) The normalized X-ray diffraction patterns of Bi_2Te_3 and Bi_4Te_5 thin films. FWHMs of X-ray rocking curves for (0 0 6) peak in Bi_2Te_3 phase and (0 0 11) peak in Bi_4Te_5 phase. (b) An HRTEM image and a low magnification TEM (inset) of the columnar nanoparticle (30 ^{o}C) film; the white lines indicate the (0 1 5) orientation of the nanograins. (c) An HRTEM and a low magnification TEM (inset) images of the nanodisc (220 ^{o}C) film.

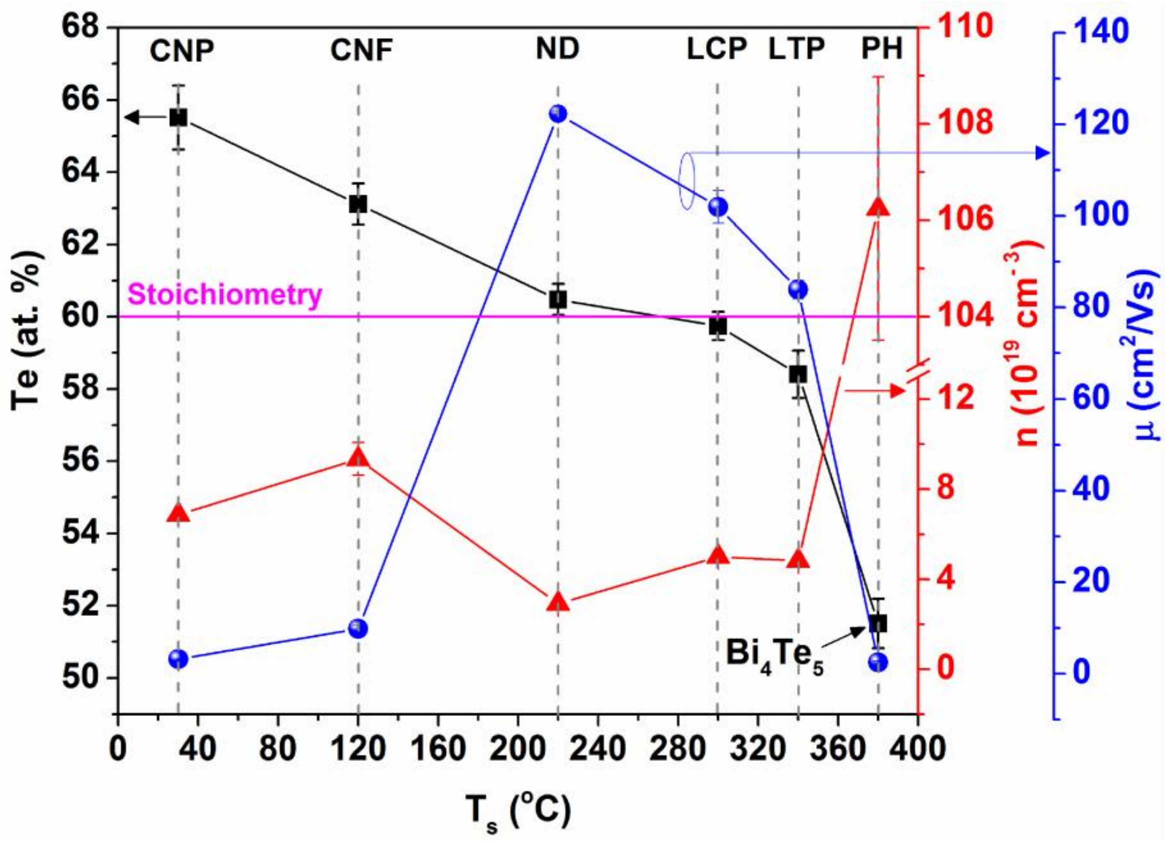

Figure 5.4 T_s-dependent Te at.% (black squares), carrier concentration (n, red triangulars), and carrier mobility (μ, blue spheres) of the Bi_2Te_3 and Bi_4Te_5 films. The abbreviations: CNP, columnar nanoparticle; CNF, columnar nanoflower; ND, nanodisc; LCP, layered compact polycrystalline; LTP, layered triangular platelet; PH, polyhedron.

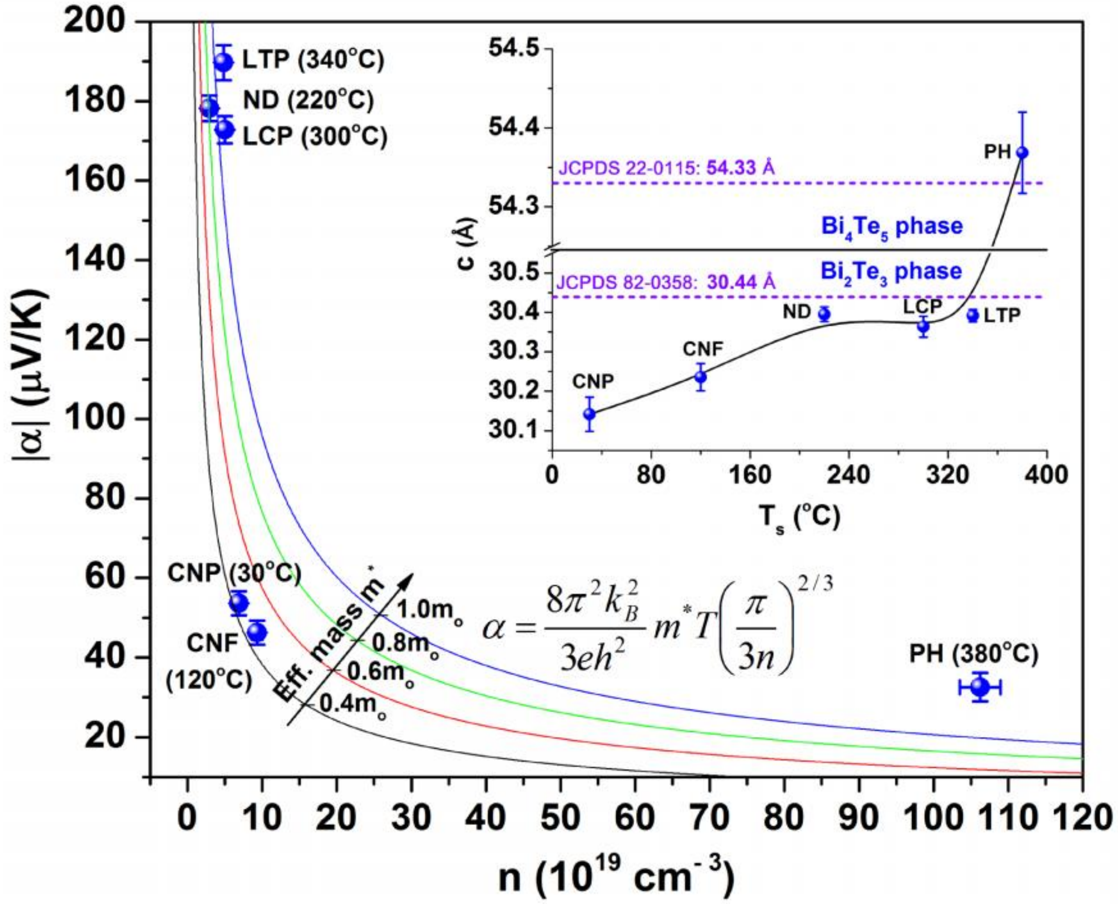

$$\alpha = \frac{8\pi^2 k_B^2}{3eh^2} m^* T \left(\frac{\pi}{3n}\right)^{2/3}$$

Figure 5.5 (a) Absolute Seebeck coefficients ($|\alpha|$) vs. *n*; the solid lines are the plots of the formula in Figure 5.5 with various effective mass m^* from $0.4m_0$ to $1.0m_0$ (m_0 is the free electron mass). Inset: T_s-dependent *c*-axis lattice constant of the Bi_2Te_3 and Bi_4Te_5 films.

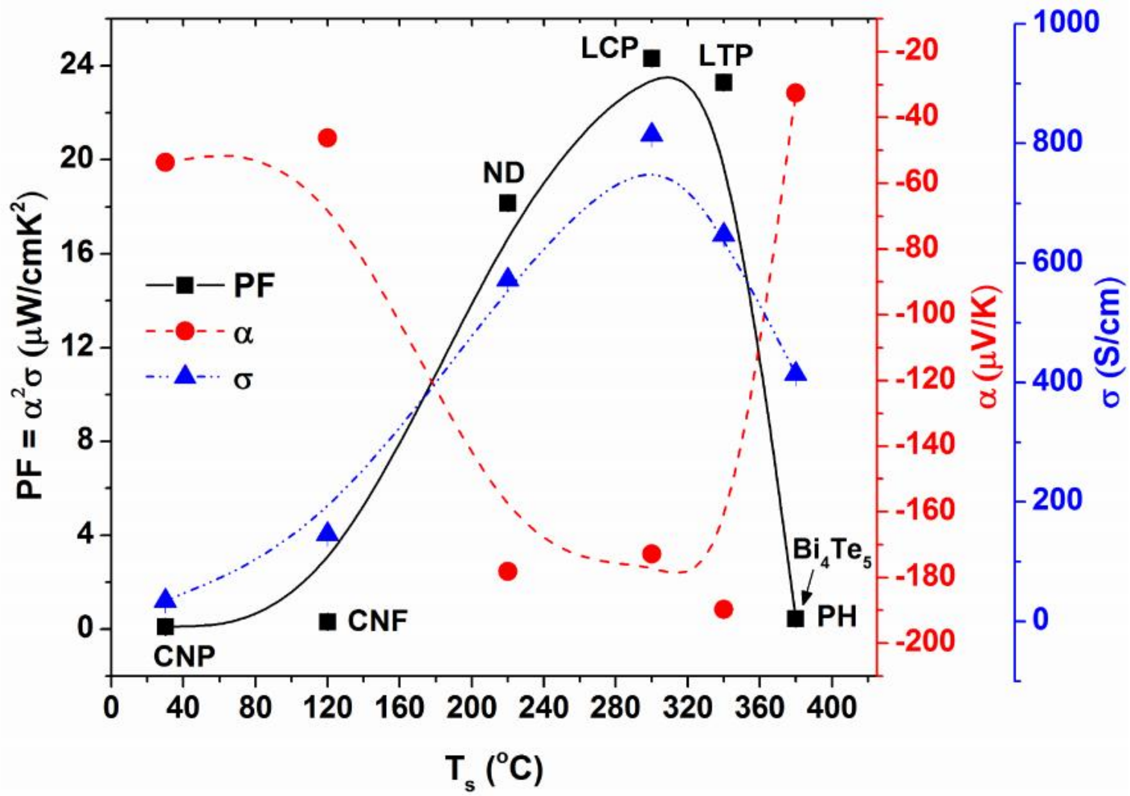

Figure 5.6 T_s dependence of room temperature Seebeck coefficient α (red circles), electrical conductivity σ (blue triangulars), and power factor (PF = $\alpha^2\sigma$, black squares) of the Bi_2Te_3 and Bi_4Te_5 films.

Table 5.1 Morphology, growth conditions, method, carrier concentration n, carrier mobility μ, electrical conductivity σ, Seebeck coefficient α, power factor PF (= $\alpha^2\sigma$), and Te content of the optimal Bi_2Te_3 thin films in this study as compared to properties of Bi_2Te_3 thin films reported in the literature. All the selected values were recorded at room temperature.

Morphology	T_s (°C)/ P_{Ar} (Pa)	**Method**	n (10^{19}cm^{-3})	μ (cm^2/Vs)	σ (S/cm)	α (μV/K)	**PF** (μW/cmK^2)	**Te** (at. %)	**Ref.**
Nanodiscs	220/ 80	PLD	2.9 ± 0.1	122.3 ± 0.5	572.0 ± 0.06	-178.2 ± 1.2	18.2 ± 0.25	60.5 ± 0.4	This work
Layered compact polycrystalline	300/ 80	PLD	5.0 ± 0.2	102 ± 3.6	814.3 ± 1.5	-172.8 ± 1.4	24.3 ± 0.44	59.7 ± 0.4	This work
Layered-triangular platelets	340/ 80	PLD	4.8 ± 0.1	83.9 ± 2.0	647.3 ± 0.4	-189.7 ± 2.3	23.3 ± 0.57	58.4 ± 0.6	This work
Layered-smooth film	250/ 10	PLD	10.1	90.6	1464.0	-186	50.6	-	Bassi et al. [17]
Compact-smooth film	350/ 10	PLD	3.5	95	532.0	-170	21.2	60	Bassi et al. [17]
Nanoparticles	300/ 20	PLD	9.7	14.8	230	-91	1.90	60	Chang et al. [39]
Layered Structure	350/ 1.0	Sputtering	95	12.1	1840	-70	8.8	56.6	Deng et al. [29]
Highly (00l)-oriented layered film	350/ 2.0	Sputtering	~10.0	52	~840.0	-200	~33.7	~60	Deng et al. [28]
Hexagonal polycrystalline	260/ -	Evaporation	1.8	125	353.4	-228	18.4	60	Silva et al. [27]
Hexagonal polycrystalline	260/ -	Evaporation	6.5	75	769.2	-228	39.9	-	Zou et al. [89]
Smooth epitaxial surface	280/ -	MBE	3.3	120	670	-201	27	60	Peranio et al. [37]

Chapter 6 Conclusions

Polycrystalline, Bi_2Se_3 thin films in chapter 4 were deposited on SiO_2/Si substrates using PLD by controlling the helium ambient pressure (P) between 0.7 and 173 Pa and the substrate temperature (T_s) between 200 and 350 °C. The Bi_2Se_3 films possessed dense, granular, and columnar structures when deposited at low (0.7 Pa), intermediate (6.7–93 Pa), and high pressures (173 Pa), respectively. The grains swelled considerably with increasing T_s because the surface mobility of adatoms increased when T_s was raised, and grain morphologies evolved from rice-liked (average size, approximately 100 nm, T_s = 200 °C) to layered structures of hexagonal platelets or flakes (average sizes, approximately 300 and 500 nm at T_s= 300 and 350 °C). The in-plane electrical conductivity (σ) decreased with increasing P because of the degradation of crystallinity and the reduction in n. However, σ increased with increasing T_s because of the enhancement in μ, crystallinity, and grain size. Specifically, Bi_2Se_3 films deposited at $P \geq 40$ Pa were stoichiometric or slightly Se rich, which diminished Se vacancies substantially to reduce the carrier concentration (n) to within $1.4 \times 10^{19} – 7.4 \times 10^{19}$ cm^{-3} even at a high T_s (up to 300 °C). More crucially, the reduction of n resulted in a substantial increase of $|\alpha|$, following the relation $|\alpha| \sim n^{-2/3}$ approximately. The films grown at T_s = 300 °C and at P = 40 Pa, and containing highly c-axis-oriented and layered hexagonal platelets, possessed the highest PF: 5.54 ± 0.34 $\mu Wcm^{-1}K^{-2}$, where $|\alpha| = 75.8 \pm 2.3$ μV/K and $\sigma = 963.8 \pm 0.4$ S/cm. The enhancement of PF in this study can be attributed to the low n (grown at $P \geq 40$ Pa) even at the high-T_s of 300 ^{o}C, which yielded a high Seebeck coefficient and excellent electrical conductivity.

In chapter 5, nanostructured n-type bismuth telluride (Bi_2Te_3) thin films were fabricated using PLD. At T_s of 220 – 340 °C and P_{Ar} = 80 Pa, the stoichiometric Bi_2Te_3 films with highly (00l)-oriented and layered structures possess remarkably high PFs between 18.2 ± 0.25 and 24.3 ± 0.44 $\mu Wcm^{-1}K^{-2}$, that is attributed to the concurrently substantial enhancements in μ (83.9 – 122.3 cm^2/Vs) and $|\alpha|$ (172.8 – 189.7 $\mu V/K$). It has been demonstrated that the morphology of highly (00l) oriented–layered structures and the stoichiometry predominantly contribute to the substantial enhancement of μ and $|\alpha|$, respectively, resulting in remarkable enhancement in PF.

This study demonstrated that tightly controlling P and T_s in PLD can enable fabrication of films that feature distinct structures and morphologies, and that it can even help overcome the challenges of growing stoichiometric films in TE Bi_2Te_3-based compounds that include volatile elements. Moreover, the interrelationships between PLD processing, morphologies, and TE properties of Bi_2Te_3-based thin films have been established comprehensively. Employing the PLD deposition strategy in this thesis, it can be expected to fabricate high PF and ZT thin films on excellent ternary compounds such as $Bi_xSb_{2-x}Te_3$, $Bi_2Te_{3-x}Se_x$…, and other complex alloys, promising for applications in TE thin-film devices.

References

[1] R. Venkatasubramanian, E. Siivola, T. Colpitts, and B. O'Quinn, *Nature* **413**, 597 (2001).

[2] D.M. Rowe, in: D.M. Rowe (Ed.), Thermoelectrics Handbook: Macro to Nano, CRC/Taylor & Francis, Boca Raton, FL, 2006.

[3] G.S. Nolas, J. Sharp, and H.J. Goldsmid, Thermoelectrics Basic Principles and New Materials Developments, Springer, Berlin, 2001.

[4] G.J. Snyder, E.S. Toberer, *Nat. Mater.* **7**, 105 (2008).

[5] C. Schumacher, K.G. Reinsberg, R. Rostek, L. Akinsinde, S. Baessler, S. Zastrow, G. Rampelberg, P. Woias, C. Detavernier, J.A.C. Broekaert, J. Bachmann, and K. Nielsch, *Adv. Energy Mater.* **3**, 95 (2013).

[6] A. Soni, Z. Yanyuan, Y. Ligen, M. Khor, K. Aik, and M. S. Dresselhaus, *Nano Lett.* **12**, 1203 (2012).

[7] G. Min and D.M. Rowe, *Solid. State. Electron.* **43**, 923 (1999).

[8] H. Böttner, J. Nurnus, A. Gavrikov, G. Kühner, M. Jägle, C. Künzel, D. Eberhard, G. Plescher, A. Schubert, and K.-H. Schlereth, *J. Microelectromechanical Syst.* **13**, 414 (2004).

[9] B. Huang, C. Lawrence, A. Gross, G.-S. Hwang, N. Ghafouri, S.-W. Lee, H. Kim, C.-P. Li, C. Uher, K. Najafi, and M. Kaviany, *J. Appl. Phys.* **104**, 113710 (2008).

[10] M. Takashiri, T. Shirakawa, K. Miyazaki, and H. Tsukamoto, *Sensors and Actuators A* **138**, 329 (2007).

[11] M. Takashiri, M. Takiishi, S. Tanaka, K. Miyazaki, and H. Tsukamoto, *J. Appl. Phys.* **101**, 074301 (2007).

[12] C.-N. Liao, Y.-C. Wang, and H.-S. Chu, *J. Appl. Phys.* 104 (2008) 104312.

[13] H.-C. Chang, C.-H. Chen, and Y.-K. Kuo, *Nanoscale* **5**, 7017 (2013).

[14] K. Kadel, L. Kumari, W.Z. Li, J.Y. Huang, and P.P. Provencio, *Nanoscale Res. Lett.* **6**, 57 (2011).

[15] Z. Sun, S. Liufu, and L. Chen, *Dalton Transact.* **39**, 10883 (2010).

[16] M. Takashiri, K. Miyazaki, S. Tanaka, J. Kurosaki, D. Nagai, and H. Tsukamoto, *J. Appl. Phys.* **104**, 084302 (2008).

[17] A. Li Bassi, A. Bailini, C.S. Casari, F. Donati, A. Mantegazza, M. Passoni, V. Russo, and C.E. Bottani, *J. Appl. Phys.* **105**, 124307 (2009).

[18] R.S. Makala, K. Jagannadham, and B.C. Sales, *J. Appl. Phys.* **94**, 3907 (2003).

[19] L.M. Goncalves, C. Couto, P. Alpuim, A.G. Rolo, F. Völklein, and J.H. Correia, *Thin Solid Films* **518**, 2816 (2010).

[20] P.H. Le, C.-N. Liao, C.W. Luo, J.-Y. Lin, and J. Leu, *Appl. Surf. Sci.* **285P**, 657 (2013).

[21] H. Noro, K. Sato, and H. Kagechika, *J. Appl. Phys.* **73**, 1252 (1993).

[22] J. Navrátil, J. Horák, T. Plecháček, S. Kamba, P. Lošt'ák, J.S. Dyck, W. Chen, and C. Uher, *J. Solid State Chem.* **177**, 1704 (2004).

[23] Y. Hor, A. Richardella, P. Roushan, Y. Xia, J. Checkelsky, A. Yazdani, M. Hasan, N. Ong, and R. Cava, *Phys. Rev. B* **79**, 195208 (2009).

[24] A. Mzerd, D. Sayah, J.C. Tedenac, and A. Boyer, *J. Cryst. Growth* **140**, 365 (1994).

[25] N. Peranio, M. Winkler, D. Bessas, Z. Aabdin, J. König, H. Böttner, R.P. Hermann, and O. Eibl, *J. Alloys Compd.* **521**, 163 (2012).

[26] H. Zou, D. M. Rowe, and S.G.K. Williams, *Thin Solid Films* **408**, 270 (2002).

[27] L.W. da Silva, M. Kaviany, and C. Uher, *J. Appl. Phys.* **97**, 114903 (2005).

[28] Z. Zhang, Y. Wang, Y. Deng, and Y. Xu, *Solid State Commun.* **151**, 1520 (2011).

[29] Y. Deng, H.-M. Liang, Y. Wang, Z.-W. Zhang, M. Tan, and J.-L. Cui, *J. Alloys Compd.* **509**, 5683 (2011).

[30] C.-N. Liao, X.-W. Su, K.-M. Liou, and H.-S. Chu, *Thin Solid Films* **519**, 4394 (2011).

[31] Y. Zhou, L. Li, Q. Tan, and J.-F. Li, *J. Alloys Compd.* **590**, 362 (2014).

[32] H.-S. Kim and S.-J. Hong, *J. Alloys Compd.* **586**, S428 (2014).

[33] W. Xie, J. He, H.J. Kang, X. Tang, S. Zhu, M. Laver, S. Wang, J.R.D. Copley, C.M. Brown, Q. Zhang, and T.M. Tritt, *Nano Lett.* **10**, 3283 (2010).

[34] P. Puneet, R. Podila, M. Karakaya, S. Zhu, J. He, T.M. Tritt, M.S. Dresselhaus, and A.M. Rao, *Sci. Rep.* **3**, 3212 (2013).

[35] A. Al Bayaz, A. Giani, M.C. Artaud, A. Foucaran, F.P. Delannoy, and A. Boyer, *J. Cryst. Growth* **241**, 463 (2002).

[36] L.D. Alegria, M.D. Schroer, A. Chatterjee, G.R. Poirier, M. Pretko, S.K. Patel, and J.R. Petta, *Nano Lett.* **12**, 4711 (2012).

[37] N. Peranio, O. Eibl, and J. Nurnus, *J. Appl. Phys.* **100**, 114306 (2006).

[38] A. Bailini, F. Donati, M. Zamboni, V. Russo, M. Passoni, C.S. Casari, A. Li Bassi, and C.E. Bottani, *Appl. Surf. Sci.* **254**, 1249 (2007).

[39] H.-C. Chang and C.-H. Chen, *CrystEngComm* **13**, 5956 (2011).

[40] X. Qiu, L.N. Austin, P.A Muscarella, J.S. Dyck, and C. Burda, *Angew. Chem. Int. Ed. Engl.* **45**, 5656 (2006).

[41] L.E. Bell, *Science* **321**, 1457 (2008).

[42] G. Chen and A. Shakouri, *Transactions of the ASME* **124**, 242 (2002).

[43] J.-F. Li, W.-S. Liu, L.-D. Zhao, and M. Zhou, *NPG Asia Mater.* **2**, 152 (2010).

[44] Y. Lan, A.J. Minnich, G. Chen, and Z. Ren, *Adv. Funct. Mater.* **20**, 357 (2010).

[45] http://www.electronics-cooling.com/2005/11/advances-in-high-performance-cooling-for-electronics/

[46] F.D. Rosi, J.P. Dismukes, and E.F. Hockings, *Electr. Eng.* **79**, 450 (1960).

[47] C. Wood, *Rep. Prog. Phys.* **51**, 459 (1988).

[48] Y. Gelbstein, Z. Dashevsky, and M.P. Dariel, *Physica B* **363**, 196 (2005).

[49] G. Tan, L.-D. Zhao, F. Shi, J.W. Doak, S.-H. Lo, H. Sun, C. Wolverton, V.P. Dravid, C. Uher, and M.G. Kanatzidis, *J. Am. Chem. Soc.* **136**, 7006 (2014).

[50] N. A. Sidorenko and L.D. Ivanova, *Inorg. mater.* **37**, 331 (2001).

[51] J.P. Heremans, V. Jovovic, E.S. Toberer, A. Saramat, K. Kurosaki, A. Charoenphakdee, S. Yamanaka, and G.J. Snyder, *Science* **321**, 554 (2008).

[52] http://www.electronics-cooling.com/2011/09/thin-film-thermoelectrics-today-and-tomorrow/

[53] J. P. Heremans, M.S. Dresselhaus, L.E. Bell, and D.T. Morelli, *Nat. Nanotechnol.* **8**, 471 (2013).

[54] http://spectrum.ieee.org/computing/hardware/intelled-team-demonstrates-first-chipscale-thermoelectric-refrigerator

[55] I. Chowdhury, R. Prasher, K. Lofgreen, G. Chrysler, S. Narasimhan, R. Mahajan, D. Koester, R. Alley, and R. Venkatasubramanian, *Nat. Nanotechnol.* **4**, 235 (2009).

[56] K. Nielsch, J. Bachmann, J. Kimling, and H. Böttner, *Adv. Energy Mater.* **1**, 713 (2011).

[57] W. Liu, X. Yan, G. Chen, and Z. Ren, Nano Energy **1**, 42 (2012).

[58] D. Kraemer, B. Poudel, H.-P. Feng, J.C. Caylor, B. Yu, X. Yan, Y. Ma, X. Wang, D. Wang, A. Muto, K. McEnaney, M. Chiesa, Z. Ren, and G. Chen, *Nat. Mater.* **10**, 532 (2011).

[59] http://www.idtechex.com/research/reports/thermoelectric-energy-harvesting-2014-2024-devices-applications-opportunities-000392.asp

[60] G.S. Nolas, D.T. Morelli, and T.M. Tritt, *Annu. Rev. Mater. Sci.* **29**, 89 (1999).

[61] H. Alam and S. Ramakrishna, *Nano Energy* **2**, 190 (2013).

[62] P. Pichanusakorn and P. Bandaru, *Mater. Sci. Eng. R* **67**, 19 (2010).

[63] M. Cutler, J.F. Leavy, and R.L. Fitzpatrick, *Phys. Rev.* **133**, 1143 (1964).

[64] T.M. Tritt, *Annu. Rev. Mater. Res.* **41**, 433 (2011).

[65] M. Martín-González, O. Caballero-Calero, and P. Díaz-Chao, *Renew. Sustain. Energy Rev.* **24**, 288 (2013).

[66] J. Eilertsen, J. Li, S. Rouvimov, and M.A. Subramanian, *J. Alloys Compd.* **509**, 6289 (2011).

[67] M.S. Dresselhaus, G. Chen, M.Y. Tang, R.G. Yang, H. Lee, D.Z. Wang, Z.F. Ren, J.-P. Fleurial, and P. Gogna, *Adv. Mater.* **19**, 1043 (2007).

[68] L.D. Hicks and M.S. Dresselhaus, *Phys. Rev. B* **47**, 12727 (1993).

[69] L.D. Hicks and M.S. Dresselhaus, *Phys. Rev. B* **47**, 16631 (1993).

[70] C. J. Vineis, A. Shakouri, A. Majumdar, and M.G. Kanatzidis, *Adv. Mater.* **22**, 3970 (2010).

[71] K.F. Hsu, S. Loo, F. Guo, W. Chen, J.S. Dyck, C. Uher, T. Hogan, E.K. Polychroniadis, and M.G. Kanatzidis, *Science* **303**, 818 (2004).

[72] D.Y. Chung, T. Hogan, P. Brazis, M. Rocci-Lane, C. Kannewurf, M. Bastea, C. Uher, and M.G. Kanatzidis, *Science* **287**, 1024 (2000).

[73] T.C. Harman, P.J. Taylor, M.P. Walsh, and B.E. LaForge, *Science* **297**, 2229 (2002).

[74] A.I. Boukai, Y. Bunimovich, J. Tahir-Kheli, J.-K. Yu, W.A. Goddard, and J.R. Heath, *Nature* **451**, 168 (2008).

[75] A.I. Hochbaum, R. Chen, R.D. Delgado, W. Liang, E.C. Garnett, M. Najarian, A. Majumdar, and P. Yang, *Nature* **451**, 163 (2008).

[76] B. Poudel, Q. Hao, Y. Ma, Y. Lan, A. Minnich, B. Yu, X. Yan, D. Wang, A. Muto, D. Vashaee, X. Chen, J. Liu, M.S. Dresselhaus, G. Chen, and Z. Ren, *Science* **320**, 634 (2008).

[77] P.F.P. Poudeu, J.D'Angelo, A.D. Downey, J.L. Short, T.P. Hogan, and M.G. Kanatzidis, *Angew. Chem. Int. Ed. Engl.* **45**, 3835 (2006).

[78] J. Androulakis, C.-H. Lin, H.-J. Kong, C. Uher, C.-I. Wu, T. Hogan, B.A. Cook, T. Caillat, K.M. Paraskevopoulos, and M.G. Kanatzidis, *J. Am. Chem. Soc.* **129**, 9780 (2007).

[79] J.-S. Rhyee, K.H. Lee, S.M. Lee, E. Cho, S.I. Kim, E. Lee, Y.S. Kwon, J.H. Shim, and G. Kotliar, *Nature* **459**, 965 (2009).

[80] A. Saramat, G. Svensson, A.E.C. Palmqvist, C. Stiewe, E. Mueller, D. Platzek, S.G.K. Williams, D.M. Rowe, J.D. Bryan, and G. D. Stucky, *J. Appl. Phys.* **99**, 023708 (2006).

[81] X.W. Wang, H. Lee, Y.C. Lan, G.H. Zhu, G. Joshi, D.Z. Wang, J. Yang, A.J. Muto, M. Y. Tang, J. Klatsky, S. Song, M.S. Dresselhaus, G. Chen, and Z.F. Ren, *Appl. Phys. Lett.* **93**, 193121 (2008).

[82] D. Vashaee and A. Shakouri, *Phys. Rev. Lett.* **92**, 106103 (2004).

[83] A. Ishida, D. Cao, S. Morioka, M. Veis, Y. Inoue, and T. Kita, *Appl. Phys. Lett.* **92**, 182105 (2008).

[84] S.A. Nemov and Y.I. Ravich, *Physics-Uspeckhi* **41**, 735 (1998).

[85] G. Wang, L. Endicott, C. Uher, *Sci. Adv. Mater.* **3**, 539 (2011).

[86] Laird Technologies: http://www.lairdtech.com/nextreme/#.U5sTU5SSyKI

[87] J. Martin, L. Wang, L. Chen, and G. Nolas, *Phys. Rev. B* **79**, 115311 (2009).

[88] J.Y.W. Seto, J. Appl. Phys. 46 (1975) 5247.

[89] H. Zou, D.M. Rowe, and G. Min, *J. Cryst. Growth* **222**, 82 (2001).

[90] H. Obara, S. Higomo, M. Ohta, A. Yamamoto, K. Ueno, and T. Iida, *Jpn. J. Appl. Phys.* **48**, 085506 (2009).

[91] D.G. Cahill, *Rev. Sci. Instrum.* **61**, 802 (1990).

[92] M. Takashiri, S. Tanaka, K. Miyazaki, and H. Tsukamoto, *J. Alloys Compd.* **490**, L44 (2010).

[93] I. Yamasaki, R. Yamanaka, M. Mikami, H. Sonobe, Y. Mori, and T. Sasaki, *17th International Conference on Therrnoelectrics* 210 (1998).

[94] R. Venkatasubramanian, *Phys. Rev. B* **61**, 3091 (2000).

[95] J. Walachová, R. Zeipl, J. Zelinka, V. Malina, M. Pavelka, M. Jelínek, V. Studnička, and P. Lošt’ák, *Appl. Phys. Lett.* **87**, 081902 (2005).

[96] C. Chen, Y. Chen, S. Lin, J.C. Ho, P. Lee, C. Chen, and S.R. Harutyunyan, *J. Phys. Chem. C* **114**, 3385 (2010).

[97] C.-N. Liao, H.-D. Shih, and P.-W. Su, *J. Electrochem. Soc.* **157**, D605 (2010).

[98] H. Lind, S. Lidin, and U. Häussermann, *Phys. Rev. B* **72**, 184101 (2005).

[99] F.-T. Huang, M.-W. Chu, H. Kung, W. Lee, R. Sankar, S.-C. Liou, K. Wu, Y. Kuo, and F. Chou, *Phys. Rev. B* **86**, 081104 (2012).

[100] J.E. Brom, Y. Ke, R. Du, D. Won, X. Weng, K. Andre, J.C. Gagnon, S.E. Mohney, Q. Li, K. Chen, X.X. Xi, and J.M. Redwing, *Appl. Phys. Lett.* **100**, 162110 (2012).

[101] L. He, F. Xiu, Y. Wang, A.V. Fedorov, G. Huang, X. Kou, M. Lang, W.P. Beyermann, J. Zou, and K.L. Wang, *J. Appl. Phys.* **109**, 103702 (2011).

[102] M. Ohring, *The Materials Science of Thin Films*, Academic Press, San Diego, CA, 1992.

[103] D.L. Smith, *Thin-Film Deposition: Principles & Practice*, McGraw-Hill, 1995.

[104] P.B. Barna and M. Adamik, *Thin Solid Films* **317**, 27 (1998).

[105] D. Kong, W. Dang, J.J. Cha, H. Li, S. Meister, H. Peng, Z. Liu, and Y. Cui, *Nano Lett.* **10**, 2245 (2010).

[106] W. Lu, Y. Ding, Y. Chen, Z.L. Wang, and J. Fang, *J. Am. Chem. Soc.* **127**, 10112 (2005).

[107] J.A. Thornton, *J. Vac. Sci. Technol.* **11**, 666 (1974).

[108] J.A. Thornton, *J. Vac. Sci. Technol.* **12**, 830 (1975).

[109] G. Koren, T. Kirzhner, E. Lahoud, K. Chashka, and A. Kanigel, *Phys. Rev. B* **84**, 224521 (2011).

[110] A. Matsunawa, JWRI **15**, 61 (1986).

[111] T. Yoshida, S. Takeyama, Y. Yamada, and K. Mutoh, *Appl. Phys. Lett.* **68**, 1772 (1996).

[112] L. Xue, P. Zhou, C.X. Zhang, C.Y. He, G.L. Hao, L.Z. Sun, J.X. Zhong, *AIP Advances* **3**, 052105 (2013).

[113] P. Tabor, C. Keenan, S. Urazdhin, and D. Lederman, *Appl. Phys. Lett.* **99**, 013111 (2011).

[114] K. Kishimoto and T. Koyanagi, *J. Appl. Phys.* **92**, 2544 (2002).

[115] A. Saji, S. Ampili, S.-H. Yang, K.J. Ku, and M. Elizabeth, *J. Phys.: Condens. Matter* **17**, 2873 (2005).

[116] Z. Wang, T. Lin, P. Wei, X. Liu, R. Dumas, K. Liu, and J. Shi, *Appl. Phys. Lett.* **97**, 042112 (2010).

[117] T. Karabacak, J.P. Singh, Y.-P. Zhao, G.-C. Wang, and T.-M. Lu, *Phys. Rev. B* **68**, 125408 (2003).

[118] Y. Liang, W. Wang, B. Zeng, G. Zhang, J. Huang, J. Li, T. Li, Y. Song, and X. Zhang, *J. Alloys Compd.* **509**, 5147 (2011).

[119] G. Hao, X. Qi, L. Yang, Y. Liu, J. Li, L. Ren, F. Sun, and J. Zhong, *AIP Adv.* **2**, 012114 (2012).

[120] Y. Deng, Y. Xiang, and Y. Song, *Cryst. Growth Des.* **9**, 3079 (2009).

[121] S.X. Zhang, L. Yan, J. Qi, M. Zhuo, Y.-Q. Wang, R.P. Prasankumar, Q.X. Jia, and S.T. Picraux, *Thin Solid Films* **520**, 6459 (2012).

[122] P.H. Le, K.H. Wu, C.W. Luo, and J. Leu, *Thin Solid Films* **534**, 659 (2013).

[123] S. Cho, Y. Kim, A. DiVenere, G.K. Wong, J.B. Ketterson, and J.R. Meyer, *Appl. Phys. Lett.* **75**, 1401 (1999).

[124] A. Hashibon and C. Elsässer, *Phys. Rev. B* **84**, 144117 (2011).

[125] G. Wang, X.G. Zhu, Y.Y. Sun, Y.Y. Li, T. Zhang, J. Wen, X. Chen, K. He, L.L. Wang, X.C. Ma, J.F. Jia, S.B. Zhang, and Q.K. Xue, *Adv. Mater.* **23**, 2929 (2011).

[126] J.W.G. Bos, H.W. Zandbergen, M.-H. Lee, N.P. Ong, and R.J. Cava, *Phys. Rev. B* **75**, 195203 (2007).

[127] H.S. Shin, S.G. Jeon, J. Yu, Y.-S. Kim, H.M. Park, J.Y. Song, Nanoscale **6**, 6158 (2014).

Curriculum vitae

LE HUU PHUOC (黎有福)

No. 359A, Quang Trung Street, Phu Thu Ward, Cai Rang District, Can Tho City, Viet Nam.
Gender: Male, Date of birth: 19 November 1983, Nationality: Viet Nam
Lecturer, Faculty of Basic Sciences, Can Tho University of Medicine and Pharmacy.
No. 179, Nguyen Van Cu Street, An Khanh Ward, Ninh Kieu District, Can Tho, Viet Nam. Cell phone: (+84) 916200095, Email: lhuuphuoc@ctump.edu.vn

---

EDUCATION

- September 2010 – August 2014
  National Chiao Tung University, Hsinchu, Taiwan
  Ph.D., Materials Science and Engineering
- September 2007 – October 2009
  Can Tho University, Can Tho, Viet Nam
  M.S., Engineering Physics
- September 2001 – August 2005
  Can Tho University, Can Tho, Viet Nam
  B.S., Physics

EXPERIENCE

- Conducting courses
  - General Physics.
  - Biophysics.
- Graduate course assistant
  - Vacuum Technology and Applications.
  - Low dielectric constant materials and processing technology.
- Operating advanced instrumentations and analyzing data

SEM, TEM, XPS-Auger spectroscopy, XRD, FT-IR, UV-VIS, Raman spectroscopy, PLD, Pump-Probe spectroscopy, Hall effect measurement, R(T).

EXPERTISE

- Thermoelectric materials and applications
- Topological insulator materials
- Superconductivity phenomena in topological insulator materials
- Growth and characterization thin-film materials using pulsed laser deposition
- Materials: Bi_2Se_3, Bi_2Te_3, SnTe, ITO, FTO, TiO_2 …

THESIS

Ph.D.: Bi_2Se_3 and Bi_2Te_3 Thermoelectric Thin-Films Grown using Pulsed Laser Deposition: Effects of Structure, Composition, and Morphology on the Thermoelectric Properties.

M.S.: Effects of Laser parameters on Laser–Tissue interaction in Percutaneous Laser Disc Decompression Technique.

PUBLICATIONS

Journal papers

[1] **Phuoc Huu Le**, Chien-Neng Liao, Chih Wei Luo, Jihperng Leu, *Thermoelectric properties of nanostructured tin-telluride thin films grown using pulsed laser deposition*, Journal of Alloys and Compounds 615 (2014) 546 – 552.

[2] **Phuoc Huu Le**, Chien-Neng Liao, Chih Wei Luo, Jiunn-Yuan Lin, Jihperng Leu, *Thermoelectric properties of bismuth-selenide films with controlled morphology and texture grown using pulsed laser deposition*, Applied Surface Science, 285P (2013) 657-663.

[3] **Phuoc Huu Le**, Kaung Hsiung Wu, Chih Wei Luo, Jihperng Leu, January **2013**, *Growth and characterization of topological insulator* Bi_2Se_3 *thin films on* $SrTiO_3$ *using pulsed laser deposition*, Thin Solid Films 534 (2013) 659 – 665.

[4] **Phuoc Huu Le**, Wen-Yen Tzeng, Hsueh-Ju Chen, Chih Wei Luo, Jiunn-Yuan Lin, Jihperng Leu, *Superconductivity in Textured Bi clusters/*Bi_2Te_3 *Films*, under review the revision manuscript by APL Materials (2014).

Conferences and Workshops

[1] **Phuoc Huu Le**. Wen-Yen Tzeng, Hsueh-Ju Chen, Chih Wei Luo, Jiunn-Yuan Lin, Jihperng Leu, "*Magnetoresistance and Superconductivity in Bi-Clusters/*Bi_2Te_3 *Films*", Materials Research Society (MRS) in San Francisco city, USA, 21-25 April, 2014.

[2] Jun Jie Huang, **Phuoc Huu Le**, Jihperng Leu, *"Thermoelectric properties of bismuth telluride films with controlled structure and morphology"*, International IUMRS-ICEM workshop in Taipei, Taiwan, 10-14 June, 2014.

[3] **Le Huu Phuoc**, Ha Viet Hien, *Effects of Laser parameters on Laser–Tissue interaction in Percutaneous Laser Disc Decompression Technique*, Journal of Medicine Practice (Viet Nam), 682 + 683 (2009) 106 – 110.